UC Irvine

UC Irvine Electronic Theses and Dissertations

Title

Modeling of Human Vascularized Colon Tumors in Three-dimensional Extracted Extracellular Matrices

Permalink

https://escholarship.org/uc/item/4pd1j810

Author

Romero Lopez, Monica

Publication Date

2016

Peer reviewed|Thesis/dissertation

eScholarship.org Powered by the California Digital Library
University of California

UNIVERSITY OF CALIFORNIA,
IRVINE

Modeling of Human Vascularized Colon Tumors in Three-dimensional Extracted Extracellular Matrices

DISSERTATION

submitted in partial satisfaction of the requirements
for the degree of

DOCTOR OF PHILOSOPHY

in Biomedical Engineering

by

Monica Romero Lopez

Dissertation Committee:
Professor Christopher C.W. Hughes, Co-Chair
Professor John S. Lowengrub, Co-Chair
Assistant Professor Michelle Digman
Associate Professor Elliot Botvinick

2016

© 2016 Monica Romero Lopez

DEDICATION

To

my parents, my sister, babies and friends

Table of Contents

LIST OF FIGURES v

LIST OF TABLES vi

ACKNOWLEDGMENTS vii

CURRICULUM VITAE ix

CHAPTER 1. Introduction 1

The complexities of cancer 2
The extracellular matrix (ECM) 2
Extracellular matrix disruptions in the tumor microenvironment 2
Stromal cells and cancer 3
Tumor Associated Signatures 4
Tumor angiogenesis and the ECM 5
Assays to study tumor evolution 6
In vitro assays 7
Extracellular matrix tissue extraction through decellularization process 8
Recreating the tumor microenvironment 9

References 11

CHAPTER 2. Recapitulating the human tumor microenvironment in vitro: colon tumor-derived extracellular matrix promotes angiogenesis and tumor cell growth. 15

Introduction 16
Materials and Methods 20
Materials, cells and animals 20
Methods 22
Results 30
Preparation of extracellular matrix gels 30
Characterization of normal ECM and tumor ECM 30
Normal ECM supports vascular network formation 31
Tumor ECM promotes the formation of tumor-like vasculature 32
Normal ECM and Tumor ECM have proteins in common, but tumor ECM has additional components 32
Microrheological measurments of normal ECM and tumor ECM 33
Colon tumor spheroids grow faster in tumor ECM 33
Both tumor cells and endothelial cells are more glycolytic in tumor ECM than in normal ECM 33
Tumor ECM promotes higher expression of genes associated with glycolysis 34
Discussion 35
Figures 40

References 48

CHAPTER 3. Multiscale Modeling of Glioblastoma Reveals that Partially Disrupting Vessel/Cancer Stem Cell Crosstalk Reduces Tumor Size without Increasing Invasiveness 53

Introduction 54
Methods 56
Continuum tumor growth model 56
Tumor cell species and lineage relationships 57

Angiogenesis 57
Cell Substrates and Feedback Regulation 58
Crosstalk 59
Results 61
VEC-GSC crosstalk promotes stem cell proliferation 61
VEGF sources affect tumor and vasculature characteristics 62
Higher initial GSC fractions increase tumor sizes and vessel numbers 65
Partially disrupting VEC-GSC crosstalk reduces tumor volume without significantly increasing invasiveness 66
Discussion 68
Conclusion 70
Acknowledgment 71
Figures 72

References 76
Supplemental Materials 79

References 91

CHAPTER 4. 3D Mathematical modeling of vascularized glioblastoma reveals that transdifferentiated vascular or vascular-supporting cells promote resistance to combinatorial therapies 93
Abstract 93
Major Findings 94
Quick Guide to Equations and Assumptions 94
Introduction 97
Results 101
Discussion 106
Methods 109
Figures 113

References 120

CHAPTER 5. Summary and Conclusions 123

References 125

LIST OF FIGURES

		Page
Figure 2.1.	ECM hydrogel extraction process	40
Figure 2.2	Characterization of the ECM from the human normal colon and the human colon liver metastasis.	41
Figure 2.3.	Vasculogenesis assay in Fibrin and Normal ECM (nECM).	42
Figure 2.4	Vasculogenesis assay in Normal ECM (nECM) and Tumor ECM (tECM).	43
Figure 2.5.	Tumor cell growth is increased in Tumor ECM (tECM).	44
Figure 2.6.	Fluorescence Lifetime Imaging Microscopy	45
Figure.3.1.	VEC-GSC crosstalk promotes GSC proliferation and self-renewal	72
Figure 3.2	VEGF sources affect tumor and vasculature characteristics.	73
Figure 3.3.	Higher initial GSC fractions increase tumor sizes and vessel numbers	74
Figure 3.4	Treatment of vascularized GBM	75
Figure 4 1.	Model schematic and spatial distribution of transdifferentiated gECs in control case	113
Figure 4.2.	Anti-angiogenic therapy reduces tumor size but increases invasion	114
Figure 4.3	Chemotherapy reduces tumor size but results in multifocal tumors.	115
Figure 4.4.	Wnt-inhibitor therapy reduces tumor invasion but suffers from resistance induced by transdifferentiation.	116
Figure.4.5.	Differentiation therapy reduces both tumor growth and invasion.	117
Figure 4.6.	Transdifferentiated gECs/gPericytes enhance tumor resistance to therapies by supporting gCSCs	118
Figure 4.7	Combined therapies effectively control both tumor growth and invasion	119

LIST OF TABLES

Page

Table 2.1. Mass spectrometry data. 46

Table 2. 2 The stiffness of nECM and tECM hydrogels. 47

ACKNOWLEDGMENTS

I deeply thank to both of my doctoral advisors, Dr. Hughes and Dr. Lowengrub. They have been very supportive during my Ph. D. I really appreciate all your time and help during my studies, in the good and the bad moments. They did not give up on me even when I thought I was not going to be able to continue. I feel very lucky to have the chance to be working with them.

I am very grateful with Dr. Chris. He believed in me although I did not have a biology background. He gave me the opportunity to work in his awesome lab and to choose my doctoral project. He gives to his students the freedom to do and follow our ideas but he is always there for advice and direction even when he is very busy. In his lab, I discovered that I really enjoy doing biology and engineering experiments.

Also, I want to thank to Dr. Lowengrub, I met him in a conference in Mexico City, I was very impressed with his research and he suggested me to apply to UCI. He helped me to get my doctoral fellowship with a project in biomedical engineering even when I was not very familiarized with the topic. I am very thankful that he let me follow my heart in my research during all my Ph. D. Dr. Huaming Yan has been very kind too, without him the modeling part would have been very difficult.

I would also like to thank to Sasha, Dr. Michelle Digman and Dr. Gratton, for their advice and time. They and their laboratories have been very supportive since the beginning of my studies. I also want to thank to Andrew Trinh and Jenu, who have been very helpful during the past couple of years. Thanks to them, I know some microscopy concepts and I have been able to use wonderful microscopes for my project. Also, Dr. Botvinick has been very encouraging; he is always very optimistic about research that reminds you how fun the science is.

Also, I am in debt with all the present and past members from the Hughes lab. They are amazing people to be with. Specially, I want to thank to Ashley Fong, who had the patience to work with me during my laboratory rotation. She has been very helpful, I have found in her a friend to whom I can talk about research but also about life. Also, I want to thank to Andrew, Katrina and Mary; I learned so many things from them, they were like superheroes for me during my first years in UCI. And, I want to express my gratitude to the current members of the lab, Jill, Agua, Michaela, Nan, Duc, Hugh and Kim. They are not only labmates for me but friends. I acknowledge Cristhian, David, Ashleigh and Lesly for all their hard work and help in my project.

I want to thank to my country, Mexico and its support through the UC-MEXUS CONACYT fellowship. I could not have done this without this fellowship and the help of my undergraduate advisors Dr. Cathy and Dr. Ramon. I am very grateful for this opportunity. I know not a lot of Mexicans have the opportunity to study a Ph. D. outside of the country. And I hope at some point I can give this back to my people.

También, quiero agradecer profundamente a mis amigos, amigas y manitas de México, Itzel, Marce, Marisol, Mariana, Gabb, Judith, Vic y Germán. Que durante todo el tiempo que he estado fuera, ellos me han apoyado, y han tenido fé en mí. Todavía recuerdo cuando tome mi primer avión hacia UCI que todos estuvieron conmigo en el aeropuerto para despedirme. También me

siento muy afortunada de haber conocido gente tan bonita durante mi estancia en UCI. A los Mexicans y no Mexicans, particularmente a Martha Álvarez que me ayudó mucho durante mis primeros años en el doctorado y que siempre ha creido en mí. A Cristóbal que me ha visto y he estado conmigo en los máximos y mínimos de esta aventura y al Sensei por sus enseñanzas.

Finalmente y lo más importante, a mi familia, mi mama, mi papa y Ceci, también Pelusita y Benita, mi segunda familia, la familia Vázquez Huerta, y a Dios y a la Lupita, que han sido pilares durante estos años fuera de casa. Gracias a ellos me he levantado en tiempos de tristeza y depresión y celebrado conmigo los momentos de éxito. En especial mi mamita, que ha estado conmigo en cada una de mis historias, desveladas y aventuras buenas y no tan buenas.

Sources of funding included:
• UC-MEXUS-CONACYT Doctoral Fellowship awarded to Monica Romero Lopez
• Miguel Vélez Fellowship awarded to Monica Romero Lopez
• ¨Beca complemento SEP¨ Fellowship awarded to Monica Romero Lopez
• US National Institutes of Health UH3 TR00048 Grant awarded to Dr. Christopher C.W. Hughes

CURRICULUM VITAE

Monica Romero Lopez

- **Ph. D. Candidate in Biomedical Engineering** 2010-2016
  Thesis: A three-dimensional study of cancer spheroid growth
  and angiogenesis in a human-extracted colon and cancer extracellular matrix.
  Advisors: John Lowengrub, Ph. D., and Christopher
  Hughes, Ph. D. University of California, Irvine, USA.
  GPA: 3.81/4
- **Advanced to candidacy** April 3, 2014
- **M.S. in Biomedical Engineering** March, 2014
- **1-year program in Mathematical and Computational Biology** 2010-2011
  University of California, Irvine, USA.
  GPA: 3.8/4
- **B. Sc. Mathematics** Fall 2004-Fall 2009
  National Autonomous University of Mexico (UNAM). Mexico City, Mexico.
  GPA: 9.33/10
  Honor's thesis Summer 2009-Summer 2011
  A Model for Tumor Antiangiogenesis in Secondary Tumors.
  Advisors: Catherine Garcia Reimbert, Ph. D. and Ramón Gabriel Plaza
  Villegas, Ph. D.
  Institute of Applied Mathematics and Systems (IIMAS),
  UNAM. Mexico City, Mexico.

Fellowships and Awards:

- **Miguel Velez fellowship** April 2016-June 2016
- **"Beca complemento de la SEP" (** September 2014-June 2015
  Miguel Velez fellowship April 2012-June 2012
- **UC MEXUS-CONACYT doctoral fellowship** September 2010-June 2015
- **Research assistant fellowship CONACYT project U47899-F** October 2009-February 2010
- **"Proyecto UNAM", research assistant fellowship** January 2008-January 2009

Publications:

- Welch-Reardon KM, Ehsan SM, Wang K, Wu N, Newman AC**, Romero-Lopez M**, Fong AH, George SC, Edwards RA, Hughes CC. Angiogenic sprouting is regulated by endothelial cell expression of Slug**,** J Cell Sci. 2014 May 1;127 (Pt 9): 2017-28.

- Ashley H. Fong, BS, **Mónica Romero-López**', MS, Chris Heylman, PhD, Mark T. Keating, BS, David Tran, PhD, Agua Sobrino, PhD, Anh Q. Tran, BS, Hiep H. Pham, BS, Cristhian Fimbres, BS, Paul D. Gershon, PhD, Elliot L. Botnovik, PhD, Steven C.

George, MD, PhD, Christopher C. W. Hughes, PhD, Three-dimensional adult cardiac extracellular matrix promotes maturation of human induced pluripotent stem cell-derived cardiomyocytes, Accepted

- Agua Sobrino, Duc T. Phan, Xiaolin Wang, Rupsa Datta, Stephanie J. Hachey, **Mónica Romero-López,** Enrico Gratton, Abe P Lee, Steven C. George and Christopher C.W. Hughes. A vascularized and perfused human micro-tumor platform for cancer drug screening. Accepted

- Yan Huaming**, Romero-López M,** Hughes CC, Lowengrub J**.** Three-dimensional visualization of tumor growth, angiogenesis and tumor cell transdifferentiation. Submitted

- Yan Huaming, **Romero-López M,** Hughes CC, Lowengrub J. Effect of transdifferentiated endothelial cells in glioblastoma tumor growth. (In preparation).

- **Romero-López M**., Trinh A, Lowengrub J., Hughes CC. Recapitulating the human tumor microenvironment in vitro: colon tumor-derived extracellular matrix promotes angiogenesis and tumor cell growth, (In preparation).

Presentations:

- Vascular Network Formation in Human Tumor-Derived Extracellular Matrix Compared to Normal Colon ECM in a 3D Model
  Poster Presentation, April 2016
  Biologic Scaffolds for Regenerative Medicine, Silverado, CA, USA
- Vascular Networks in 3D Scaffolds,
  Oral Presentation, April, 2016,
- *First International Forum of Mexican Talent,* Government of Mexico, Guadalajara, Mexico
- Comparison of Vascular Networks in 3D Scaffolds,
  Oral Presentation, April, 2016,
  Institute of Materials, UNAM, Mexico, Mexico
- Vascular Tissue Constructs,
  Guest Lecture, November, 2015,
  Tissue Engineering 2015, UC Irvine, U.S.A
- Vascular Network Formation in Human Tumor-Derived Extracellular Matrix Compared to Normal Colon ECM in a 3D *in vitro* Model: Tumor Matrix Promotes a More Tumor-Like Vascular Phenotype,
  Oral Presentation, October 2015,
  North America Vascular Biology Organization Meeting, Boston, MA, U.S.A.
- A Three-Dimensional Model of Vascularized Human Colon Spheroids in a Human Colon Extracted Extracellular Matrix (Reviewer Choice Award),
  Poster, October 2014,
  Biomedical Engineering Society Meeting, San Antonio, Texas, U.S.A.

- Three-Dimensional Cancer Tumor Spheroids in a Human Colon Gel, *Poster*, October, 2013
  North America Vascular Biology Organization Meeting, Boston, MA, U.S.A.

Experience:

- **Research assistant** January, 2008-January 2009
  Multivariate analysis with SPSS and MATLAB software.
  Advisors: Elizabeth Solleiro, Ph. D. and Sergey Sedov, Ph. D., UNAM.
- **Teaching experience**
  - "Tissue Engineering", teacher assistant Fall ,2015
    Biomedical Engineering department, UCI
  - "Calculus 2B", teacher assistant Spring, 2014
    Physical Sciences, UCI
  - ¨Stochastic Partial Differential Equations", grader Spring, 2013
    Physical Sciences, UCI
  - ¨Stochastic Partial Differential Equations", grader Spring, 2012
    Physical Sciences, UCI
  - "Partial Differential Equations", teacher assistant Spring, 2010
    School of Sciences, UNAM.
  - "Analytical Geometry", teacher assistant and Fall, 2009
    "Mathematics for Life Sciences", lecturer
    School of Sciences,UNAM**.**
  - "Ordinary Differential Equations", teacher assistant Spring, 2009
    School of Sciences,

Professional Service:

- Mentor UCI math CEO at Madison elementary school for biology and engineering Winter, 2016
- Graduate InterConnect Peer Mentor, project for mentoring new international graduate students at UCI
  Summer, 2015
- American Association of University Women (AAUW) Tech Trek lab host and mentor Summer, 2015
  Mentor UCI math CEO at Lathrop for middle scholars, focused in teaching science and mathematics, particularly to Mexican-American students.
  Fall 2014-Present
- Coordinator of instructors based in Mexico in the project Club de Ciencias Mexico (Science Clubs Mexico) (http://quieroaprender.masporfavor.com/equipo/?lang=en)
  Summer 2014-Present
- Teacher, organizer and coordinator of my own Science Club (Divertzciencia) focused in Tissue Engineering in Mexico to students of different high schools and colleges. (https://www.youtube.com/watch?v=JRE_YGMS1jE)

Summer 2014

- Mentor of six undergraduate students
  Summer 2011-Present

Memberships:

- North American Vascular Biology Organization member
- American Association of University Women

Relevant Skills andQualifications:

(Reading, Writing,Speaking)

- French (fluent, basic,
  basic)
- English (fluent, fluent, fluent)
- Spanish (fluent, fluent, fluent)
- Software applications: Maple 8 (Advanced), Matlab 8 (Advanced), Java (Intermediate), Latex (Advanced), R, SPSS and Minitab (Intermediate), Mathematica (Intermediate)

Courses and Conferences Attended:

- LFD (Laboratory of Fluorescence Dynamics) Workshop
  October, 2010
  University of California, Irvine
- Mathematical Modelling of Cancer Growth and Treatment Summer School
  August, 2010
  University of Dundee.
- International Conference on Mathematical Biology and
  Annual Meeting of The Society of Mathematical Biology.
  And mentoring program with Dr. Mark Chaplain.
  July 2009
  University of British Columbia, Vancouver, Canada
- Extracurricular seminar of Mathematical Biology
  Spring, 2008
  School of Sciences, UNAM.
- V Meeting of Mathematical Biology and X Autumn School (conferences series) of Biomathematics. Institute of Limnology, Autonomous University of Sinaloa, Mexico.
  November 2007
- III Meeting of Mathematical Biology and VIII Autumn School of Biomathematics.
  November, 2006
  Jalapa Ecology Institute, Veracruz,
  Mexico.

- II Meeting of Mathematical Biology
  November, 2005
  Autonomous University of Coahuila.

ABSTRACT OF THE DISSERTATION

Modeling of Human Vascularized Colon Tumors in Three-dimensional Extracted Extracellular Matrices

By

Monica Romero Lopez

Doctor of Philosophy in Biomedical Engineering

University of California, Irvine, 2016

Professor Christopher C.W. Hughes, Co-Chair and

John Lowengrub, Co-Chair

Cancer is one of the deadliest diseases; vast resources have been used to understand its root causes and to elucidate the intricacies of cancer progression in order to develop effective prevention and treatment strategies. Unfortunately, there are a lot of factors in the tumor microenvironment that contribute to cancer development and progression. Consequently, a better understanding of the tumor niche has become an important goal of cancer research. Here we have approached the problem using a combination of *in vitro* assays and computational modeling. Firstly we studied extracellular matrix (ECM). Recently, it has been found that the ECM surrounding tumors has significant effects on tumor cell growth and migration. However, there is a shortage of information on how cells respond to normal vs tumor ECM. In order to overcome this problem we have isolated human tumor ECM (tECM) and compared its chemical and mechanical properties to ECM derived from matched normal tissue (nECM). We next examined the ability of each of these matrices to support development of new vasculature – a key event in tumor progression. We found that the capillaries that form in the tECM have characteristics similar to those seen in *in vivo* tumors. We also found that tumor growth and

tumor metabolism is different in these two ECMs, with tumor growth being faster, and tumor cell metabolism more glycolytic, in the tECM. Taken together, these data identify the importance of the ECM in tumor progression and suggest that normalization of ECM morphology and composition could provide a novel strategy to limit tumor growth.

Our second approach used mathematical models to study the interaction of different tumor cell lineages with the vascular niche. We find evidence to support the idea of endothelial cell transdifferentiation into tumor cells. And, the computational simulations of the model indicated that the transdifferentiated glioblastoma cells to have a major contribution in tumor therapy resistance.

CHAPTER 1. Introduction

In the past two decades, cancer has become one of the leading causes of death in the developed world, and vast resources have been invested in an effort to understand the root causes, to elucidate the intricacies of cancer progression, and to develop effective prevention and treatment strategies.

Despite many years of study, cures are still needed, and this is due to two main reasons: (1) cancer biology is more complex than originally thought, and (2) the assays currently used to study cancer are often not ideal and do not accurately recapitulate *in vivo*, human tumors.

Of note, it has become increasingly evident that cancer is not caused by an isolated event - it must be studied as a complex progression of many disruptions to homeostasis [1]. Further, any deregulation or disorganization of the tissue homeostasis can directly affect cellular behavior, causing mutations that can lead to cancer. And, once formed, malignant tumors are not isolated entities in the organism, but are closely related to the surrounding microenvironment - including the stromal cells and the extracellular matrix (ECM).

Importantly, many of the assays currently used to study cancer biology do not accurately mimic the human tumor. Many are performed in 2D culture and very few incorporate the multiple important aspects of the tumor microenvironment, including the extracellular matrix (ECM) and vascular networks. I aimed to address some of these shortcomings by extracting human ECM and incorporating it into a 3D matrix that contains vascular structures.

The complexities of cancer

As mentioned before, the development of tumors involves multiple genetic and cellular disruptions. There are several elements of the tumor microenvironment such as the ECM and the stromal cells that participate actively in the evolution of cancer. Therefore, it is important to study the changes and interactions between the tumor and its surroundings, in particular, the ECM and the stromal cells, to better understand the complexity of this disease, and maybe, to be able to explore new ways to make anti-cancer therapy more efficient.

The extracellular matrix (ECM)

The extracellular matrix (ECM) is an interlaced, complex system of fibrous proteins mixed with proteoglycans. These components form a cross-linked network that serves as a structural scaffold for resident cells. Also, the ECM provides important biophysical and biochemical signals to the cells, and each organ has its unique ECM structure and composition specific to its function. The most important characteristics of the ECM of each tissue are the protein composition, pore size, mechanical strength and permeability to gasses, fluids, and nutrients. This specific ECM signature dictates the phenotype and behavior of the cells embedded in it [2-4]. For example, stem cells that have been seeded in scaffolds of varying stiffness were able to differentiate into cells found in ECMs with similar mechanical properties, without the use of growth factors [5]

Extracellular matrix disruptions in the tumor microenvironment

Disruptions to the ECM can have profound effects on cancer progression [6, 7]. These disruptions include physical (porosity, fiber orientation), biochemical (binding to

growth factors), and biomechanical (stiffness) alterations [8]. These ECM anomalies promote cellular transformation that may lead to the generation of a tumorigenic microenvironment. Therefore, the study of the composition and mechanical properties of the ECM before and during cancer development will help to understand better how to target the tumor niche.

Changes in ECM can also affect tumor proliferation, survival, invasion, differentiation, signaling, metastasis, drug delivery and absorption [9]. However, it is still not known if these ECM changes lead to cancer or if cancer leads to the ECM modifications *in vivo*. For this reason, it is important to explore the different ECM-tumor interactions through different assays.

Stromal cells and cancer

The development of tumors has been linked to tissue inflammation and a tumor has been described as a wound that does not heal [10]. Inflammation can induce the differentiation of fibroblasts to myofibroblasts [11], which then produce large amounts of ECM, leading to tissue remodeling. These changes in ECM organization are known as the desmoplastic reaction [12]. Additional work has to be done to investigate if this desmoplastic tissue precedes tumorigenesis or if it is a result of the interaction of cancer cells with stromal cells and ECM molecules. Tumor and stromal cells utilize overexpression or accumulation of different types of molecules, such as collagens (I, III, IV, V, XII), proteoglycans and hyaluronan around the tumor, and these molecules may help to recreate a better environment for cancer propagation [13-16].

Additionally, in the presence of tumors, stromal cells (such as fibroblasts) undergo differentiation into cancer-associated fibroblasts (CAFs). CAFs secrete chemokines, growth factors and extracellular matrix components that directly contribute to tumor progression. These cells remodel the ECM, often making it denser by secreting excess collagen I and III, thereby altering integrin signaling in the tumor cells, which can lead to an increase in tumor migration and a higher risk of tumor metastasis [17].

Tumor Associated Signatures

Mina Bissell and her research group have extensively studied breast tumor progression and tumor cross-talk with the local microenvironment [7, 10, 18-20]. Her research in this field has been very important in understanding how breast tumor cells affect the ECM and how the ECM affects the tumor cells. In the microscopy-imaging field, it is well known that collagen fibers can be visualized using a property inherent in its structure (non-centrosymmetric structure) known as second harmonic generation (SHG). Through the use of the SHG of the collagen, Bissell, and her collaborators have been able to characterize different stages of cancer prognosis and metastasis, in relation to the tumor surrounding collagen fibers [9]. These stages are known as tumor-associated collagen signatures (TACs). For example, in the normal scenario or stage 1, the collagen fibers are characterized to be random and isotropic. However, in the malignant (fibrotic or desmoplastic) tissue or stage 3, the collagen fibers are aligned and organized anisotropically. Additionally, the collagen fibers are in perpendicular direction to the border or the tumor. In this stage, it is very likely that there are some tumor cells already detached from the main tumor, metastasizing to other tissues. Therefore, in this case, there is a very

bad prognosis for the disease. Finally, during stage 2, the collagen fibers are straight, but they are aligned parallel to the tumor border.

Tumor angiogenesis and the ECM

The transition from the relatively harmless and confined dormant avascular state to the vascular state depends upon the ability of the tumor to induce the formation and invasion of blood vessels from the surrounding tissue [21], a process termed tumor angiogenesis. Without angiogenesis, a tumor cannot grow beyond approximately 2 mm in size [22, 23]. This obstacle to tumor growth requires the development of angiogenic potential within the growing tumor cells – referred to as the "angiogenic switch". This switch is an alteration in the balance between the proangiogenic and antiangiogenic factors [24]. Some of these are derived from fragments of the ECM, such as endostatin, hexastatin and canstatin (antiangiogenic factors) [25].

The angiogenic switch starts when tumor cells become hypoxic, and these cells, together with stromal cells (fibroblasts), secrete diffusible chemical signals, collectively called angiogenic factors. Some of the most important angiogenic factors are vascular endothelial cell growth factor (VEGF), transforming growth factor-β (TGF-β), fibroblast growth factors (FGF), tumor necrosis factor alpha (TNF-α) and angiopoietins (Ang-1, Ang-2) [26]. These molecules diffuse into the host microenvironment and bind to specific cell membrane receptors on the endothelial cells that line existing blood vessels. This process activates the expression of matrix metalloproteinases (MMPs) - proteolytic enzymes that facilitate degradation of the ECM and basement membrane by EC. Also, these MMPs help to remodel the ECM enabling migration of the endothelial cells towards the tumor.

Migration is mediated by the chemotactic response to tumor angiogenic factors, and the ability of MMPs (2,9,13,14) to generate space for the endothelial cells to move through and invade deeper into the ECM [27]. Therefore, matrix morphology, stiffness, and fiber orientation have strong effects on endothelial cell migration, sprout extension rate, and tumor cell invasion. Any changes in these factors can, therefore, produce an anti- or pro-angiogenic effect. It has been shown that an increase in ECM stiffness slows endothelial cell migration, therefore reducing vessel formation [28].

ECM molecules also affect the migration of tumor cells to other tissues. Evidence suggests that changes in ECM stiffness and fiber conformation can enhance cell migration and, as a result, promote the spread of cancer cell metastasis [29-31].

Understanding how disruption in the ECM can lead to altered cellular behavior is important for advancements in cancer research, and the creation of gels and scaffolds has been an effective method to reproduce the cellular microenvironment.

Assays to study tumor evolution

There are two general categories of models to study cancer progression: *in vivo* and *in vitro*. *In vivo* tumor models are more predictive because they best recapitulate the complex 3D environment. However, it is difficult to control the environment, and to visualize and quantify the results. In addition, these experiments are expensive and time-consuming. *In vitro models* –are easier to manipulate and to follow their progression over time with several visualization techniques, but they lack the complexity that it is found *in vivo*. Therefore, once these shortcomings have been overcome, *in vitro* models offer the promise of gaining insight into some of the key biological features of the several stages in cancer progression.

In vitro assays

Traditional *in vitro* experimental tumor models have focused on monolayers (2D), and many of the first studies of the interactions between tumor cells and the ECM were done in two-dimensions. For example, placing tumor cells on top of single-protein coatings (collagen or fibronectin). In these cases, the cells and the ECM protein are in direct contact, but the real spatial cell arrangement is not reproduced. Three-dimensional effects are critical to reproducing the *in vivo* cell proliferation rates, oxygen perfusion and expression of growth factors.

The emergent field of tissue engineering has focused on the design of biomimetic 3D constructs that closely resemble the *in vivo* biological, mechanical and biochemical environment. This work has focused mainly on regenerative medicine where the goal is replacing a damaged tissue or organ. There are two major approaches in the design of 3D scaffolds: one is the use of artificial scaffolds such as polymers and peptide-based hydrogels and the other is the use of hydrogels derived from native ECM components, such as fibronectin and collagen. While the hydrogels made from artificial materials can recreate the mechanical properties of the native ECM, they lack its biological and chemical composition. However, the scaffolds extracted from ECM components have the chemical and biological complexity that the artificial hydrogels lack, but sometimes they do not reproduce the *in vivo* stiffness due to the extraction methods used to obtain them. One of the most effective methods used to extract the ECM from tissues is known as decellularization, and will be discussed in the next section.

Extracellular matrix tissue extraction through decellularization process

Decellularization is the process of removing cells from tissue using physical or chemical techniques. These techniques are selected such that they minimally affect the extracellular matrix composition but sufficiently remove a majority of the cellular debris. Some of the physical techniques are freeze-thaw, sonication and mechanical removal of the tissue or some layers of it. These techniques are often used during the first steps of the decellularization process. The chemical techniques consist of washing the tissue with solutions, such as detergents, using perfusion pumps or diffusion techniques (soaking and stirring the tissue in the solution). Detergents can be Triton x100, sodium dodecyl sulfate (SDS), sodium deoxycholate (SDC), 3-[(3-cholamidopropyl) dimethylammonio]-1-propanesulfonate (CHAPS) [32], acids and bases (Peracetic acid), hypertonic or hypotonic solutions, enzymes such as trypsin, DNAase, RNAase, and others which facilitate the dissolution of membranes and remaining cellular components [33, 34]

To decellularize a tissue it is necessary to take into account the origin, thickness, age [35, 36] and stiffness of the tissue, to avoid any removal or damage of the extracellular proteins [37]. It has been shown that some solutions, such as SDS, are good for decellularizing thick tissues, but they do not preserve collagen and glycosaminoglycans (GAGs) particularly well [38]. One of the first researchers to utilize this process was Dr. Stephen Badylak, who decellularized porcine bladder and small intestine submucosa to use them as a vascular graft in the small bowel of dogs [39]. Other well-known decellularized tissues in the medical field are porcine heart valves, which are broadly used in heart valve repair [40, 41].

Most of the time, decellularization is performed in whole tissues or organs using perfusion pumps. For example, cornea [42], larynx [43], lung [44, 45], liver [46, 47], and heart [48] perfusion pumps have been used. These perfusion pumps are also used to recellularize the organ with different types of cells and to study the survival and growth of the cells in the decellularized tissue. These tissues have been shown to be rich in several types of collagen [49], elastin [40], fibronectin [50], glucosaminoglycans (GAGs) [51, 52] and growth factors [53, 54].

Badylak and colleagues developed a derived ECM hydrogel from the decellularized small intestine submucosa by lyophilizing, powdering and digesting it, resulting in a gel that can be used as an injectable graft. These ECM hydrogels have been chemically and physically characterized. It has been observed that they have the chemical complexity of the native extracellular matrixand their physical properties can be adjusted to recreate as much as possible the native tissue (such as rheological properties and fiber density). They can form through polymerization into three-dimension scaffolds similar to collagen and fibrin gels [55, 56]. In early studies, they found that these gels could be used as an *in vitro* scaffold; their urinary bladder extracted gel supported adhesion and growth of rat aortic smooth muscle cells *in vitro* [56]. Some years later, a porcine liver-derived gel was extracted and used successfully for culturing human hepatocytes *in vitro [57]*. Moreover, a heart extracted scaffold was used to induce differentiation of pluripotent stem cells without the use of growth factors [58] and human embryonic stem cells [59].

Recreating the tumor microenvironment

The field of tissue engineering and regeneration is poised to play an important role in cancer modeling. To improve repeatability and controllability advances in 3D scaffold

structures are starting to be used in cancer research. Such structures have to mimic key features of the ECM while enabling the control of their physical and biochemical properties such as a tumor-ECM composition and structure with tunable pore size, stiffness, and embedded growth factors.

In order to have an ideal 3D tumor scaffold, several variables have to be considered. For example, having stromal cells and a close vasculature, mimicking the matrix mechanical and chemical properties such as the geometry, fiber size, fiber arrangement, nutrient and oxygen diffusion rates, adhesion sites and growth factor binding.

However, most of the hydrogels that are used to study tumor progression are scaffolds derived from one ECM component or synthetic hydrogels. Some recent studies have demonstrated that tumor cells grown in those 3D matrices exhibit characteristics very similar to tumors grown *in vivo* (e.g., gene expression profiles, hypoxia and necrosis, and response to therapeutic intervention). However, these platforms lack the complex composition that is typical of native ECM and the tumor microenvironment. For example, some of these studies do not consider the stromal cells and the tumor vasculature, giving interesting results, but results that are difficult to translate into *in vivo* research.

Therefore, finding the appropriate 3D ECM gel that can recapitulate and recreate the native ECM composition in the tumor will provide valuable new tools to answer questions about microenvironmental signals in cancer progression. To this end, we describe in this work the extraction of ECM from a human tumor tissue. Additionally, we use this scaffold to study ECM-cell and cell-cell interactions in a more complex environment than have been possible up to now. We hope this work can bring new insights into the cancer research field. In the future we may be able to use our system to improve preclinical drug screening, providing more information about efficacy early in the drug

development process.

REFERENCES

1. DelNero, P., Y.H. Song, and C. Fischbach, *Microengineered tumor models: insights & opportunities from a physical sciences-oncology perspective.* Biomedical microdevices, 2013. **15**(4): p. 583-593.
2. Robert E. Hurst, K.D.K., Rebeca B. Bonner, Ron D. Bowditch and George P. Hemstreet III, *Matrix dependent plasticity of the malignant phenotype of blader cancer cells.* Anticancer Res., 2003. **23**(4): p. 3119-3128.
3. Dozmorov, M.G., et al., *Analysis of the interaction of extracellular matrix and phenotype of bladder cancer cells.* BMC Cancer, 2006. **6**: p. 12.
4. Petersen, O.W., et al., *Interaction with basement membrane serves to rapidly distinguish growth and differentiation pattern of normal and malignant human breast epithelial cells.* Proceedings of the National Academy of Sciences of the United States of America, 1992. **89**(19): p. 9064-9068.
5. Engler, A.J., et al., *Matrix Elasticity Directs Stem Cell Lineage Specification.* Cell, 2006. **126**(4): p. 677-689.
6. Ahlfors, J.-E.W. and K.L. Billiar, *Biomechanical and biochemical characteristics of a human fibroblast-produced and remodeled matrix.* Biomaterials, 2007. **28**(13): p. 2183-2191.
7. Celeste, M.N. and J.B. Mina, *Modeling dynamic reciprocity: Engineering three-dimensional culture models of breast architecture, function, and neoplastic transformation.* Seminars in Cancer Biology, 2005. **15**(5): p. 342-352.
8. Sainio, A., *Extracellular Matrix Macromolecules in Tumour Microenvironment with Special Reference to Desmoplastic Reaction and the Role of Matrix Proteoglycans and Hyaluronan.* Journal of Carcinogenesis & Mutagenesis, 2013. **S13**.
9. Lu, P., V.M. Weaver, and Z. Werb, *The extracellular matrix: A dynamic niche in cancer progression.* The Journal of Cell Biology, 2012. **196**(4): p. 395-406.
10. Bissell, M.J. and W.C. Hines, *Why don't we get more cancer? A proposed role of the microenvironment in restraining cancer progression.* Nat Med, 2011. **17**(3): p. 320-329.
11. De Wever, O., et al., *Stromal myofibroblasts are drivers of invasive cancer growth.* International Journal of Cancer, 2008. **123**(10): p. 2229-2238.
12. Annele, S., *Extracellular Matrix Macromolecules in Tumour Microenvironment with Special Reference to Desmoplastic Reaction and the Role of Matrix Proteoglycans and Hyaluronan.* Journal of Carcinogenesis & Mutagenesis, 2013. **S13**.
13. Armstrong, T., et al., *Type I collagen promotes the malignant phenotype of pancreatic ductal adenocarcinoma.* Clinical cancer research : an official journal of the American Association for Cancer Research, 2004. **10**(21): p. 7427-7437.
14. Coulson-Thomas, V., et al., *Colorectal cancer desmoplastic reaction up-regulates collagen synthesis and restricts cancer cell invasion.* Cell and tissue research, 2011. **346**(2): p. 223-236.

15. Goetz, J., et al., *Biomechanical remodeling of the microenvironment by stromal caveolin-1 favors tumor invasion and metastasis.* Cell, 2011. **146**(1): p. 148-163.
16. Nystr¸àö¸àÇm, H., et al., *Liver-metastatic potential of colorectal cancer is related to the stromal composition of the tumour.* Anticancer research, 2012. **32**(12): p. 5183-5191.
17. Tung, J.C., et al., *Tumor mechanics and metabolic dysfunction.* Free Radic Biol Med, 2015. **79**: p. 269-80.
18. Bissell, M.J. and D. Radisky, *Putting tumors in context.* Nature reviews. Cancer, 2001. **1**(1): p. 46-54.
19. Brownfield, Douglas G., et al., *Patterned Collagen Fibers Orient Branching Mammary Epithelium through Distinct Signaling Modules.* Current Biology, 2013. **23**(8): p. 703-709.
20. Kenny, P.A., et al., *The morphologies of breast cancer cell lines in three-dimensional assays correlate with their profiles of gene expression.* Mol Oncol, 2007. **1**(1): p. 84-96.
21. Macklin, P., et al., *Multiscale modelling and nonlinear simulation of vascular tumour growth.* Journal of mathematical biology, 2009. **58**(4-5): p. 765-798.
22. Folkman, J., *Tumor Angiogenesis: A Possible Control Point in Tumor Growth.* Annals of Internal Medicine, 1975. **82**(1): p. 96-100.
23. Naumov, G.N., L.A. Akslen, and J. Folkman, *Role of Angiogenesis in Human Tumor Dormancy: Animal Models of the Angiogenic Switch.* Cell Cycle, 2006. **5**(16): p. 1779-1787.
24. Figg, W.D.F., M. J. , *Angiogenesis: an integrative approach from science to medicine.* . 2008. **Springer**.
25. Ortega N, W.Z., *New functional roles for non-collagenous domains of basement membrane collagens.* J Cell Sci, 2002. **115**: p. 4201-4214.
26. Machein, M., et al., *Angiopoietin-1 promotes tumor angiogenesis in a rat glioma model.* The American journal of …, 2004.
27. Bruce Alberts, e.a., *Molecular Biology of Cell*. 5 ed. ed. 2008.
28. Bauer, A., T. Jackson, and Y. Jiang, *Topography of extracellular matrix mediates vascular morphogenesis and migration speeds in angiogenesis.* PLoS computational biology, 2009. **5**(7).
29. Amit, P. and K. Sanjay, *Transforming potential and matrix stiffness co-regulate confinement sensitivity of tumor cell migration.* Integrative Biology, 2013. **5**.
30. Zaman, M.H., et al., *Migration of tumor cells in 3D matrices is governed by matrix stiffness along with cell-matrix adhesion and proteolysis (vol 103, pg 10889, 2006).* Proceedings of the National Academy of Sciences of the United States of America, 2006. **103**(37): p. 13897-13897.
31. Zaman, M., *The role of engineering approaches in analysing cancer invasion and metastasis.* Nature reviews. Cancer, 2013. **13**(8): p. 596-603.
32. Melo, E., et al., *Effects of the Decellularization Method on the Local Stiffness of Acellular Lungs.* Tissue engineering. Part C, Methods, 2013.
33. Crapo, P., T. Gilbert, and S. Badylak, *An overview of tissue and whole organ decellularization processes.* Biomaterials, 2011. **32**(12): p. 3233-3243.
34. Melo, E., et al., *Effects of the Decellularization Method on the Local Stiffness of Acellular Lungs.* Tissue engineering. Part C, Methods, 2013.

35. Tottey, S., et al., *The effect of source animal age upon extracellular matrix scaffold properties.* Biomaterials, 2011. **32**(1): p. 128-136.
36. Williams, C., Quinn, K. P., Georgakoudi, I. & Black, L. D. 1, *Young developmental age cardiac extracellular matrix promotes the expansion of neonatal cardiomyocytes in vitro.* Acta Biomaterialia 2014. **10**.
37. Badylak, S., D. Freytes, and T. Gilbert, *Extracellular matrix as a biological scaffold material: Structure and function.* Acta biomaterialia, 2009. **5**(1): p. 1-13.
38. Ren, H., et al., *Evaluation of two decellularization methods in the development of a whole-organ decellularized rat liver scaffold.* Liver international : official journal of the International Association for the Study of the Liver, 2013. **33**(3): p. 448-458.
39. Badylak, S., Lantz, G., Coffey, A. & Geddes, L. , *Small intestinal submucosa as a large diameter vascular graft in the dog.* The Journal of surgical research 1989. **47**: p. 74–80
40. Rieder, E., et al., *Decellularization protocols of porcine heart valves differ importantly in efficiency of cell removal and susceptibility of the matrix to recellularization with human vascular cells.* The Journal of thoracic and cardiovascular surgery, 2004. **127**(2): p. 399-405.
41. Cebotari, S., et al., *Detergent decellularization of heart valves for tissue engineering: toxicological effects of residual detergents on human endothelial cells.* Artificial organs, 2010. **34**(3): p. 206-210.
42. Du, L., et al., *Histological evaluation and biomechanical characterisation of an acellular porcine cornea scaffold.* The British journal of ophthalmology, 2011. **95**(3): p. 410-414.
43. Hung, S.-H., et al., *Larynx decellularization: combining freeze-drying and sonication as an effective method.* Journal of voice : official journal of the Voice Foundation, 2013. **27**(3): p. 289-294.
44. Nichols, J., et al., *Production and assessment of decellularized pig and human lung scaffolds.* Tissue engineering. Part A, 2013. **19**(17-18): p. 2045-2062.
45. Booth, A., et al., *Acellular normal and fibrotic human lung matrices as a culture system for in vitro investigation.* American journal of respiratory and critical care medicine, 2012. **186**(9): p. 866-876.
46. Kajbafzadeh, A.-M., et al., *Determining the optimal decellularization and sterilization protocol for preparing a tissue scaffold of a human-sized liver tissue.* Tissue engineering. Part C, Methods, 2013. **19**(8): p. 642-651.
47. Mirmalek-Sani, S.-H., et al., *Immunogenicity of decellularized porcine liver for bioengineered hepatic tissue.* The American journal of pathology, 2013. **183**(2): p. 558-565.
48. Ott, H., et al., *Perfusion-decellularized matrix: using nature's platform to engineer a bioartificial heart.* Nature medicine, 2008. **14**(2): p. 213-221.
49. O'Neill, J.D.e.a., *Decellularization of Human and Porcine Lung Tissues for Pulmonary Tissue Engineering.* The Annals of Thoracic Surgery 2013. **96**.
50. McPherson, T.B.B., S. F. , *Characterization of Fibronectin Derived from Porcine Small Intestinal Submucosa.* Tissue Engineering 1998. **4**: p. 75-83.
51. Yang, B., et al., *Development of a porcine bladder acellular matrix with well-preserved extracellular bioactive factors for tissue engineering.* Tissue engineering. Part C, Methods, 2010. **16**(5): p. 1201-1211.

52. Hodde, J., Badylak, S., Brightman, A. & Voytik-Harbin, S. , *Glycosaminoglycan content of small intestinal submucosa: a bioscaffold for tissue replacement.* Tissue engineering 1995. **2**: p. 209-17.
53. Voytik-Harbin, S., Brightman, A., Kraine, M., Waisner, B. & Badylak, S. , *Identification of extractable growth factors from small intestinal submucosa.* Journal of cellular biochemistry, 1997. **67**: p. 478–91.
54. Hodde JP, R.R., Liang HA, Badylak SF., *Vascular endothelial growth factor in porcine-derived extracellular matrix.* Endothelium., 2001. **8**(1): p. 11-24.
55. Johnson, T., S. Lin, and K. Christman, *Tailoring material properties of a nanofibrous extracellular matrix derived hydrogel.* Nanotechnology, 2011.
56. Freytes, D., et al., *Preparation and rheological characterization of a gel form of the porcine urinary bladder matrix.* Biomaterials, 2008. **29**(11): p. 1630-1637.
57. Sellaro, T., et al., *Maintenance of human hepatocyte function in vitro by liver-derived extracellular matrix gels.* Tissue engineering. Part A, 2010. **16**(3): p. 1075-1082.
58. Duan, Y., et al., *Hybrid gel composed of native heart matrix and collagen induces cardiac differentiation of human embryonic stem cells without supplemental growth factors.* Journal of cardiovascular translational research, 2011. **4**(5): p. 605-615.
59. DeQuach, J.e.a., *Simple and high yielding method for preparing tissue specific extracellular matrix coatings for cell culture.* PloS one 2009. **5**: p. e13039.

CHAPTER 2. Recapitulating the human tumor microenvironment in vitro: colon tumor-derived extracellular matrix promotes angiogenesis and tumor cell growth.

M. Romero-López[2], A. Trinh[2], C. Fimbres[2], M. Shuler[1], A. Sobrino[1], M. Keating[2], P. Ghearson[4], E. Botvinick[2,3], M. Digman[2], J.S. Lowengrub[5] , C.C.W. Hughes[1,2,3]

[1]Department of Molecular Biology and Biochemistry, School of Biological Sciences, [2]Department of Biomedical Engineering, The Henry Samueli School of Engineering, [3]The Edwards Lifesciences Center for Advanced Cardiovascular Technology, [4]Proteomics Mass Spectrometry Facility, [5]Department of Mathematics, University of California Irvine, Irvine, CA 92697

Abstract

Extracellular matrix (ECM) is an essential and dynamic component of all tissues and directly affects cellular behavior by providing both mechanical and signaling cues. Changes in ECM can alter tissue homeostasis, potentially leading to promotion of cellular transformation and the generation of tumors. Therefore, the study of ECM composition during cancer progression will be vital to the development of targeted treatments. In an effort to reproduce the native 3D cellular microenvironment, conventional approaches have utilized protein gels and scaffolds that incompletely recapitulate the complexity of native tissues. Here, we sought to address this lack of complexity by extracting and comparing ECM from normal human colon and colon tumor. We found differences in protein composition and stiffness, and observed significant differences in vascular network formation and tumor growth in each of the reconstituted matrices. We also studied free/bound ratios of NADH in the tumor and endothelial cells using Fluorescence Lifetime Imaging Microscopy (FLIM) as a surrogate for the metabolic state of the cells. We observed that cells seeded in tumor ECM (tECM) had higher relative levels of free NADH, consistent with higher a glycolytic rate, than those seeded

in normal ECM (nECM). These results demonstrate that the ECM plays an important role in the growth of cancer cells and their associated vasculature.

Introduction

The extracellular matrix (ECM) is a complex network of proteins and glycosaminoglycans that provides biochemical and biomechanical signaling cues to the cells it surrounds. ECM disruptions can occur in the physical (porosity, fiber orientation), biochemical (growth factor binding), and biomechanical (stiffness) properties of the ECM, and some of these properties help to regulate cell differentiation, adhesion, survival, fate, migration and proliferation rates [60] [12].

Cancer is one of the leading causes of death in the developed world and vast resources have been expended with the goal of understanding its root causes and to elucidate the intricacies of cancer progression in order to develop effective prevention and treatment strategies. There is a growing interest in the study of cell-matrix disruptions as these may contribute to cancer development by promoting cell dedifferentiation and cancer stem cell division. For example, the development of tumors has been linked to tissue inflammation, and this can induce the differentiation of fibroblasts into myofibroblasts. Myofibroblasts produce large amounts of ECM leading to tissue remodeling – also known as a desmoplastic reaction [12] – and this has been linked to tumor development.

Additional work is needed, however, to determine if this desmoplastic tissue precedes tumorogenesis or if it is a result of the interaction of cancer cells with stromal cells and ECM molecules. In response to tumor-derived signals stromal cells express numerous ECM

components, including collagens (I, III, IV, V, XII), proteoglycans and hyaluronan, which help recreate a more permissive environment for cancer propagation [17, 61-64]. As a result of these changes in the ECM, the fiber conformation is modified as well as the tumor tissue stiffness [17]. Evidence suggests that changes in ECM stiffness and fiber conformation can alter tumor growth and differentiation [4, 19, 65]. In particular, collagen can enhance cell proliferation and migration and, as a result, promote cancer cell proliferation, [29-31].

Both in vivo and in vitro approaches have been used to study the process of cancer progression. *In vivo* tumor models are ideal as they more closely reproduce the native evolution of cancer and its microenvironment. However, it is difficult to control the environment in these models, and visualization of cell-cell and cell-ECM interactions, and quantification of results is problematic without specific imaging technology [66]. In contrast, *in vitro* models are easier to manipulate, offering the opportunity to probe key biological features of several of the stages of cancer progression. However, 2D monolayer cultures have predominated and these fail to model key aspects of the tumor microenvironment, including 3D geometry/density of ECM binding sites, ECM heterogeneity, gradients of biochemical factors, spatial gradients, porosity, and density, among others.

Angiogenesis – the formation of new blood vessels from pre-existing vessels – is a critical feature of solid tumor growth that cannot be reproduced in a 2D environment. Without its own vasculature a tumor cannot grow beyond a few millimeters in size. The angiogenic process starts when tumor cells become hypoxic and those cells and stromal cells (fibroblast) secrete diffusible chemical signals, collectively called angiogenic factors. This process

activates the expression of matrix metalloproteinases (MMPs) – proteolytic enzymes that facilitate degradation of the ECM and basement membrane – by endothelial cells (EC), enabling their migration away from the parent vessel as a new sprout. ECM morphology and fiber orientation have strong effects on EC migration, sprout extension rate and vascular characteristics [28, 67-69].

It is now well established that 3D *in vitro* experiments provide a better approximation of the *in vivo* tumor cell microenvironment than do 2D cultures [45]. It has been shown that cancer cell morphology [20, 70], cell movement [8, 9], cell proliferation rates [71], gene expression [72] and function [73, 74] are all different in 2D versus 3D cultures. In particular, 3D *in vitro* experiments of tumor spheroids showed upregulated expression of angiogenic factors compared to cells seeded in 2D [75, 76], while other work demonstrated that cells in a 2D environment have a lower drug response than cells in 3D [77]. Finally, it is well known, from the results of Bissell and collaborators, that tumor cells de-differentiate when cultured in 2D, whereas in 3D cultures they adopt amorphous morphologies similar to the ones seen *in vivo* [4]. These are just some examples of the importance of studying tumor cells in the correct context [18].

Recent work looking at tumor cells in a 3D setting *in vitro* have focused on tumor cells or tumor spheroids, grown in Matrigel, collagen or fibrin [78, 79]. However, collagen and fibrin are single ECM components and do not capture the complexity of native human ECM. In contrast, Matrigel, which is extracted from Engelbreth-Holm-Swarm (EHS) mouse sarcoma

[80, 81], has a more complex composition. However, it is highly enriched for laminin 111, but lacks the substantial amounts of collagen normally seen in tumor matrix [82].

In order to improve ECM consistency, advances in 3D artificial biomimetic structures from tissue engineering are being developed. These structures mimic key features of the ECM while enabling the control of physical and biochemical properties including protein content, pore size, stiffness and embedded growth factors. Examples include hydrogel systems (e.g. cross-linked peptide-based gels) [83-85], tissue extracted ECM gels [37, 56], and cell derived matrices [86, 87]. Importantly, hydrogels containing ECM extracted from tissues using decellularization techniques contain almost all of the protein of native tissues and in the correct protein ratios. Furthermore, these gels allow for other tunable features such as rheological properties and fiber density, [88, 89]. Additionally, through polymerization, these gels form three-dimension scaffolds similar to collagen and fibrin gels. [55, 56].

Here, we focus on reproducing the native ECM microenvironment by decellularizing, both normal and tumor tissues for incorporation into 3D hydrogels. We found that normal (n)ECM and tumor (t)ECM have different protein composition, with the tumor-derived ECM having some additional protein components. We found significant differences in vascular characteristics and tumor growth in the different matrices, and additionally, using fluorescence lifetime imaging microscopy, noted a dramatic shift to a more glycolytic metabolism in tumor cells growing in tECM versus nECM.

Materials and Methods

Materials, cells and animals

Endothelial growth medium-2 (EGM-2) was obtained from Lonza (Basel, Switzerland), DMEM was from Corning (Corning, New York), Fetal Bovine Serum (FBS) was from Gemini Bio Products (Sacramento, California). Sodium deoxycholate (SDC), Triton-X100 and pepsin were from Sigma-Aldrich (St. Louis, Missouri), sodium dodecyl sulfate (SDS) was from Bio-Rad (Irvine, California), DNAse was from Worthington (Lakewood, New Jersey), Antibiotic-Antimycotic, 1X and 10X Dulbecco's phosphate buffered saline (DPBS) and Trizol were obtained from Life Technologies (Carlsbad, California). An ultra-fine cheese grater was purchased from Amazon.com (Seattle, Washington). Fibrinogen 90% clottable bovine was from MP Biomedicals (Santa Ana, California), thrombin (1.3 Units/ml) was from Sigma-Aldrich (St. Louis, Missouri) and polydimethylsiloxane (PDMS) was from Dow Corning (Midland, Michigan). The centrifuge was from Beckman-Coulter (Brea, California). A plate reader was bought from BioTek (Winooski, VT). 96-well low attachment plates were purchased from Cornining (Corning, NY). TURBO DNA-free kit was obtained from Thermo Fisher Scientific (Waltham, MA). iScript cDNA Synthesis Kit and Precast Polyacrylamide Gels were from BioRad (Hercules, California). And gene primers were synthesized by Integrated DNA Technologies (Coralville, Iowa). Optimum cutting temperature compound (OCT) was purchased from VWR International (Radnor, PA).

A Ti:Sapphire laser Mai Tai was from Spectra Physics (Irvine, California) and a LUMPlanFl 40x/0.80 W objective was from Olympus (Tokyo, Japan). An LTQ Velos Pro mass analyzer was from Thermo Fisher Scientific (Waltham, Massachusetts), the Mascot Distiller 2.5.0 and Mascot Server 2.5.0 were from Matrix Science (Boston, Massachusetts).

MATLAB was purchased from Mathworks (Natick, Massachusetts) and GraphPad Prism was bought from GraphPad Software (La Jolla, California). An Olympus 1X70 inverted microscope and an Olympus FluoView FV1000 were from Olympus (Cypress, California). And SPOT microscopy software from (Sterling Heights, Michigan).

Endothelial colony forming cells (EC) were isolated from human umbilical cords were obtained from the University of California, Irvine Medical Center, following an Institutional Review Board-approved protocol and using the protocol described in [90]. The normal human lung fibroblasts (NHLF) were purchased from Lonza (Basel, Switzerland) and colon tumor cell lines (SW620, SW480, HCT116) were obtained from UC Irvine's Chao Family Comprehensive Cancer Center. EC were cultured in EGM-2 and used between passages 4-8. NHLF (used between passages 4-8), SW620 and HCT116 were cultured in DMEM containing 10% FBS. All cells were cultured at 37 °C, in a 5% CO_2 incubator. The EC and cancer cells were transduced with lentivirus expressing mcherry and GFP (LeGO-C2 (plasmid # 27339), LeGO-V2 (plasmid # 27340), which were gifts from Boris Fehse (Addgene, Cambridge, Massachusetts)

Human anonymous discarded colon tissue and tumor tissue were obtained from the Medical Center, University of California Irvine, following an Institutional Review Board-approved protocol.

NOD/SCID mice were purchased from Jackson Laboratories, Bar Harbor, ME. All in vivo studies were completed under the approval of the IACUC committee at the University of California, Irvine.

Methods

Human colon submucosa decellularization.

Human discarded colon tissue was obtained from the University of California Irvine Medical Center following an Institutional Review Board-approved protocol. The tissue was frozen at -80^{o}C for at least 48 hours for cell lysis. The tissue was then thawed in sterile ddH_2O for one hour, and the colon submucosa was isolated by mechanically removing the fat, mucosa and the colon muscle layers. The submucosa was cut into small pieces (approximately 3mm length) and washed with ddH_2O for 1 hour. The tissue was then washed with 2X phosphate buffer solution (PBS) for 1 hour and washed with 2% sodium deoxycholate (SDC) for six days (our previous studies with porcine colon submucosa using 1% sodium dodecyl sulfate (SDS) resulted in low collagen content compared with the 2% SDC treated and SDC is recommended to be used in thin tissues [37]). The tissue was washed in 1% Triton-X100 for 30 minutes and rinsed in ddH_2O 10 times for 20 minutes each to remove any remaining detergent. This was followed by a wash in 1X PBS with 1% Antibiotic-Antimycotic for 24 hours at 4^{o}C. All washes were performed in a stir plate at 350 rpm.

Human liver metastasis decellularization.

Human discarded tumor tissue was obtained from the UCI Medical Center following an Institutional Review Board-approved protocol. Similar to colon submucosa decellularization, this tissue was stored at -80^{o}C for at least 48 hours prior to use, and washed for 1 hour in

ddH20. Then, the tissue was washed with 2X PBS for one hour and washed with 1% SDS for 4 days. After that, it was washed for 30 minutes with 1% Triton-X100, washed in 100U of DNAse and then rinsed with ddH20 water for 20 minutes, 10 times. This was followed by a wash in 1X PBS with 1X Antibiotic-Antimycotic for 24 hours at 4^{o}C. All washes were done on a stir plate at 350 rpm.

Decellularization confirmation

Random decellularized tissue pieces were selected and fixed in 4% paraformaldehyde (PFA). The tissue pieces were send to the Department of Pathology, University of California Irvine (UCI) and were embedded in paraffin and cut into 4-μm slices. Finally, hematoxylin and eosin stain was performed.

Colon submucosa and tumor ECM gels preparation

Decellularized tissue was frozen in liquid nitrogen and lyophilized for 3 to 4 days until the tissue was completely dry. Then, the tissue was milled using an ultra-fine cheese grater. The ECM tissue powder (100 mg) was enzymatically digested by mixing it with 20 mg of pepsin in 10 ml of 0.1 N HCl to a final ECM solution of 10 mg/ml. The ECM solution was diluted in 10X DPBS resulting in a final ECM concentration of 8 mg/ml. Finally, 1N NaOH was added to bring the solution to pH 7.4.

Vasculogenesis assays in 3D fibrin and ECM gels

A solution of 8 mg/ml of fibrinogen in 1X DPBS was used for both the fibrin and the ECM-fibrin gels. Both normal colon ECM (nECM) and tumor ECM (tECM) gels were made by mixing 37.5 μl (75%) of normal or tumor ECM solution with 12.5 μl (25%) of fibrin. ECs transduced to express mCherry (1 x 10^6 cells/mL) were co-suspended with 2 x 10^6 cells/ml

fibroblasts before polymerization. The gel/cell solutions were mixed with 5 μl of thrombin (1.3 Units/ml thrombin), and pipetted into a polydimethylsiloxane (PDMS) ring (8 mm radius and 0.8 mm height)[91] attached to a 6-well glass-bottom plate and incubated at 37°C for 2 hours. Then 3 ml EGM-2 media was added on the top of the gels of the three conditions: fibrin, nECM and tECM gels. The plate was kept in the incubator at 37°C for the duration of the experiment. EGM-2 media was changed at day 3 and day 5 in all the conditions. Microscope images were taken at day 2, 4 and 8. All experiments were performed in triplicate.

Colon tumor cell growth assay

GFP- transduced SW620 cells were trypsinized, counted, and centrifuged, 2 x 10^5 cells/ml were resuspended in the nECM or the tECM to a final concentration of 2 x 10^5 cells/ml. The gel/cell solutions were mixed with 5 μl of thrombin pipetted into PDMS rings and attached to a 6-well glass-bottom plate (3 gels per well). The gels were incubated at 37°C for 2 hours for polymerization prior to the addition of 3 ml EGM-2 media on the top of the gels. Media was changed at day 3 and day 5. The plate was kept in the incubator at 37°C for the duration of the experiment. For tumor growth quantification, colon tumor cell (GFP-labeled SW620) cumulative size was measured by the intensity of the tumor cells using a plate reader on day 2, 4 and 8. All experiments were performed four times in triplicates.

Tumor spheroid-angiogenesis assay preparation

Fibroblasts and GFP transduced SW620 cells were trypsinized, counted, and centrifuged (Beckman-Coulter, Brea, California). The cells were mixed in a solution of DMEM with 10% FBS and 15% methylcellulose at a ratio of 3:1 (Fibroblasts: SW620). Spheroids of 1000 cells were made by pipetting 150 μl of the suspension into each well of a 96-well low attachment plate and incubating for 24 hours at 37°C. Spheroids were harvested into a 1.5 ml

Eppendorf tube, and the supernatant was aspirated. Eight spheroids were added to the protein/cell suspension (2 x 10^6 cells/mL mCherry-labeled EC, 2 x 10^6 cells/ml fibroblasts) before casting the gels. The protein/cell solutions were mixed with 5 μl of thrombin, pipetted into a PDMS ring and attached to a 6-well glass-bottom plate. The gels were then incubated for 2 hours at 37°C, prior to the addition of EGM-2 media on the top of the gels of the two conditions, the nECM and tECM gels. EGM-2 media was changed at day 3 and day 5 in all the conditions. All experiments were performed three times in triplicates.

Quantitative RT-PCR

At day 10 of the colon tumor growth assay, the gels of each condition were harvested and digested with Trizol following the manufacture's protocol for RNA isolation. RNA was treated with DNAse (TURBO DNA-free kit for 30 minutes. Then 5 μg of RNA were used for the generation of cDNA with the iScript cDNA Synthesis Kit. QPCR was performed with SYBR green chemistry and the BioRad CFX96 qPCR system. Primers of the genes Hexokinase 1 (HK), Pyruvate Dehydrogenase Kinase (PDK1) and Solute Carrier Family/Facilitated Glucose Transporter Member 1 (SLC2A1/GLUT1) were used for gene expression analysis.

mRNA expression levels were normalized to the expression of the cells seeded in the nECM and measured four times. The figure shows the fold changes, the standard error of the mean and the statistical significance is shown as *$p<0.05$.

Collagen fiber visualization through Second Harmonic Generation (SHG)

To visualize the collagen fiber morphology and distribution, second harmonic generation acquisition of the normal colon submucosa and the tumor tissue was performed using the system developed by the Laboratory of Fluorescence Dynamics (LFD) at UCI [92] before and after decellularization, as well as after digestion. A Ti:Sapphire laser (Mai Tai, Spectra Physics, Irvine, California) was used for two-photon fluorescence excitation, with a wavelength of 810 nm and an incident power in the sample of 20mW. The signal was collected using a long working distance water objective (LUMPlanFl 40x/0.80 W, Olympus, Tokyo, Japan) with a field of view of 110um. The SHG signal was obtained using a bandpass filter 320-390 nm.

SDS-page

To further characterize the colon and tumor ECM gels, the ECM solutions were separated by SDS-PAGE using a Pre-cast Polyacrylamide gel and stained with Coomassie Brilliant Blue to visualize proteins present in the ECM.

Mechanical analysis of the three-dimensional gels

Laser optical tweezers-based active microrheology (AMR) was performed in the laboratory of Dr. Botvinick, UCI. 2 μm beads were embedded into the different matrix solutions. After the gels were polymerized, the beads were then trapped by the laser resulting in oscillation at different frequencies with an amplitude of 60 nm; the amplitudes were recorded and the complex shear modulus (G) was calculated as previously described by Kotlarchyk et al. [93].

NanoLC-MS/MS

Decellularized normal and tumor tissues were treated as described by Fong, et al. except that the resulting peptides from each tissue, after treatment with iodoacetamide and trypsinized as described [94], were subjected to Nanoscale liquid chromatography coupled to tandem mass spectrometry (nanoLC-MS/MS) using an LTQ Velos Pro mass analyzer. The mass analyzer was connected to a nanoLC-Easy1000, with peptide separation in an in-house-packed 25 cm x 75 μm ID C18 nanospray tip. Peptides were resolved in segmented solvent gradients running from 6 to 35% Acetonitrile (CH_3CN) in 0.1% formic acid over 135 min.

Fourier Transform Mass Spectrometry (FTMS) precursor spectra were acquired at 60,000 resolution, and up to 20 of the most intense ions with charge states of +2 and higher in each precursor spectrum were subjected to rapid collision induced dissociation (CID) fragmentation and ion trap analysis. Spectral data were re-calculated using Mascot Distiller 2.5.0 and the resulting peaklists were searched against SwissProt (July 2014) with *Bos Taurus* taxonomy along with a database of common contaminants using Mascot Server 2.5.0, with Carbamidomethyl (C) and Oxidation (M) as fixed and variable modifications, respectively, and precursor and fragment mass tolerances of 10 ppm and 0.25 Da, respectively. Mascot protein score and exponentially modified protein abundance index (emPAI) values in Mascot results were compared between samples using in-house software.

Vessel quantification

AngioTool (NCI) was used to quantify the vasculogenesis assay (vessel area, vessel length, number of branches). The vessel diameter and fractal dimension quantification was performed using the MATLAB (Mathworks, Natick, Massachusetts) subroutine, RAVE, developed by Seaman *et al.* [95]

Imaging

Fluorescent images were collected through the Olympus (Cypress, California) 1X70 inverted microscope with SPOT software (Sterling Heights, Michigan). Confocal images were obtained using a confocal microscope (Olympus FluoView FV1000, from the LFD).

Florescence lifetime imaging (FLIM)

FLIM data was acquired on a Zeiss LSM 710 (Carl Zeiss, Jena, Germany) microscope using an EC Plan-Neofluar 20x/0.50 N.A. objective (Carl Zeiss, Oberkochen, Germany). NADH was excited by an 80 MHz Titanium:Sapphire Mai Tai Laser (Spectra-Physics, Santa Clara, CA) at 740 nm. Tumor spheroids and (2×10^6 cells/mL mCherry-labeled EC, 2×10^6 cells/ml fibroblasts) embedded in the nECM and tECM were imaged. In detail, images (256 x 256 pixels) of individual tumor cells from the borders of the tumor spheroids closer to the vasculature, were collected with a scan speed of 25.21 μsec/pixel. The experiments were done in triplicate and nine images were taken per condition in each experiment.

Fifty frames were collected and integrated for each fluorescence lifetime image. The excitation and emission signals were separated by a 690 nm dichroic mirror, and a 460/80 bandpass filter and photomultiplier tube (H7422P-40, Hamamatsu Photonics, Hamamatsu, Japan) were used for detection. Frequency domain FLIM data was acquired by the A320 FastFLIM FLIMbox (ISS, Chamgaign, IL) and analyzed by SimFCS software (LFD, Irvine, CA, www.lfd.uci.edu).

Fluorescence lifetime images were analyzed by the phasor approach, as previously described in [96], [97]. Briefly, every pixel of the integrated FLIM image was transformed into

a point on the phasor plot. The g and s coordinates in the phasor plot were calculated from the sine and cosine components of the Fourier transform of the fluorescence intensity decay of each pixel in the image. By NADH FLIM phasor analysis, we mapped the free to protein bound NADH distribution in the images, which was correlated to the metabolic status of the biological sample [97]

In vivo mice studies

GFP- transduced SW620 cells were resuspended in 100 µl of nECM or tECM to a final concentration of 3 x 10^7 cells/ml. Eight ten-week-old NOD/SCID mice were shaven on the lower left and right flanks, just above the hind limbs. The cell/ECM mixture were implanted subcutaneously: cells/nECM on one side and cells/tECM mixture on the other side of each mouse. Mice were measured biweekly for tumor growth. Tumor Volume was calculated by the formula [(Length x $Width^2$)/2]. Tumors were allowed to grow for 5 weeks, then the mice were euthanized, and tumors harvested. The tumors were cut in half. One half of each tumor was fixed in 4% PFA and embedded in paraffin and cut in sections by the Department of Pathology UCI for immunohistochemistry (IHC) analysis. And the other half of each tumor was embedded and frozen in OCT immediately after harvest and cut in slides of 60 µm for FLIM analysis.

Immunohistochemistry analysis for CD31

Staining and quantification was done exactly the same way as described in [98]. In brief, EC inside the tumor sections were visualized by staining for CD31+ cells. The total percent vascular density of the tumors was calculated by determining the area of CD31+ cells versus the entire area of the section using ImageJ. The sections were imaged to obtain the

vascular density for each image of the tumor. The degree of vascularization was calculated at a distance of 20, 40, 60, 80, and 100 % into the tumor (where 100 % was considered the center of the tumor) using Image J.

Statistics

Data are represented as mean +/- standard deviation, except where otherwise stated. Statistical data analysis was determined using and unpaired t-test with n=3 and a 95% confidence interval. Statistical calculations were performed using GraphPad Prism (GraphPad Software, La Jolla, California).

Results

Preparation of extracellular matrix gels

An overview of ECM gel preparation is provided in Fig 1. Previous work has indicated that individual tissues must be treated with unique protocols during the decellularization process to maintain the chemical properties unique to each tissue [37]. We confirmed this as both normal colon and colon tumor tissues required different decellularization protocols. The normal colon tissue was treated with 2% SDC as a less aggressive detergent optimized for thin tissues, while harsher 1% SDS was necessary to decellularize the thick, bloody tumor tissue.

Characterization of normal ECM and tumor ECM

We obtained our tumor tissue from colon tumors that had metastasized to liver. Primary colon tumor tissue is very hard to obtain as most primary tumors receive neoadjuvant treatment before surgical removal and are then unsuitable for our use. Regardless, work on ECM proteomics from the Hynes laboratory indicates that ECM from colon metastases in liver is more similar in composition to colon ECM than it is to the liver itself [99].

To confirm that complete decellularization was achieved in colon and tumor tissue, hematoxylin and eosin (H&E) staining was performed (Fig. 2A, 2B). Random sections were chosen and an absence of nucleic acids was observed (Fig. 2C, 2D). The second harmonic signal from the non-centrosymmetric collagen structure was used to visualize the collagen fibers in the colon and tumor tissues before decellularization, and after gel polymerization. The collagen fibers can be visualized in white to light blue (Fig. 2E - H) in the tissues before the decellularization process as well as in the reconstituted gels. It is clear that the gels are representative of the native architecture of the original tissues. SDS-page gels were run for both of the solubilized ECMs, and bands at the molecular weight of collagen I were observed, suggesting the presence of collagen I in our ECMs (data not shown). Both, nECM and tECM SDS-page profiles have a unique protein profile; in particular, extra bands at higher molecular weights in the tECM were observed (data not shown).

Normal ECM supports vascular network formation

To determine if nECM was able to support new vessel formation, fibroblasts and EC expressing mCherry (2 million/ml, 1 million/ml respectively) were suspended in nECM and in control fibrin gels. After 4 to 8 days extensive formation of lumenized vessels was observed in both the control (fibrin) and nECM gels (Fig. 3A). Several important features of the vascular networks were quantified using Angiotool software (NCI), including total vessel length, vessel area, number of branches and vessel diameter. In the quantification of these parameters, no significant difference was found between the nECM and vascular networks in fibrin, although there was a trend toward greater vascularity in fibrin, indicating that the vessels formed in nECM gels were comparable to those formed in fibrin gels (Fig. 3B-E).

Tumor ECM promotes the formation of tumor-like vasculature

In order to examine if the tECM could support the growth of new vessels, we followed the same procedure as for nECM. Fibroblasts and mCherry-EC (2 million/ml, 1 million/ml respectively) were suspended in each of the gels at a ratio of 2:1, and vessel formation was tracked for 8 days (Fig 4A). Again, we quantified several vascular network characteristics, and significant differences between the two conditions were found. Total vessel length, vessel area and the number of branches were significantly higher in the tECM when compared to nECM – by almost 2-fold by day 2 (Fig. 4B-D). Furthermore, vessel diameter was increased in the vessels grown in tECM (33.92 μm ± 3.71) compared to those in nECM (22.91 μm ± 2.35) (Fig. 4E. Overall, we found greater variability of vessel diameter in the tECM, as indicated by the higher standard error; this is consistent with observations in human patient tumor-vasculature compared to vasculature in matched normal tissues [100]. The fractal dimension, which is a mathematical measure that quantifies the complexity of a network, was also higher in tECM vascular networks (Fig. 4F. This last observation also agrees with what has been found *in vivo* in tumor vasculature [95]. Therefore, the vessels grown in tECM mimicked tumor vasculature, both in variability of vessel diameter within the network and fractal dimension.

Normal ECM and Tumor ECM have proteins in common, but tumor ECM has additional components

To determine protein composition of both ECMs, mass spectrometry was performed. Data from the nano-LC MS/MS was depurated with a threshold score and compared between nECMs and tECM. Mass spectrometry revealed that both ECMs have some proteins in common, including collagen I, IV, elastin, laminin, heparan sulfate, and vitronectin. However, the tECM contains additional proteins, such as tenascin-C, periostin, and fibrinogen (Table 1).

Microrheological measurments of normal ECM and tumor ECM

Microrheology was performed on both ECMs using AMR. The measurements were taken at random locations within the samples. Amplitude data was collected and analyzed. The ECMs display the storage modulus's (G') and loss modulus showed in Table 2.

Colon tumor spheroids grow faster in tumor ECM

Colon tumor cells (GFP-labeled SW620) and EC (mCherry) were incorporated into either nECM or tECM (Fig. 5). The tumor cells tended to grow more compactly in the nECM (Fig. 5A), whereas they were more diffuse in the tECM (Fig. 5B). Differences in vascular growth have been noted above (Fig. 4). Tumor growth was then followed by measuring the intensity of GFP using a plate reader. By 9 days we saw a significantly faster growth of the tumor cells in tECM compared to those in nECM (Fig. 5C). We also subcutaneously injected tumor cells in matrix into immunocompromised mice and examined their subsequent growth.

Although there was an early, non-significant increase in the tECM this difference soon disappeared (data not shown). It is likely that invading mouse fibroblasts rapidly remodeled the nECM into tumor ECM under the influence of the tumor cells.

Both tumor cells and endothelial cells are more glycolytic in tumor ECM than in normal ECM

Fluorescence Lifetime Imaging Microscopy (FLIM) is a label-free imaging modality that when coupled with the phasor approach to data analysis can report on free/bound NADH ratios at single pixel resolution. A higher free/bound ratio of NADH has been shown to correlate with a higher level of glycolysis within cells [97]. We used FLIM to examine the metabolic profile of the SW620 colon cancer cells and the EC of the surrounding vasculature in different ECMs. We identified each cell type by its expression of green (tumor) or red (EC)

fluorescent proteins (Fig. 6A, B) and used this to generate masks for FLIM analysis of the tumor cells (Fig. 6C, D) and the EC (Fig. 6E, F). The associated phasor plot is shown in Fig. 6G. We found a higher relative level of free NADH in both the tumor cells and the EC when they were embedded in tECM (blue/white) compared to nECM (Fig. 6H, I), consistent with higher levels of glycolysis. This observation is also consistent with previous work in orthotopic colon tumors and their adjacent vessels in mice [101]. Importantly, the effect of tumor matrix on the NADH free/bound ratio was also seen when we used two other colon cancer cell lines, SW480 and HCT116 (data not shown). We next extended these studies to tumors *in vivo*. SW620 cells in either nECM or tECM were injected subcutaneously into immunocompromised mice and then harvested after 5 weeks for FLIM analysis. Similar to our *in vitro* findings we saw a strong increase in the free/bound ratio of NADH in tumor cells growing in the tECM compared to the nECM, again suggesting that these cells are more glycolytic in the tumor matrix microenvironment.

Tumor ECM promotes higher expression of genes associated with glycolysis

To provide further evidence that the nature of the ECM can influence cellular metabolism we examined expression of several genes associated with glycolysis, including the glucose transporter GLUT1 (*SLC2A1*), Hexokinase (*HK1*), and Pyruvate Dehydrogenase Kinase 1 (*PDK1*). After 10 days of culture, tumor cells seeded in tECM had higher expression of these genes compared to cells in nECM (Fig. 6J), consistent with the increase in free NADH seen by FLIM and in line with the known preference of tumor cells to favor aerobic glycolysis over oxidative phosphorylation (Warburg Effect) [102].

Discussion

Decellularization has recently become a valuable tool to study ECM and its interactions with different cell types, both in the context of biomaterials, and in the field of regenerative medicine. Decellularization has been successfully employed in a variety of tissues, including cornea [42], larynx [43] , lung [44, 45], liver [46, 47], and heart [48]. Importantly, as was found in our study, these different tissues require unique decellularization protocols to preserve the chemical composition of the native tissues. To our knowledge, this is the first time that human normal colon and cancer tissues have been decellularized for 3D ECM studies. Since normal colon and tumor tissue differ in thickness and density, it is not possible to decellularize them using the same protocols, necessitating the optimization of unique protocols for each tissue.

An alternative technique to obtain hydrogels was introduced by Badylak and colleagues [103] where they developed an ECM gel from the decellularized small intestine submucosa by lyophilizing, powderizing and digesting the tissue, resulting in a solution that could be used as an injectable graft. In earlier studies it was found that these gels could be used as an *in vitro* scaffold – a urinary bladder extracted gel supported adhesion and growth of rat aortic smooth muscle cells *in vitro* [56]. Some years later, a porcine liver-derived gel was extracted and used successfully for culturing human hepatocytes *in vitro* [57]. In addition, a heart-extracted scaffold was used to induce differentiation of pluripotent stem cells into cardiomyocytes without the use of growth factors [58], while a similar scaffold was used to differentiate human embryonic stem cells into cardiomyocytes [59].

These studies suggest that the complexity and uniqueness of the native extracellular matrix is a key feature for the study of not only "normal" cell behavior *in vitro* but also that of tumors. Thus, as Ghajar and Bissell have described [104], there is a need for a better tumor-engineered platform to study the interactions of the tumor cells, vasculature and ECM, particularly in light of emerging evidence of the critical role that ECM plays in the tumor microenvironment. For example, this is well documented by Bissell and collaborators for breast tumors [4, 20], where they find that the cell environment can be as important as the cell genotype. Cells sense the ECM through integrins and these signals are transmitted through the cytoskeleton, leading to changes in gene expression and adaptation to the cells' local environment. Thus, the local microenvironment can lead to changes in both cell phenotype and genotype [18].

Changes in the tumor ECM, such as extra deposition and crosslinking of the collagen fibers, are the result of cross-talk between the tumor cells and the tumor-associated stromal cells [105]. These cells express lysil oxidase (LOX), which crosslinks collagens and elastin, resulting in increased stiffness [17, 105]. In this study we also observed differences in collagen fiber structure between the normal tissue and the tumor tissue (Fig. 2). We found the collagen fibers in the tumor tissue to be more linearized and aligned in comparison to collagen fibers in nECM, which were curly and anisotropic, as described in [105]. Our mass spectrometry data revealed further changes in the tECM composition compared to nECM. We noted the presence of several proteins, such as periostin, tenascin-C and fibrinogen, in the tECM that have been directly linked to tumor progression and poor prognosis [106-108]. Additionally, using active microrheology, we observed changes in stiffness between the two reconstituted hydrogels, the

tECM being almost 3-fold stiffer than the nECM. It has been documented that tumor tissues are stiffer than normal tissues – for example, breast tumor ECM is stiffer at least three times stiffer than normal ECM [109, 110]. It is hypothesized that these changes in the tissue stiffness are the result of excess fiber crosslinking and changes in ECM composition [110].

Several groups have studied blood vessel formation or vasculogenesis in different ECM proteins (collagen or fibrin) or in Matrigel [111-114]. However, our study is the first to show *in vitro* vascularization of a normal human tissue-derived hydrogel (nECM) or a tECM. We observed that nECM supports vessel formation as well as fibrin, which has been widely use for tissue engineering applications such as vascularized tissue grafts [66]. A vascularized platform has numerous applications in the tissue-engineering field, such as a platform for *in vitro* disease models, for *in vitro* drug testing, and also for *in vivo* tissue regeneration. Moreover, since tumors require new blood vessels *in vivo* to continue growing beyond a certain size, being able to develop a capillary network in a natural hydrogel would allow us to more closely mimic the *in vivo* tumor niche. To this end we developed a vascularized tissue in a human tumor ECM hydrogel. Unfortunately, supply of primary colon tumor tissue is limited as most patients receive neoadjuvant therapy before resection, making the tumors unsuitable for decellularization. We therefore used colon tumors that had metastasized to liver. Importantly, an ECM proteomics study from the Hynes laboratory has shown that ECM from colon liver metastases is more similar in composition to colon ECM than it is to liver ECM [99].

In our study, we found that the capillary networks developed in tECM had similar characteristics to the *in vivo* tumor vasculature. Recent work looking at vasculogenesis in

different ECM materials such as collagen or/and fibrin [115] [69], have revealed that at higher concentrations, and increased stiffness, the degree of vascularization is decreased and the average vessel diameter is significantly reduced [116]. However, in our studies we have seen an increase in vessel density, sprouting and vessel diameter in tECM, even though this is 3-fold stiffer than the nECM. This suggests that differences in ECM composition are more important than the stiffness for regulating vessel formation. From the mass spectrometry analysis, we identified tenascin-C in the tECM but not nECM. It is known to be abundant in tumor tissues and to have an important role in endothelial proliferation and vessel malformations [117]. It is also well known that ECM can bind to several growth factors, making them available to cells during matrix proteolysis. These growth factors can stimulate endothelial cells enhancing vasculogenesis or angiogenesis [118, 119]. In addition to the endothelial cells, tumor cell growth was also significant increased in the tECM. This could be due to the mechanical properties of the tECM or to the composition. Tumor cells are known to proliferate and migrate more in stiffer substrates [120].

In order to investigate the correlation between ECM and cell metabolism we used FLIM as a measure of cell metabolic activity. We found significant differences in cells grown in the two matrices. Specifically the free/bound ratio of NADH was higher in cells in tECM, consistent with higher rates of glycolysis. This is in line with findings in tissue biopsies where the FLIM signature of the cells in tumor tissues indicates that these cells are more glycolytic than cells in normal tissues [17]. Consistent with changes in FLIM, we found significant differences in gene expression in the cells seeded in tumor ECM. The up-regulation of GLUT1 and HK gene expression in tECM supports the increase in glucose uptake and glycolysis in

tECM compared to nECM. The increased expression of PDK1 (a negative regulator of PDH) favors a reduced entry of glucose into the TCA cycle and a reduced rate of OxPhos, consistent with the preference of many tumors for aerobic glycolysis over OxPhos (see below). It is now well established that the metabolic properties of tumor cells are different from those of normal cells [121], and although the molecular mechanism is still not well understood, it is well accepted that cancer cells are more dependent on aerobic glycolysis than on glucose oxidation, and this is independent of oxygen availability, a preference known as the Warburg effect [102].

Here we have demonstrated how the tumor microenvironment participates in this malignant phenotype. Our data identify the tumor microenvironment as an important factor in the regulation of tumor cell metabolism, supporting the work of others, and emphasizes the possibilities of targeting the 3D tumor microenvironment as a way of controlling tumor growth [122, 123].

In summary, we have demonstrated that the composition (and possibly stiffness) of the ECM has a dramatic effect on both tumor cells and the vasculature that supports them. Tumor-derived matrix supports an altered metabolism, shifting cells towards aerobic glycolysis, as well as enhanced tumor cell proliferation. In addition, vascular network formation is profoundly altered, with increased vessels length but also increased vascular heterogeneity. These studies suggest that targeting the tumor ECM may be a useful adjunct to more direct anti-tumor cell therapies.

Figures

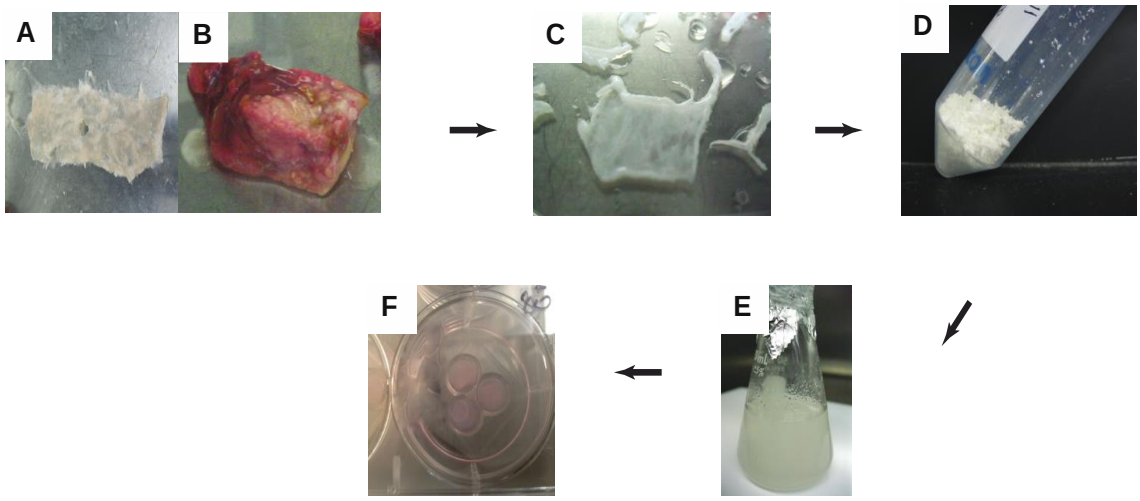


Figure 2.1.ECM hydrogel extraction process. (A) Human colon tissue and (B) colon tumor metastasis were cut into pieces, (C) decellularized with the use of several detergents, (D) lyophilized and powderized. Finally, (E) the ECM was digested with pepsin and HCL. The ECM solution polymerizes at 37° C at 7.5 pH forming (F) ECM hydrogels of colon and tumor tissues in PDMS rings.

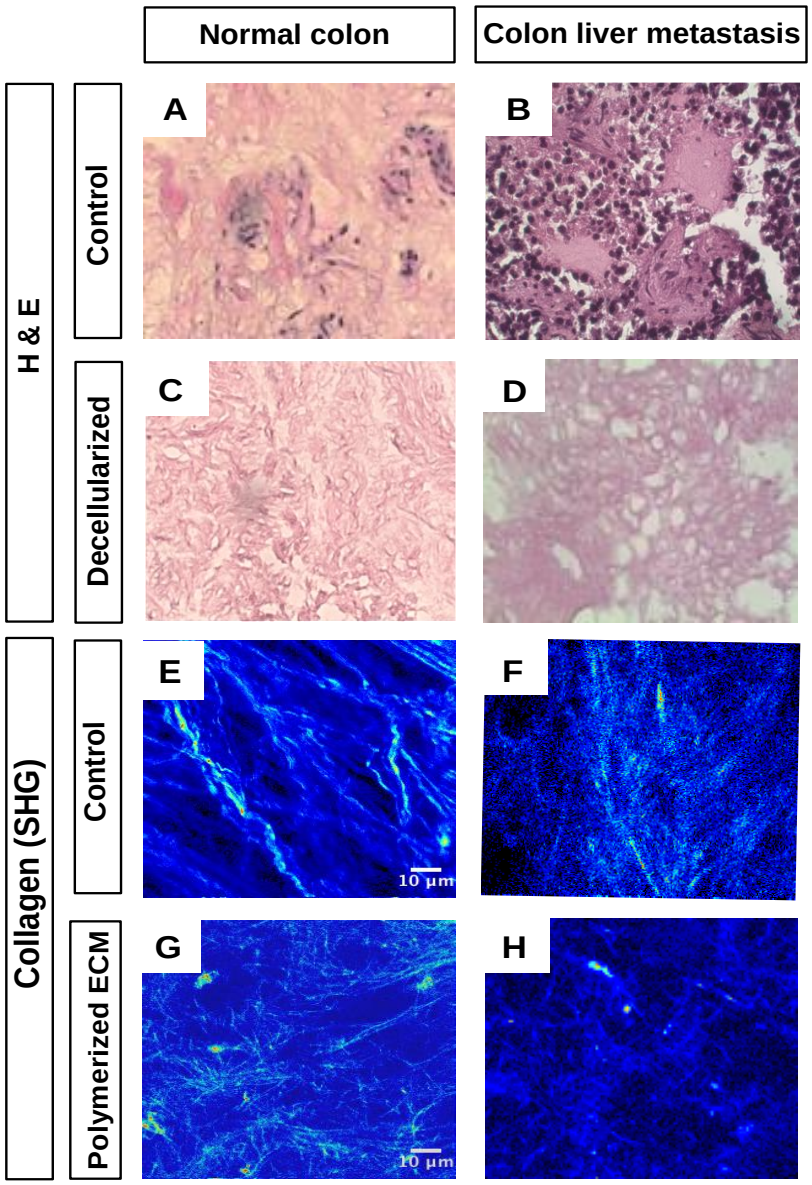


Figure 2.2 Characterization of the ECM from the human normal colon and the human colon liver metastasis. (A, C, E, G) Normal colon tissue. (B, D, F, H) Colon liver metastasis tissue. (A, B) Tissue before decellularizatin. H&E stain. (C, D) Tissue after decellularization. H&E stain. There is no cellular nuclei (purple) or debris present, indicating complete decellularization. (E, F, G, H). Second harmonic generation (SHG) of collagen fibers (in white to light blue) showing that the collagen is still present after decellularization and polymerization in the ECM hydrogels. Scale bar= 10 µm.

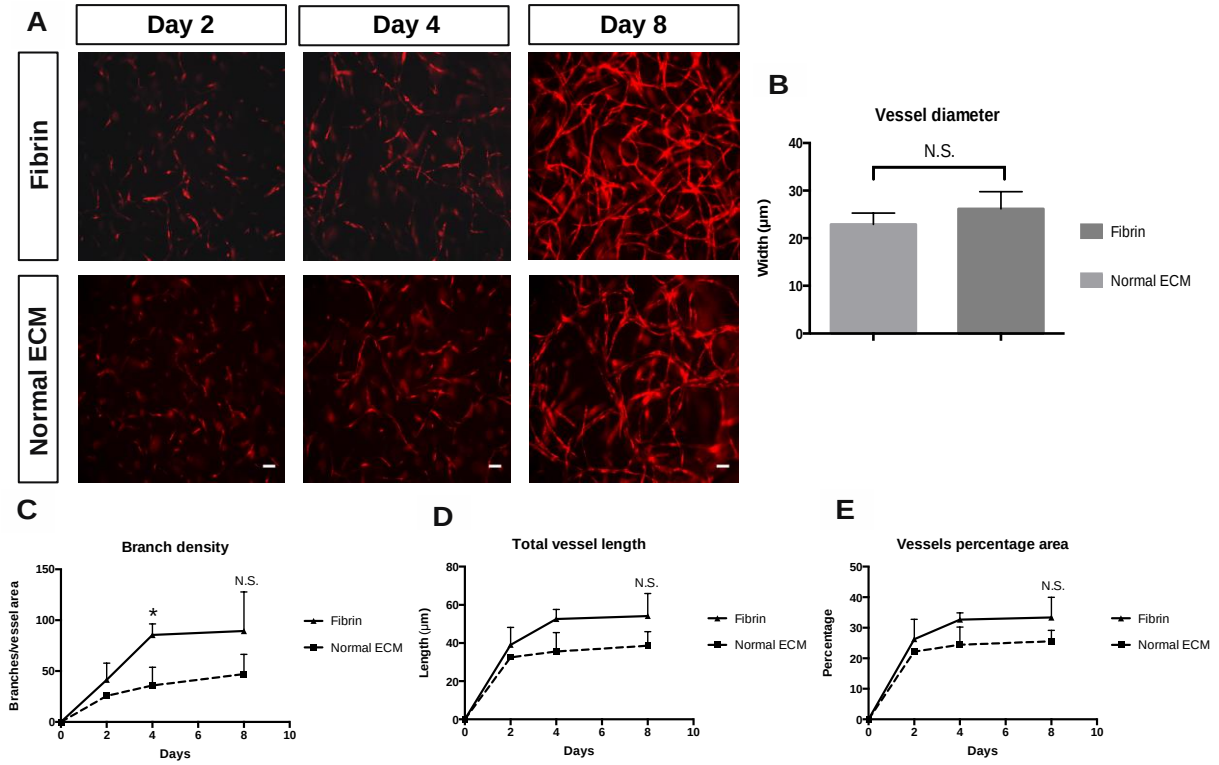


Figure 2.3. Vasculogenesis assay in Fibrin and Normal ECM (nECM). Coculture of 1 million/ml of fibroblasts and 2 million/ml of EC (mcherry-transduced) in Fibrin and nECM (A) The capillary network developed over 8 days in Fibrin and nECM. (B) Vessel diameter at day 8 in Fibrin and the nECM. No significance differences were evident (N. S.). Branch density (C), total vessel length (D) and vessel percentage area (E) increased over time in both conditions. All quantified parameters were higher in Fibrin than in nECM, however there were no significance differences. Scale bar=100 µm.

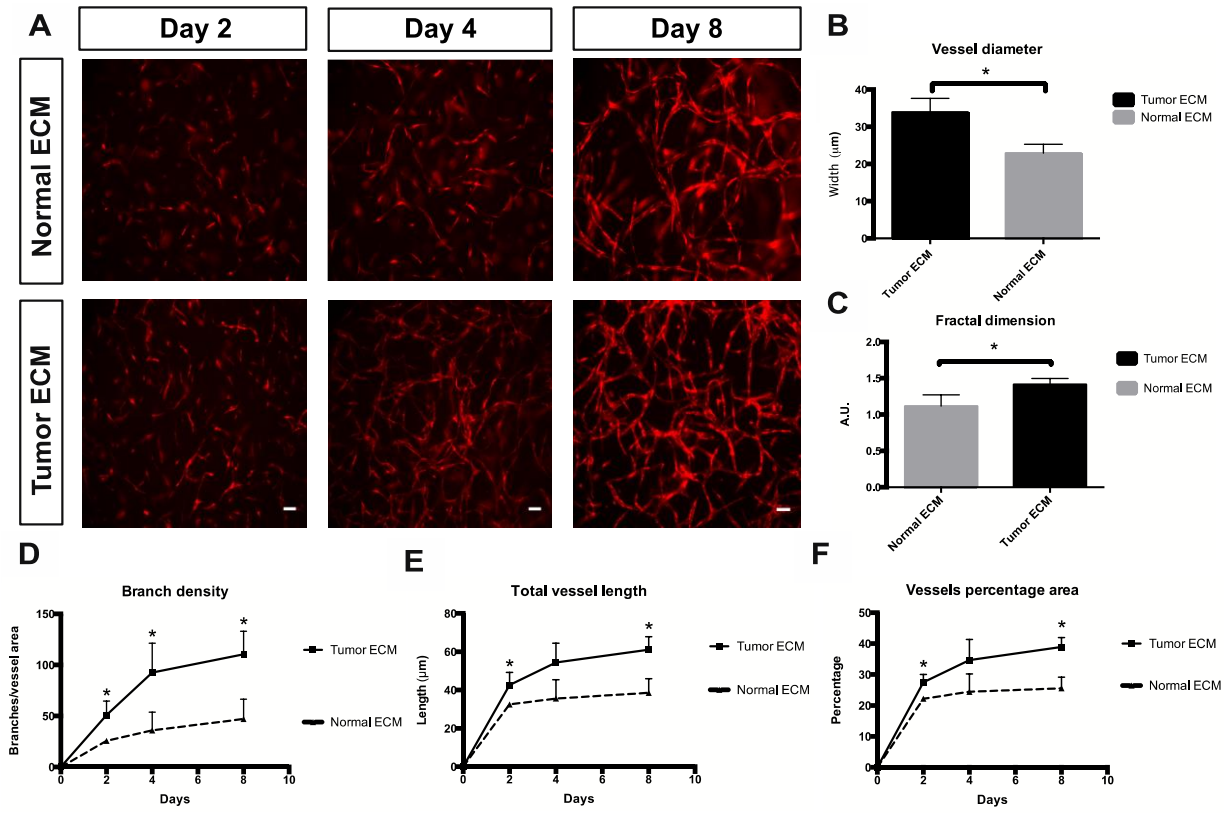


Figure 2.4. Vasculogenesis assay in Normal ECM (nECM) and Tumor ECM (tECM). Coculture of 1 million/ml of fibroblasts and 2 million of EC (mcherry-transduced) in nECM and tECM (A) The capillary network developed over 8 days in nECM and tECM. (B) Vessels that formed in the tECM displayed significantly larger diameters when compared to those that formed in the nECM ($p<0.05$). Additionally, vessels in the tECM were significantly more complex as indicated by increased fractal dimension (C) and increased branch density (D). Total vessel length (E) and vessel percentage area (F) were also significantly higher in tECM when compared to nECM ($p<0.05$). Scale bar=100 μm.

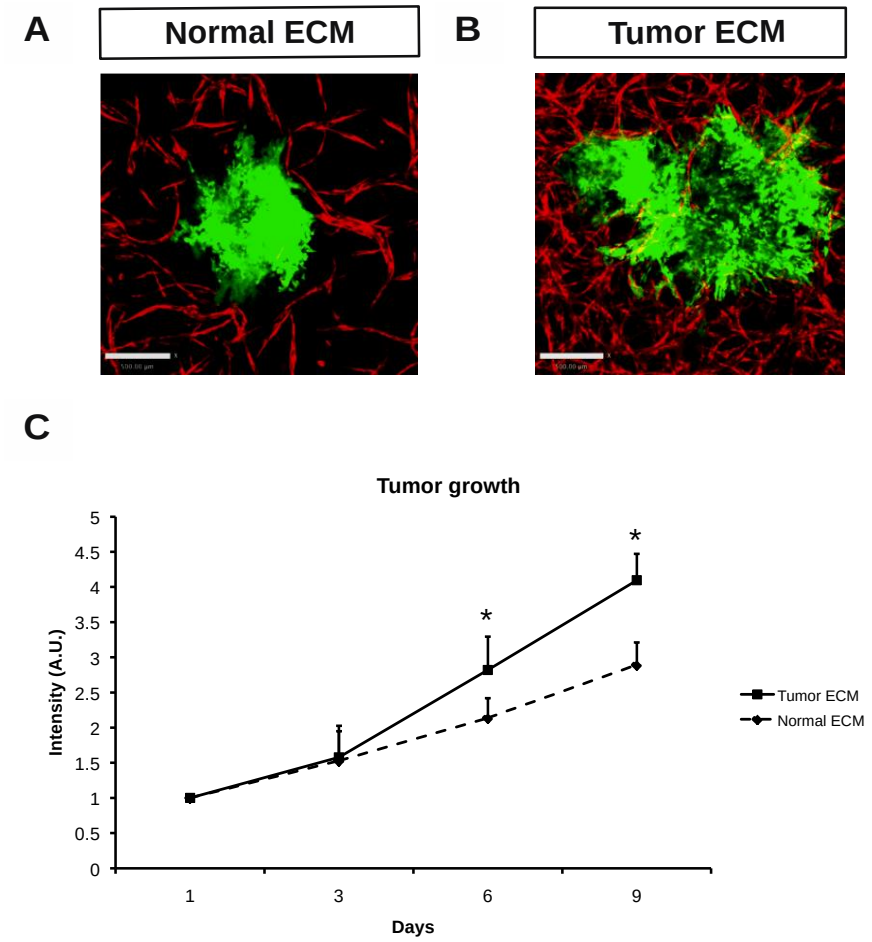


Figure 2.5. Tumor cell growth is increased in Tumor ECM (tECM). Tumor spheroid assay. (A, B) Coculture of 2 million/ml of fibroblasts and 2 million of EC (mcherry-transduced) with tumor colon cells (SW620, GFP-transduced) in nECM (A) and tECM at day 4 of the experiment (B). (C) SW620 cell growth was quantified, and tumors in tECM grew significantly more than in nECM. Scale bar= 500 μm

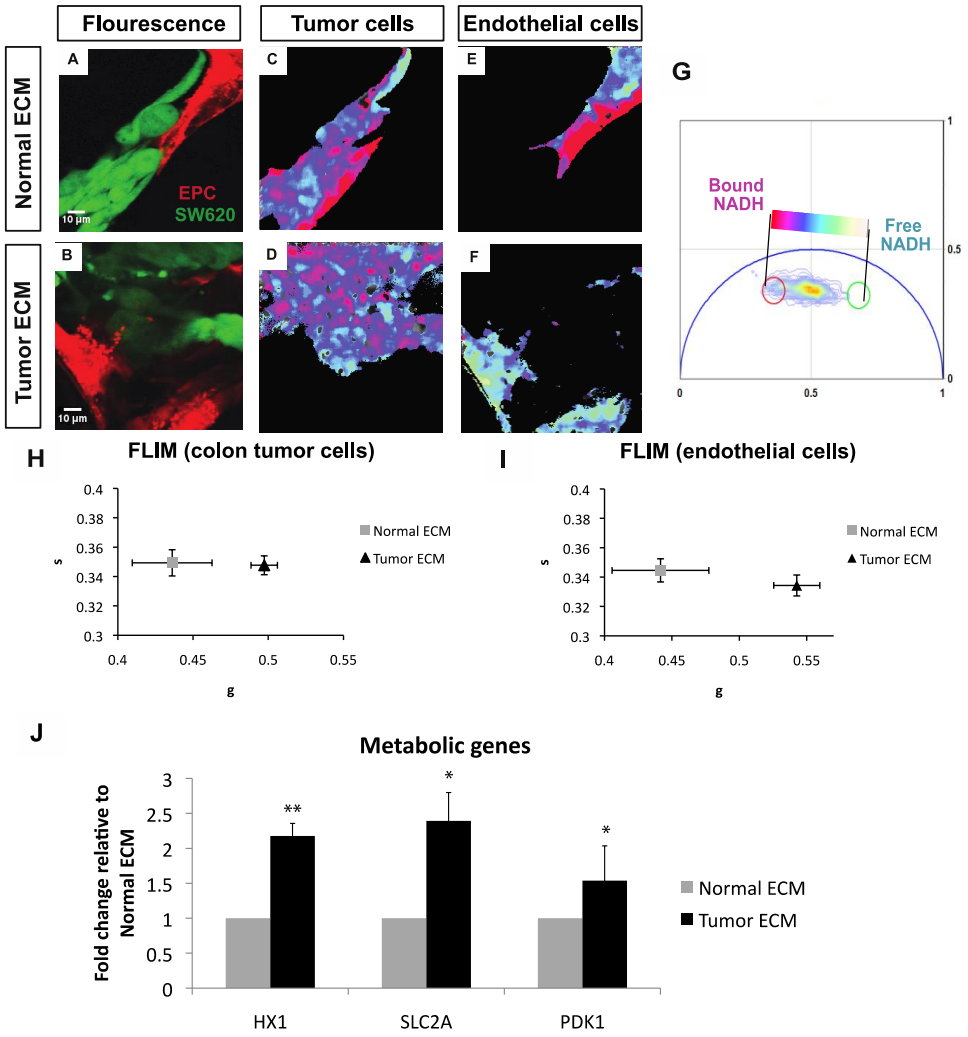


Figure 2.6. Fluorescence Lifetime Imaging Microscopy. Fluorescent images of EC (mcherry) and colon tumor cells SW620 (GFP) embedded in nECM (A) and tECM (B). NADH intensity of the tumor cells in nECM (C) and tECM (D). NADH intensity of the EC in nECM (E) and tECM (F). (G) NADH color map in the phasor plot. (H) FLIM phasor-plot values for SW620 cells seeded in nECM and tECM (I) FLIM phasor-plot values for EC seeded in nECM and tECM. (J) tECM induced the expression of genes involved in tumor metabolism. 1) HX1 (Hexokinase 1), 2) SLC2A (Solute Carrier Family/Facilitated Glucose Transporter Member 1), 3) PDK1 (Pyruvate Dehydrogenase Kinase). Student T-test *p<0.01 n = 4. Error bars are standard deviations of the mean. Scale bar = 10 µm

ECM protein	Normal ECM	Tumor ECM
Biglycan		
Collagen I		
Collagen III		
Collagen IV		
Collagen V		
Collagen VI		
Collagen XIV		
EGF-containing fibulin-like extracellular matrix protein		
Elastin		
Fibrilin		
Fibrinogen		
Fibronectin		
Fibulin		
Heparan Sulfate		
Laminin		
Latent-transforming growth factor beta-binding protein		
Periostin		
Peroxidasin		
Tenascin C		
Thrombospondin 2		
Vitronectin		

Table 2.1. Mass spectrometry data. Mass spectrometry was performed in Normal ECM and Tumor ECM. EGF-containing fibulin-like extracellular matrix protein (EFEMP1), Latent-transforming growth factor beta-binding protein (LTBP)

Source (3D Hydrogel)	**Storage Modulus (G') (Pa)**	**Loss Modulus (G'') (Pa)**
nECM	41 ± 29	8.9 ± 5
tECM	124 ± 54	31 ± 13

Table 2.2 The stiffness of nECM and tECM hydrogels. Microrheology was used to determine storage and loss modulus.

REFERENCES

4. Petersen, O.W., et al., *Interaction with basement membrane serves to rapidly distinguish growth and differentiation pattern of normal and malignant human breast epithelial cells.* Proceedings of the National Academy of Sciences of the United States of America, 1992. **89**(19): p. 9064-9068.
12. Annele, S., *Extracellular Matrix Macromolecules in Tumour Microenvironment with Special Reference to Desmoplastic Reaction and the Role of Matrix Proteoglycans and Hyaluronan.* Journal of Carcinogenesis & Mutagenesis, 2013. **S13**.
17. Tung, J.C., et al., *Tumor mechanics and metabolic dysfunction.* Free Radic Biol Med, 2015. **79**: p. 269-80.
18. Bissell, M.J. and D. Radisky, *Putting tumors in context.* Nature reviews. Cancer, 2001. **1**(1): p. 46-54.
19. Brownfield, Douglas G., et al., *Patterned Collagen Fibers Orient Branching Mammary Epithelium through Distinct Signaling Modules.* Current Biology, 2013. **23**(8): p. 703-709.
20. Kenny, P.A., et al., *The morphologies of breast cancer cell lines in three-dimensional assays correlate with their profiles of gene expression.* Mol Oncol, 2007. **1**(1): p. 84-96.
28. Bauer, A., T. Jackson, and Y. Jiang, *Topography of extracellular matrix mediates vascular morphogenesis and migration speeds in angiogenesis.* PLoS computational biology, 2009. **5**(7).
29. Amit, P. and K. Sanjay, *Transforming potential and matrix stiffness co-regulate confinement sensitivity of tumor cell migration.* Integrative Biology, 2013. **5**.
30. Zaman, M.H., et al., *Migration of tumor cells in 3D matrices is governed by matrix stiffness along with cell-matrix adhesion and proteolysis (vol 103, pg 10889, 2006).* Proceedings of the National Academy of Sciences of the United States of America, 2006. **103**(37): p. 13897-13897.
31. Zaman, M., *The role of engineering approaches in analysing cancer invasion and metastasis.* Nature reviews. Cancer, 2013. **13**(8): p. 596-603.
37. Badylak, S., D. Freytes, and T. Gilbert, *Extracellular matrix as a biological scaffold material: Structure and function.* Acta biomaterialia, 2009. **5**(1): p. 1-13.
42. Du, L., et al., *Histological evaluation and biomechanical characterisation of an acellular porcine cornea scaffold.* The British journal of ophthalmology, 2011. **95**(3): p. 410-414.
43. Hung, S.-H., et al., *Larynx decellularization: combining freeze-drying and sonication as an effective method.* Journal of voice : official journal of the Voice Foundation, 2013. **27**(3): p. 289-294.
44. Nichols, J., et al., *Production and assessment of decellularized pig and human lung scaffolds.* Tissue engineering. Part A, 2013. **19**(17-18): p. 2045-2062.
45. Booth, A., et al., *Acellular normal and fibrotic human lung matrices as a culture system for in vitro investigation.* American journal of respiratory and critical care medicine, 2012. **186**(9): p. 866-876.
46. Kajbafzadeh, A.-M., et al., *Determining the optimal decellularization and sterilization protocol for preparing a tissue scaffold of a human-sized liver tissue.* Tissue engineering. Part C, Methods, 2013. **19**(8): p. 642-651.

47. Mirmalek-Sani, S.-H., et al., *Immunogenicity of decellularized porcine liver for bioengineered hepatic tissue.* The American journal of pathology, 2013. **183**(2): p. 558-565.
48. Ott, H., et al., *Perfusion-decellularized matrix: using nature's platform to engineer a bioartificial heart.* Nature medicine, 2008. **14**(2): p. 213-221.
55. Johnson, T., S. Lin, and K. Christman, *Tailoring material properties of a nanofibrous extracellular matrix derived hydrogel.* Nanotechnology, 2011.
56. Freytes, D., et al., *Preparation and rheological characterization of a gel form of the porcine urinary bladder matrix.* Biomaterials, 2008. **29**(11): p. 1630-1637.
57. Sellaro, T., et al., *Maintenance of human hepatocyte function in vitro by liver-derived extracellular matrix gels.* Tissue engineering. Part A, 2010. **16**(3): p. 1075-1082.
58. Duan, Y., et al., *Hybrid gel composed of native heart matrix and collagen induces cardiac differentiation of human embryonic stem cells without supplemental growth factors.* Journal of cardiovascular translational research, 2011. **4**(5): p. 605-615.
59. DeQuach, J.e.a., *Simple and high yielding method for preparing tissue specific extracellular matrix coatings for cell culture.* PloS one 2009. **5**: p. e13039.
60. Pengfei Lu, V.M.W.a.Z.W., *The extracellular matrix: A dynamic niche in cancer progression.* J. Cell Biology, 2012. **196**(4): p. 395-406.
61. Coulson-Thomas, V.J., et al., *Colorectal cancer desmoplastic reaction up-regulates collagen synthesis and restricts cancer cell invasion.* Cell Tissue Res, 2011. **346**(2): p. 223-36.
62. Thomas Armstrong, G.P., Lindsay B. Murphy, Adrian C. Bateman, John A. Conti, David R. Fine, Colin D. Johnson, R. Christopher Benyon, and John P. Iredale, *Type I Collagen Promotes the Malignant Phenotype of Pancreatic Ductal Adenocarcinoma.* Clinical Cancer Research 2004. **10**: p. 7427–7437.
63. Hanna Nystrom, P.N., Anette Berglund, Richard Palmqvist, Bjorn Tavelin and Malin Sund, *Liver-metastatic Potential of Colorectal Cancer Is Related to the Stromal Composition of the Tumour.* Anticancer Research, 2012. **32**: p. 5183-5192.
64. Goetz, Jacky G., et al., *Biomechanical Remodeling of the Microenvironment by Stromal Caveolin-1 Favors Tumor Invasion and Metastasis.* Cell, 2011. **146**(1): p. 148-163.
65. Alcaraz, J., et al., *Laminin and biomimetic extracellular elasticity enhance functional differentiation in mammary epithelia.* The EMBO Journal, 2008. **27**(21): p. 2829-2838.
66. White, S.M., S.C. George, and B. Choi, *Automated computation of functional vascular density using laser speckle imaging in a rodent window chamber model.* Microvasc Res, 2011. **82**(1): p. 92-5.
67. Francis, M.E., S. Uriel, and E.M. Brey, *Endothelial cell-matrix interactions in neovascularization.* Tissue Eng Part B Rev, 2008. **14**(1): p. 19-32.
68. Edgar, L.T., et al., *Extracellular Matrix Density Regulates the Rate of Neovessel Growth and Branching in Sprouting Angiogenesis.* PLoS ONE, 2014. **9**(1): p. e85178.
69. Ghajar, C.M., Chen, X., Harris, J. W., Suresh, V., Hughes, C. C., Jeon, N. L., Putnam, A. J., George, S. C., *The effect of matrix density on the regulation of 3-D capillary morphogenesis.* Biophys J, 2008. **94**(5): p. 1930-41.
70. Baker, E.L., R.T. Bonnecaze, and M.H. Zaman, *Extracellular matrix stiffness and architecture govern intracellular rheology in cancer.* Biophys J, 2009. **97**(4): p. 1013-21.

71. Pickl, M. and C.H. Ries, *Comparison of 3D and 2D tumor models reveals enhanced HER2 activation in 3D associated with an increased response to trastuzumab.* Oncogene, 2008. **28**(3): p. 461-468.
72. Burns, J.S., et al., *Decellularized matrix from tumorigenic human mesenchymal stem cells promotes neovascularization with galectin-1 dependent endothelial interaction.* PLoS One, 2011. **6**(7): p. e21888.
73. Tammy T. Chang, M.D., Ph.D. and Millie Hughes-Fulford, Ph.D., *Monolayer and Spheroid Culture of Human Liver Hepatocellular Carcinoma Cell Line Cells Demonstrate Distinct Global Gene Expression Patterns and Functional Phenotypes.* Tissue Engineering: Part A, 2009. **15**(3): p. 559-67.
74. Yip, D. and C.H. Cho, *A multicellular 3D heterospheroid model of liver tumor and stromal cells in collagen gel for anti-cancer drug testing.* Biochem Biophys Res Commun, 2013. **433**(3): p. 327-32.
75. Fischbach, C., et al., *Engineering tumors with 3D scaffolds.* Nat Methods, 2007. **4**(10): p. 855-60.
76. Fischbach, C., et al., *Cancer cell angiogenic capability is regulated by 3D culture and integrin engagement.* Proceedings of the National Academy of Sciences of the United States of America, 2009. **106**(2): p. 399-404.
77. Longati, P., et al., *3D pancreatic carcinoma spheroids induce a matrix-rich, chemoresistant phenotype offering a better model for drug testing.* BMC Cancer, 2013. **13**: p. 95-95.
78. Nyga, A., et al., *A novel tissue engineered three-dimensional in vitro colorectal cancer model.* Acta biomaterialia, 2013. **9**(8): p. 7917-7926.
79. Jayme, L.H., et al., *3-D Tumor Model for In Vitro Evaluation of Anticancer Drugs.* Molecular Pharmaceutics, 2008. **5**.
80. Kibbey, M., *Maintenance of the EHS sarcoma and matrigel preparation.* Methods in Cell Science, 1994.
81. Hughes, C., L. Postovit, and G. Lajoie, *Matrigel: a complex protein mixture required for optimal growth of cell culture.* Proteomics, 2010. **10**(9): p. 1886-1890.
82. Serebriiskii, I., et al., *Fibroblast-derived 3D matrix differentially regulates the growth and drug-responsiveness of human cancer cells.* Matrix Biol, 2008. **27**(6): p. 573-85.
83. Almany, L. and D. Seliktar, *Biosynthetic hydrogel scaffolds made from fibrinogen and polyethylene glycol for 3D cell cultures.* Biomaterials, 2005. **26**(15): p. 2467-2477.
84. Callahan, L., et al., *ECM production of primary human and bovine chondrocytes in hybrid PEG hydrogels containing type I collagen and hyaluronic acid.* Biomacromolecules, 2012. **13**(5): p. 1625-1631.
85. Stahl, P., et al., *PEG-based hydrogels with collagen mimetic peptide-mediated and tunable physical cross-links.* Biomacromolecules, 2010. **11**(9): p. 2336-2344.
86. Beacham, D.A.A., Michael D; Cukierman, Edna, *Preparation of extracellular matrices produced by cultured and primary fibroblasts.*, in *Current Protocols in Cell Biology*. 2007.
87. Ahlfors, J.-E.W.B., K. , *Biomechanical and biochemical characteristics of a human fibroblast-produced and remodeled matrix.* . Biomaterials 2007. **28**: p. 2183–91.
88. Keane, T., et al., *Preparation and characterization of a biologic scaffold from esophageal mucosa.* Biomaterials, 2013. **34**(28): p. 6729-6737.

89. Petersen, T., et al., *Matrix composition and mechanics of decellularized lung scaffolds.* Cells, tissues, organs, 2012. **195**(3): p. 222-231.
90. Melero-Martin JM, K.Z., Picard A, Wu X, Paruchuri S, and Bischoff J. , *In vivo vaculogenic potential of human blood derived endothelial progenitor cells.* Blood, 2007. **109**: p. 4761-4768.
91. Ehsan, S.M., et al., *A three-dimensional in vitro model of tumor cell intravasation.* Integr Biol (Camb), 2014. **6**(6): p. 603-10.
92. Crosignani, V., et al., *Deep tissue fluorescence imaging and in vivo biological applications.* Journal of Biomedical Optics, 2012. **17**(11): p. 116023.
93. Maxwell A. Kotlarchyk, S.G.S., Martha B. Alvarez-Elizondo, Laura C. Estrada, Rahul Singh, Lorenzo Valdevit, Ekaterina Kniazeva, Enrico Gratton, Andrew J. Putnam, Elliot L. Botvinick., *Concentration Independent Modulation of Local Micromechanics in a Fibrin Gel.* PloS one, 2011. **6**(5): p. e20201.
94. Wisniewski, J.R., et al., *Universal sample preparation method for proteome analysis.* Nature methods, 2009. **6**(5): p. 359-62.
95. Seaman, M.E., S.M. Peirce, and K. Kelly, *Rapid analysis of vessel elements (RAVE): a tool for studying physiologic, pathologic and tumor angiogenesis.* PLoS One, 2011. **6**(6): p. e20807.
96. Digman, M.A., et al., *The Phasor Approach to Fluorescence Lifetime Imaging Analysis.* Biophysical Journal, 2008. **94**(2): p. L14-L16.
97. Stringari, C., Nourse, Jamison L., Flanagan, Lisa A., Gratton, Enrico, *Phasor Fluorescence Lifetime Microscopy of Free and Protein-Bound NADH Reveals Neural Stem Cell Differentiation Potential.* PLoS ONE, 2012. **7**(11): p. e48014.
98. Ziegler, M.E., et al., *mTORC2 mediates CXCL12-induced angiogenesis.* Angiogenesis, 2016: p. 1-13.
99. Naba, A., et al., *Extracellular matrix signatures of human primary metastatic colon cancers and their metastases to liver.* BMC Cancer, 2014. **14**(1): p. 1-12.
100. Mizuno, K., et al., *Narrow-banding images and structures of microvessels of colonic lesions.* Dig Dis Sci, 2011. **56**(6): p. 1811-7.
101. Pate, K.T., et al., *Wnt signaling directs a metabolic program of glycolysis and angiogenesis in colon cancer.* EMBO J, 2014. **33**(13): p. 1454-73.
102. Warburg, O., *On the Origin of Cancer Cells.* Science, 1956. **123**(3191): p. 309-314.
103. Badylak, S.F., Demeter, R. J., Hiles, M., Voytik, S. & Knapp Jr, P. M. , *Fluidized intestinal submucosa and its use as an injectable tissue graft.* United States Patent, 1994.
104. Weigelt, B., C.M. Ghajar, and M.J. Bissell, *The need for complex 3D culture models to unravel novel pathways and identify accurate biomarkers in breast cancer.* Advanced Drug Delivery Reviews, 2014. **69–70**: p. 42-51.
105. Egeblad, M., M.G. Rasch, and V.M. Weaver, *Dynamic interplay between the collagen scaffold and tumor evolution.* Current opinion in cell biology, 2010. **22**(5): p. 697-706.
106. Van Obberghen-Schilling, E., et al., *Fibronectin and tenascin-C: accomplices in vascular morphogenesis during development and tumor growth.* Int J Dev Biol, 2011. **55**(4-5): p. 511-25.
107. Orend, G. and R. Chiquet-Ehrismann, *Tenascin-C induced signaling in cancer.* Cancer Lett, 2006. **244**(2): p. 143-63.

108. Michaylira, C.Z., et al., *Periostin, a cell adhesion molecule, facilitates invasion in the tumor microenvironment and annotates a novel tumor-invasive signature in esophageal cancer.* Cancer Res, 2010. **70**(13): p. 5281-92.
109. Lopez, J.I., et al., *In situ force mapping of mammary gland transformation.* Integrative Biology, 2011. **3**(9): p. 910-921.
110. Plodinec, M., M. Loparic, and C.A. Monnier, *The nanomechanical signature of breast cancer.* Nature Nanotechnology, 2012. **7**(11): p. 757-65.
111. Rao, R.R., et al., *Matrix composition regulates three-dimensional network formation by endothelial cells and mesenchymal stem cells in collagen/fibrin materials.* Angiogenesis, 2012. **15**(2): p. 253-64.
112. Rowe, S.L. and J.P. Stegemann, *Microstructure and mechanics of collagen-fibrin matrices polymerized using ancrod snake venom enzyme.* J Biomech Eng, 2009. **131**(6): p. 061012.
113. Davis, G.E., et al., *Matrix metalloproteinase-1 and -9 activation by plasmin regulates a novel endothelial cell-mediated mechanism of collagen gel contraction and capillary tube regression in three-dimensional collagen matrices.* Journal of Cell Science, 2001. **114**(5): p. 917-930.
114. Ponce, M.L., *Tube Formation: an In Vitro Matrigel Angiogenesis Assay*, in *Angiogenesis Protocols: Second Edition*, C. Murray and S. Martin, Editors. 2009, Humana Press: Totowa, NJ. p. 183-188.
115. Koh, W., et al., *Chapter 5 In Vitro Three Dimensional Collagen Matrix Models of Endothelial Lumen Formation During Vasculogenesis and Angiogenesis*, in *Methods in Enzymology*. 2008, Academic Press. p. 83-101.
116. Bauer, A.L., T.L. Jackson, and Y. Jiang, *Topography of Extracellular Matrix Mediates Vascular Morphogenesis and Migration Speeds in Angiogenesis.* PLoS Comput Biol, 2009. **5**(7): p. e1000445.
117. Alves, T.R., et al., *Tenascin-C in the extracellular matrix promotes the selection of highly proliferative and tubulogenesis-defective endothelial cells.* Experimental Cell Research, 2011. **317**(15): p. 2073-2085.
118. Irvine, S.M., et al., *Quantification of in vitro and in vivo angiogenesis stimulated by ovine forestomach matrix biomaterial.* Biomaterials, 2011. **32**(27): p. 6351-6361.
119. Vorotnikova, E., et al., *Extracellular matrix-derived products modulate endothelial and progenitor cell migration and proliferation in vitro and stimulate regenerative healing in vivo.* Matrix Biol, 2010. **29**(8): p. 690-700.
120. Baker, A.M., et al., *Lysyl oxidase enzymatic function increases stiffness to drive colorectal cancer progression through FAK.* Oncogene, 2013. **32**(14): p. 1863-1868.
121. Zhao, Y., E.B. Butler, and M. Tan, *Targeting cellular metabolism to improve cancer therapeutics.* Cell Death & Disease, 2013. **4**(3): p. e532.
122. Cairns, R.A., I.S. Harris, and T.W. Mak, *Regulation of cancer cell metabolism.* Nat Rev Cancer, 2011. **11**(2): p. 85-95.
123. Serebriiskii, I., et al., *Fibroblast-derived 3D matrix differentially regulates the growth and drug-responsiveness of human cancer cells.* Matrix Biology, 2008. **27**(6): p. 573-585.

CHAPTER 3. Multiscale Modeling of Glioblastoma Reveals that Partially Disrupting Vessel/Cancer Stem Cell Crosstalk Reduces Tumor Size without Increasing Invasiveness

H. Yan[4], M. Romero-López[2], H.B. Frieboes [5,6,7], C.C.W. Hughes [1,2,3], J.S. Lowengrub [2,4]

[1]Department of Molecular Biology and Biochemistry, School of Biological Sciences, [2]Department of Biomedical Engineering, The Henry Samueli School of Engineering, [3]The Edwards Lifesciences Center for Advanced Cardiovascular Technology, [4]Department of Mathematics, University of California Irvine, Irvine, CA 92697, [5]Department of Biomedical Engineering, [6]James Brown Cancer Center, [7]Department of Pharmacology and Toxicology, University of Louisville.

Abstract—

In glioblastoma, the crosstalk between vascular endothelial cells (VECs) and glioma stem cells (GSCs) has been shown to enhance tumor growth. We propose a multiscale mathematical model to study this mechanism, explore tumor growth under different initial and microenvironmental conditions and investigate the effects of blocking the crosstalk. *Methods:* We develop a hybrid continuum-discrete model of tumor progression and vasculature growth. VEC-GSC crosstalk is modeled via VEGF production by tumor cells and by secretion of soluble factors by VECs that promotes GSC self-renewal and proliferation. *Results:* VEC-GSC crosstalk increases both tumor size and GSC fraction by enhancing GSC activity and neovascular development. VEGF promotes vessel formation and larger VEGF sources typically increase vessel numbers, which enhances tumor growth and stabilizes the tumor shape. Increasing the initial GSC fraction has a similar effect. Partially disrupting the crosstalk by blocking VEC secretion of GSC promoters reduces tumor sizes but does not increase invasiveness. This is in contrast to anti-angiogenic therapies, which also reduce tumor size but significantly increase

tumor invasiveness. *Significance:* We propose that targeting VEC-GSC crosstalk is a promising new approach for cancer therapies.

Introduction

Glioblastoma (grade IV glioma, GBM) is one of the most aggressive, heterogeneous, vascularized and deadly brain tumors and causes more than ten thousand deaths each year in the United States. The median patient survival for GBM is approximately 15 months, according to the American Brain Tumor Association. It remains a challenge to eradicate GBM because it is highly vascularized, heterogeneous, and invasive.

In recent years, the heterogeneity of the GBM has been extensively studied [124]. The glioma stem cell (GSC) hierarchy has been found to play a crucial role in tumor development and therapy resistance [125]. For example, tumors with high GSC population are more aggressive than tumors with low or no GSCs [126]. Further, as noted in [126], GSCs have three main characteristics. They are multipotent (differentiate into the other cell types), are able to self-renew (give rise to cells with the same characteristics) and produce tumors when implanted in animal models. It is also believed that GSCs are responsible for the resistance to radiotherapy and chemotherapy [127]. However, there are few experimental studies that identify different tumor cell lineages in GBM progression. Therefore, we develop and investigate a mathematical model to provide a better understanding of GSC dynamics in tumor progression.

In healthy brains, it has been observed that the microenvironment of neural stem cells (NSCs) is important in maintaining their stemness. In particular, vascular endothelial cells (VECs) secrete factors that stimulate the self-renewal and proliferation of NSCs, and NSCs are

found close to capillaries [128]. This crosstalk between the NSC niche and capillaries motivated similar studies in glioma. For example, [129] found that Nestin+/CD133+ cells, which are believed to be GSCs, are located closer to the capillaries, and GSCs cultured with VECs exhibit increased proliferation and self-renewal. In addition, GSCs respond to signals present in the secretome of VECs, indicating that GSCs do not require direct contact with VECs.

Several molecules are believed to control the crosstalk. These include endothelial Nitric Oxide that activates Notch signaling between adjacent VECs and GSCs and regulates the proliferation of the GSCs [130-132]. Also implicated is the Hedgehog (HH) pathway, which is involved in maintaining the stemness of somatic cells [133]. Sonic hedgehog ligand (Shh) is secreted by VECs and activates the HH pathway in GSCs, which regulates their self-renewal and proliferation [134]. The mTOR pathway has also been shown to maintain GSCs in the presence of VECs [135]. These pathways can be blocked as possible anti-tumor therapies.

A number of mathematical models have been developed to study tumor growth and its response to treatment [136]. For example, [137] reviewed theories of tumor vasculature and simulated random vessel network generation algorithms, tumor-vasculature interaction via growth factors and oxygen, and interstitial fluid flows. In [138], a data-based model was used to validate the structural link between metastatic emission and primary tumor size. In [139], a hybrid cellular automation was developed to investigate the effects of metabolic heterogeneity on tumor progression. Diffusible cytotoxic treatments (e.g. chemotherapy) and antiangiogenic therapy may increase metabolic aggressiveness. The studies in [140] revealed that acute and fractionated

irradiation results in GSC enrichment, which contributes to accelerated repopulation after irradiation, and reprogramming of non-cancer stem cells back to a cancer stem cell state [141].

In this paper, we develop a 3D hybrid continuum-discrete model of GBM by accounting for cancer cell lineages (collections of progressively more differentiated cancer cells) and feedback among the different cell types, following the continuum model in [142]. We account for tumor-induced neovascularization, following the discrete model in [143], and incorporate crosstalk between GSCs and VECs via pro-angiogenic factors secreted by tumor cells and factors secreted by VECs that promote GSC self-renewal and proliferation. We consider the effects of different VEGF sources on tumor progression and neovascularization. Since GSCs play an important role in tumor progression, we vary the initial GSC fraction and study tumor response. Then, we investigate the effects when the crosstalk is partially disrupted and when angiogenesis is blocked. Lastly, we relate our results to experimental findings and discuss future work.

Methods

Continuum tumor growth model

We adapt the three-dimensional multispecies tumor mixture model described in [142, 144], where tumor cells are tightly packed and cell species are modeled as volume fractions. Let φ_{GSC}, φ_{GCP}, φ_{GTD}, φ_D and φ_H be the volume fractions of GSCs, committed progenitor GBM cells (GCPs), terminally differentiated GBM cells (GTDs), dead GBM cells and host tissue respectively. The total fraction of tumor cells is $\varphi_T = \varphi_{GSC} + \varphi_{GCP} + \varphi_{GTD} + \varphi_D$. We assume that the fractions of solid region $\varphi_S = \varphi_T + \varphi_H$ and interstitial water (φ_W) are constant and add up to 1.

The volume fractions satisfy the mass conservation equation

$$\frac{\partial \varphi_i}{\partial t} = -\nabla \cdot \mathbf{J}_i + Src_i - \nabla \cdot (\mathbf{u}\varphi_i), \qquad (1)$$

where $i = GSC, GCP, GTD, D$ or T. $\mathbf{J}_i$ is a flux taken to penalize the mixing of the tumor and host tissues. The term $\nabla\cdot(\mathbf{u}\varphi_i)$ models passive cell movement (advection); $\mathbf{u}$ is the mass-averaged velocity of solid components defined by Darcy's law: $\mathbf{u} = -\nabla p + \mathbf{F}$, where $\mathbf{F}$ models cell adhesion and p is the solid pressure created by tumor cell proliferation. See Sec. S1 in Supplemental Materials for further details.

Tumor cell species and lineage relationships

Following [142], we assume that the proliferation rates of GSCs and GCPs are proportional to the nutrient concentration n. GSCs and GCPs self-renew with probabilities p_0 and p_1 respectively. GTDs do not proliferate and undergo apoptosis. The source term of dead cells consists of apoptosis and cell lysis into water. The mass exchange terms for tumor cells are

$$\begin{aligned} Src_{GSC} &= \lambda_m^{GSC} n\varphi_{GSC}(2p_0 - 1) \\ Src_{GCP} &= \lambda_m^{GSC} n\varphi_{GSC} 2(1-p_0) + \lambda_m^{GCP} n\varphi_{GCP}(2p_1 - 1) \\ Src_{GTD} &= \lambda_m^{GCP} n\varphi_{GCP} 2(1-p_1) - \lambda_a^{GTD}\varphi_{GTD} \\ Src_D &= \lambda_a^{GTD}\varphi_{GTD} - \lambda_L^D\varphi_D. \end{aligned} \qquad (2)$$

Here λ_m^{GSC} and λ_m^{GCP} are the mitosis rates of GSCs and GCPs respectively. λ_a^{GTD} is the apoptosis rate of GTDs, and λ_L^D is the lysis rate of dead cells. The mass exchange term of total tumor is the sum of Eq. (2) and accounts for GSC and GCP proliferation as well as cell lysis:

$$Src_T = \lambda_m^{GSC} n j_{GSC} + \lambda_m^{GCP} n j_{GCP} - \lambda_L^D j_D. \qquad (3)$$

Angiogenesis

We adapt the angiogenesis model in [143]. This model generates a vascular network stimulated by soluble angiogenic regulators (e.g. vascular endothelial growth factor, VEGF [1]), which we model using a single variable C_V, which represents the total concentration of pro-angiogenic factors (henceforth referred to as VEGF). In particular,

$$0 = \nabla\cdot(D_V \nabla C_V) - d_V C_V + S_V, \qquad (4)$$

where D_V, d_V and s_V are the diffusivity, natural decay and production rates of VEGF respectively. For example, VEGF may be produced by viable cells (whose volume fraction is $f_V = f_{GSC} + f_{GCP} + f_{GTD} = f_T - f_D$) in regions of hypoxia. This can be modeled as $S_V = p_V H(\tilde{n} - n)(f_T - f_D)$, where p_V is production rate, $H(x)$ is the Heaviside function ($H(x) = 1$ when $x > 0$; $H(x) = 0$ otherwise), and $\tilde{n}$ is the hypoxia threshold so that viable cells $(\phi_T - \phi_D)$ produce VEGF when the nutrient level $n < \tilde{n}$. Other sources of VEGF are considered in Sec. III. B.

Vessel sprout sites are selected at a constant probability once the VEGF concentration is higher than a threshold in a region a short distance away from the tumor. The tip cell moves in circular random walk and so the vessel network is independent of the computational grid for tumor cells. At each time step, the tip cell has a fixed probability to divide into two leading endothelial cells that continue to develop into new vessels. Once a tip cell crosses the path of another vessel, the two vessels may connect (anastomose) and form loops, and begin to deliver cell substrates, e.g. nutrients to the tumor. Such vessels are termed "functional." The contribution from all vessel segments that supply cell substrates is integrated to obtain the effective vascular density. See [143] for details.

Cell Substrates and Feedback Regulation

We assume that the nutrient concentration n satisfies a quasi-steady state equation, because nutrient diffusion (minutes) occurs significantly faster than cell proliferation (days). Nutrients are produced by pre-existing vessels in the host tissue and functional vessels. Cells uptake nutrients at potentially different rates. In particular,

$$0 = \nabla \cdot \left(D_n \nabla n\right) - \left(u_n^{GSC}\varphi_{GSC} + u_n^{GCP}\varphi_{GCP} + u_n^{GTD}\varphi_{GTD} + d_n\right)n + \left(p_n^H Q(\varphi_T) + p_n^V \rho_{FV}\right)(\bar{n} - n), \tag{5}$$

where D_n is the diffusivity, d_n is the natural decay rate, u_n^{GSC}, u_n^{GCP} and u_n^{GTD} are the uptake rates by GSCs, GCPs and GTDs respectively. The function $Q(\varphi_T) \approx 1-\varphi_T$ approximates the characteristic function of the host tissue, see [145]. p_n^V and p_n^H are the nutrient supply rates from the pre-existing and functional neo-vessels (ρ_{FV}) respectively. $\bar{n}$ is the nutrient concentration in the vessels. Further, when the solid pressure p exceeds a threshold at a specific location, nearby vessels are shut down (with a certain probability) by removing them from the vascular network and any associated vessel loops will discontinue nutrient delivery [143].

The self-renewal fraction of GSCs and GCPs are controlled by various soluble signaling factors. We assume that GTDs produce negative feedback regulators C_{T1} on GSC self-renewal and C_{T2} on GCP self-renewal. Frequently, these are members of the TGF-β superfamily, which are known to diffuse over long ranges (e.g., see [146] for Activin). In addition, we follow [142] and assume that there is a short range self-renewal promoter C_W (e.g. Wnt), and a long range inhibitor C_{WI} of C_W, e.g. Dkk [147, 148]. Both C_W and C_{WI} are produced by GSCs [149] and their production rates are proportional to the nutrient level. We use a generalized Gierer-Meinhardt model described in [142] for C_W and C_{WI}. See Sec. S2 in Supplemental Materials for details.

Crosstalk

In brain tumors, primary human endothelial cells (pHVECs) are found to help maintain the cancer stem cell pool through soluble factors, and increase the size of tumor spheres [129], suggesting positive feedback from pHVECs to stem cells. Here, we investigate the combined effect of possible mechanisms in [129, 134, 150] and assume that the vasculature produces a soluble cell substrate *F* whose concentration is C_F:

$$\frac{\partial C_F}{\partial t} + \nabla \cdot \left(\mathbf{u}_w C_F\right) = \nabla \cdot \left(D_F \nabla C_F\right) - d_F C_F + p_F^V \rho_V \left(\overline{C_F} - C_F\right), \quad (6)$$

where $\nabla \cdot (\mathbf{u}_w C_F)$ models the advection with the interstitial water, D_F and d_F are the diffusivities and natural decay respectively. p_F is the production rate from neovessels (ρ_V), $\overline{C_F}$ is the concentration near the vessels. The factor F is assumed to represent the concentration of all VEC secreted GSC promoters.

We assume that C_F promotes both GSC proliferation and self-renewal. We thus take the GSC mitosis rate to be

$$\lambda_m^{GSC} = \bar{\lambda}_m^{GSC}\left(1 + \Delta_m^F \frac{\chi_m^F}{1 + \chi_m^F}\right), \quad (7)$$

where $\bar{\lambda}_m^{GSC}$ is the base proliferation rate, χ_m^F is the positive feedback gain by C_F and Δ_m^F is the maximum fold change.

Next, we incorporate the positive feedback by C_F and C_W, and negative feedback by C_{T1} on the probability of GSC self-renewal. We take a multiplication of Hill functions

$$p_0 = p_0^{\min} + \left(p_0^{\max} - p_0^{\min}\right) \times \frac{c_0^F C_F + c_0^W C_W}{1 + c_0^F C_F + c_0^W C_W} \frac{1}{1 + \psi_0 C_{T1}}. \quad (8)$$

Here $p_0^{\min}$ and $p_0^{\max}$ are the minimum and maximum levels of GSC self-renewal respectively. χ_0^F and χ_0^W are the positive feedback gains by C_F and C_W respectively. ψ_0 is the negative feedback gain by C_{T1}. The self-renewal probability of GCPs is defined analogously without the feedback from C_F:

$$p_1 = p_1^{\min} + \left(p_1^{\max} - p_1^{\min}\right) \times \frac{c_1^W C_W}{1 + c_1^W C_W} \frac{1}{1 + \psi_1 C_{T2}}. \quad (9)$$

Results

We now solve the model to study tumor progression and its response to treatment. The tumor begins as a perturbed avascular spheroid that, unless stated otherwise, consists of uniformly distributed 10% GSCs, 25% GCPs, 60% GTDs and 5% dead cells. All parameters are listed in Table S1 in Supplementary Materials.

VEC-GSC crosstalk promotes stem cell proliferation

At early stages, GSCs self-organize and clusters emerge at tumor boundary (Fig. 1A, red; Fig. 1B) as an effect of a Turing-type pattern formation of the self-renewal promoter and its inhibitor, which was also observed in [142]. While the tumor grows, these GSC clusters stay near the tumor boundary, where nutrients and cell proliferation levels are higher. Blood vessels sprout (red dots) near the tumor boundary around T = 40, then grow and anastomose into functional vessels (blue lines) that are connected to host vasculature and supply nutrients to the tumor.

Consequently, tumor cell proliferation is enhanced and the tumor size grows rapidly. Interestingly, the evolution of the GCPs is non-monotone; the GCP fraction reaches a minimum around T=50 (Fig. 1A and Fig. S2, blue in Supplementary Materials). This occurs because around this time GSC self-renewal is enhanced by VEC-GSC crosstalk, p_0 at the center begins to increase over 0.5 due to positive feedback F secreted by VECs (Fig. 1C). This decreases the replenishment of the GCP population by differentiating GSCs and so GCP numbers decrease due to their differentiation to GTDs (recall that the maximum GCP self-renewal $p_1^{\max} = 0.45 < 0.5$). As a result, a new GSC cluster emerges at the tumor center and the GSC fraction in the tumor increases (Fig. 1B, Fig. 2B, blue). We note that high p_0 regions are colocalized with functional vessels, which are mainly present at the tumor center (Fig 1C).

VEGF sources affect tumor and vasculature characteristics

Next, we study the effects of different VEGF sources on the tumor and vasculature. To quantify the tumor shape, we use the shape factor: $\sqrt[3]{36\pi}\frac{S}{V^{2/3}}$, where S and V are the surface area and volume of the tumor respectively. Note that a sphere has shape factor equal to one. To quantify the vessel network, we use the tortuosity of the vessel network (following [151]), as well as the total number of vessels and the number of functional vessels. In Fig. 1, VEGF is produced by hypoxic tumor cells: $S_V = p_V H(\tilde{n} - n)(j_T - j_D)$ is used in Eq. (7), as described earlier.

The tumor volume grows rapidly once angiogenesis starts around T=37 (Fig. 2A, blue). The volume fraction of GSCs increases slightly after this (Fig. 2B, blue) due to enhanced GSC proliferation and self-renewal because of increased nutrients and positive feedback from VECs. After T=60, the fraction reaches a maximum and stabilizes. We will discuss this in the next section. The tumor remains roughly spherical with shape factor approximately equal to one (Fig. 2C, blue) although the growth of fingers at late times increases the shape factor. The total number of vessels steadily increases (Fig. 2F, blue), consistent with the fairly steady increase in VEGF production (Fig. 2G, blue). However, the number of functional vessels also reaches a maximum shortly after angiogenesis is initiated (Fig. 2E, blue) and before increasing at late times. The non-monotone dynamics of the number of functional vessels is due to the crushing of vessels by high pressure resulting from rapid cell division, which is consistent with experimental observations [152, 153]. Vessel crushing also causes the tortuosity of the vascular system to saturate (Fig. 2D, blue).

It has been believed that hypoxic tumor cells secrete angiogenic proteins that promote

tumor vascularization, as modeled above. However, [154] observed that tumors with higher initial populations of GSCs are more vascularized and aggressive. The authors found that under normoxic conditions, only GSCs secrete angiogenic factors, e.g. vascular endothelial growth factors (VEGF). However, non-GSCs also secrete VEGF under hypoxic conditions. In particular, GSCs secreted more than twice as much angiogenic factors than non-GSCs. In a migration and tube formation assay with endothelial cells using conditioned media from CD133+ (GSC) and CD133- (non-GSC) cells, they observed higher total vessel length with CD133+ conditioned media. Moreover, higher microvessel densities were observed in GSC orthotopic xenograft tumors in mice compared with non-GSC tumors, indicating that GSCs recruited higher number of VECs, which is correlated with the amount of VEGF secreted.

To model this mixed VEGF production, we take $S_V = p_V H(\tilde{n} - n)(f_T - f_D) + p_V(f_{SC} + f_{CP})$, where we assume that GCPs and GSCs behave similarly with respect to VEGF production. Compared to Fig. 1, the tumor with mixed S_V grows faster (Fig. 2A, red versus blue), has larger GSC fraction (Fig. 2B), is more compact (Fig. 2C), has more tortuous vessels (Fig. 2D), and more vessels generally (Figs. 2E and F) and generates larger amounts of VEGF (Fig. 2G). Accordingly, neovascularization starts earlier, around T=25, compared to T=37 for hypoxic production of VEGF. Interestingly, because nutrients are supplied into the tumor interior, the GSC clusters originally at the tumor boundary move inwards and merge with the central GSC cluster. As a result, finger development is suppressed and the tumor acquires a nearly spherical shape. In contrast, the tumor in Fig. 1 still has fingers at late stages that continue to develop.

Next, we take out hypoxic cells from the mixed VEGF production, so that VEGF is only produced by GSCs and GCPs ($S_V = \rho_V(j_{SC} + j_{CP})$). The amount of VEGF is reduced compared to the mixed case from the beginning (Fig. 2G, red vs green) since hypoxic GTDs at the center no longer produce VEGF. In the early stages of angiogenesis, however, more VEGF is produced than the tumor in Fig. 1, although this trend reverses at later times (Fig. 2G). Consequently, vessels are generated later in time than the mixed case but early than the hypoxic case considered in Fig. 1 (see Figs. 2E, F). Correspondingly, the GSC fraction is lower compared to the mixed case but is larger than that for the hypoxic case during the early stages of angiogenesis, before dropping below the hypoxic case at later times (Fig. 2B).

After the tumors are vascularized, they all grow roughly at the same speed (Fig. 2A). The vessels are less tortuous compared to both the mixed and hypoxic VEGF sources because most vessels are directed towards GSC clusters (see Fig. S1 in Supplemental Materials). This also results in less pressure-induced vessel crushing, as seen by the steady increase of functional vessels at later times (Fig. 2E, green). The shape factor is increased compared to the tumor with mixed S_V due to fingers on the tumor surface (Fig. 2A). The tumor is less invasive (smaller shape factor) than the hypoxic case (Fig. 2C).

Overall, we observe that the larger VEGF production results in vascularization of the tumor at an earlier time and that GSC fraction and the number of vessels at early times are correlated with the amount of VEGF. Later, as vessel crushing occurs, the evolution of vessel numbers is not monotone with VEGF amounts. However, tumor sizes correlate with the number of functional vessels. Finally, the tumor with mixed VEGF sources has most tortuous vessels

among the VEGF sources we tested, which is consistent with experimental results when VEGF is overexpressed [155].

Higher initial GSC fractions increase tumor sizes and vessel numbers

An *in vitro* and *in vivo* study in [156] showed the differences in GBM growth and vasculature between low and high numbers of GSCs. The authors observed larger tumors and higher perfused microvessel densities (functional vessels) with more initial GSCs. Consistent with [154], they also showed that tumors with more GSCs expressed significantly more VEGF both *in vitro* and *in vivo*, which is directly correlated with the number of vessels in the tumor.

We now take the tumor in Fig. 1 and change the initial GSC fraction to 30%, 50%, 70% and 90%. We take the extra portions first from GTDs, then from dead cells and finally from GCPs as necessary. For example, the tumor that starts with 50% GSCs has 25% GCPs, 20% GTDs (reduced) and 5% dead cells. The tumor with 90% GSCs has 10% GCPs and no GTDs/dead cells initially. Cell distributions are still homogeneous in space initially. We take $S_V = p_V H(\tilde{n} - n)(\varphi_T - \varphi_D)$ for all cases. The tumor morphologies and cell and vessel distributions are shown in Fig. 3A. While the initial sizes are the same, tumors starting from higher GSC fractions grow more rapidly. The center GSC cluster forms earlier, and connects to GSC clusters near the boundary as it grows. These GSC clusters no longer develop into fingers. Consequently, the tumors with large GSC initial fractions are more compact and the shape factor is smaller (Fig. 3D).

An interesting observation is that the GSC fraction in all cases converges to approximately 30% as time evolves, regardless of tumor size and initial GSC fraction (Fig. 3C).

This suggests that the GSC fractions are regulated by feedback from GTDs and VEC-GSC crosstalk, which in part is regulated by mechanical feedback. For instance, the number of functional vessels saturates at roughly similar values across all tumor cases. This is due to vessel crushing and reflects regulation by mechanical pressure. By changing the vascular model parameters, e.g., making the sprouting probability continuously dependent on VEGF concentration and varying the pressure threshold at which crushing occurs, the limiting GSC fractions can be altered (see Figs. S6-S7 in Supplemental Materials). See also the Supplementary Materials (Figs. S4 and S5) for the dynamics of the GCP and GTD fractions.

As for the vasculature, larger initial GSC fractions increase VEGF production (see Fig. S5 in Supplemental Materials) and advance vessel formation, except that the 90% and 70% cases are vascularized at the same day (Fig. 3E). Vessel crushing takes place in tumors with more than 30% initial GSCs, which stabilizes the number of functional vessels. The dynamics is similar in tumors with 70% or 90% initial GSCs, which suggests that the feedback from crosstalk has saturated.

Partially disrupting VEC-GSC crosstalk reduces tumor volume without significantly increasing invasiveness

In experiments, a number of mechanisms have been found to partially disrupt VEC-GSC crosstalk. For example, it was observed that the self-renewing GSC population and the tumor size are reduced when blocking the mTOR pathway [135]. In addition, blocking Hedgehog signaling also inhibits the self-renewal and proliferation of the GSCs, and produces smaller tumors [134]. To model this type of treatment, we take the tumor in Fig. 1 as the Control and test the effects of partially disrupting VEC-GSC crosstalk by blocking VEC secretion of the GSC promoter F. Recall that in Control, functional vessels release feedback factors F that enhance

GSC proliferation and self-renewal. As a result, the effective GSC mitosis rate $\lambda_m^{SC} n(2p_0 - 1)$ is higher and the tumor has a large GSC cluster at the tumor center (Fig. 4F, top row). However, when the VEC secretion of *F* is blocked (or *F* is de-activated), only the self-renewal promoter C_W exerts positive feedback on p_0. Since C_W colocalizes at GSC clusters, p_0 at other locations is greatly reduced (Fig. 4F, middle row). Thus, in the treated case, the large GSC cluster at tumor center no longer forms. Consequently, both the tumor volume and the GSC fraction are reduced significantly compared to Control (Figs. 4A, B; green vs blue). Importantly, the shape factor is not significantly increased from that for the Control (Fig. 4C), which suggests that this treatment does not increase tumor invasiveness. This can be explained as follows.

In Control, GSC proliferation at the center creates excessive solid pressure that induces vessel crushing (see Fig. S9 in Supplemental Materials). As a result, the number of functional vessels decreases between T=45 and T=60 (Fig. 4E, blue). Nutrient production also decreases, which stabilizes the average nutrient concentration in the tumor (Fig. 4D, blue), calculated as $\int_\Omega \varphi_T n dx / \int_\Omega \varphi_T dx$. In contrast, when the VEC secretion of *F* is blocked, the solid pressure is much lower, vessels rarely crush and the number of functional vessels increases steadily (Fig. 4E, green). This brings more nutrients to the tumor (Fig. 4D, green) enabling GSCs to proliferate faster and be located more in the tumor interior rather than at the tumor boundary, which is the case at early times. Consequently, at late times, finger growth is suppressed, the tumor becomes more compact and its shape factor approaches that of the Control. Note that the shape factor does increase between *T*=40 and *T*=60 during the early stages of angiogenesis before there is significant nutrient delivery through the neovasculature.

Next, we block angiogenesis in the model. Effectively, this removes the positive feedback on tumor cell proliferation from nutrients released by functional vessels. The tumor

volume is further reduced (Fig. 4A, red). Starting from T=40, GSC clusters near the boundary begin to develop fingers. Since few nutrients penetrate the tumor and the nutrient level is now highest at tumor boundary, the GSC clusters remain at the tumor boundary and promote the growth of invasive fingers, which are much more pronounced than the invasive tumors and significantly increase the shape factor (Fig. 4C, red). At late stages (T~100), these fingers grow into multifocal tumors, indicating greater tumor invasiveness. The GSC fraction is also higher than the tumor with partially disrupted VEC-GSC crosstalk because the tumor is smaller and GSCs are located at the tips of fingers where there is ample nutrient, which increases GSC proliferation and self-renewal. Further, in the tumor interior, the nutrient levels are low, which reduces cell proliferation (Fig. 4F, bottom row). Overall, our results are consistent with previous experiments where it has been observed that vessel densities, tumor sizes and GSCs are reduced following antiangiogenic therapy (bevacizumab) [129]. It is also well known that GBM becomes more invasive after bevacizumab treatment [157], and even forms multifocal tumors in some cases [158]. Previous mathematical models that did not distinguish between tumor cell types also have demonstrated such behavior [159].

Discussion

In this paper, we have developed and investigated a hybrid continuum-discrete multispecies model of GBM growth. We modeled feedback interactions among GSCs, GCPs, GTDs, VECs and the neovascular network. The cells and cell substrates are treated as continuum, and the vasculature is composed of discrete VECs. Nutrient delivery from the vasculature enhances tumor cell proliferation. VEC-GSC crosstalk is mediated by a VEC-secreted soluble factor that promotes GSC mitosis and self-renewal. Tumor cells may secrete VEGF and promote vessel formation, whereas excessive solid pressure created by tumor cell

proliferation causes vessels to be crushed, which limits perfusion. Although we presented the results corresponding to one set of parameters (Table S1, Supplementary Materials), the model behavior we observe is characteristic of that obtained across a wide range of parameters.

GSC spatiotemporal patterning plays an important role in tumor invasion. During the avascular stage of growth, our model predicts that GSCs cluster near the tumor boundary and develop into invasive fingers. Similar results have been observed previously in both experiments [160] [161] and modeling studies [142]. Our results suggest that blocking angiogenesis, via antiangiogenic therapy, effectively reduces tumor size, but risks increased tumor invasion. Avascular tumors invade aggressively by increasing their surface area to gain access to nutrients in the host [162]. Angiogenesis restrains tumor invasion through nutrient supplied from functional vessels, which results in more uniform cell proliferation and faster growth as a tradeoff. This is consistent with experimental results, e.g., see [163, 164].

Both angiogenesis and vessel growth are affected by VEGF production. It is typically assumed that hypoxic tumor cells release VEGF to promote vessel formation and gain access to nutrients. However, there is also evidence that GSCs and GCPs may be more involved in VEGF production [154]. When this is taken into account, our studies show that this results in larger amounts of VEGF in the system. Consequently, this advances the time when angiogenesis starts, results in more vessels in early stages, and promotes larger tumors. At later stages of growth, vessels may be crushed due to proliferation-induced pressure forces, which can lead to a non-monotone evolution of vessel distributions. We also find that, consistent with experiments [165, 166], vessels are more tortuous with increasing amounts of VEGF. It is thought that an excess of VEGF impairs vessel development giving rise to tortuous vessels [167].

Due to the importance of GSCs in tumor progression, their initial fraction is expected to affect tumor characteristics. We have shown that tumors with higher GSC fractions grow larger in size and have larger amounts of vessel3s, which has been observed experimentally in [156]. However, GSC fractions converge to a common value as time evolves regardless of the tumor size and initial GSC fraction. This unexpected result suggests that GSC fractions are regulated by a complex interplay of mechanical and chemical signaling mechanisms.

Finally, we have demonstrated that the VEC-GSC crosstalk enhances tumor growth and increases GSC fractions, which is also consistent with experiments (e.g., [129, 154]). In these tumors, positive feedback factors from VECs, combined with increased nutrient levels, result in the formation of GSC clusters in the tumor interior in addition to those at the boundary. This leads to more uniform cell proliferation within the tumor and as a result, the tumors tend to grow in compact shapes. We found that partially disrupting VEC-GSC crosstalk by blocking secretion of GSC promoters reduces tumor sizes very effectively and, unlike anti-angiogenic therapy, does not significantly increase the potential for invasiveness. This suggests that targeting VEC-GSC crosstalk is a promising direction for anti-cancer treatment.

Conclusion

We have developed and studied a 3D hybrid mathematical model of glioblastoma growth that accounts for cancer cell lineages containing cancer stem cells, committed progenitor cells and post-mitotic terminally differentiated cells, as well as vascular endothelial cells and a tumor-induced neovascular network. Feedback signaling between tumor cells and vasculature regulates their dynamics. Our studies show how the tumor and vascular development depend on feedback regulation. For instance, crosstalk between cancer stem cells and vascular endothelial cells, via

pro-angiogenic factors secreted by tumor cells and VEC-secreted factors that upregulate GSC proliferation and renewal, is shown to promote cancer stem cell self-renewal and proliferation, resulting in large tumors with tortuous neovascular networks. Targeting this crosstalk is shown to hold promise as a novel anti-cancer therapy.

Acknowledgment

The authors thank Arthur Lander, Hamed Youssefpour and Marian Waterman for useful discussions.

Figures

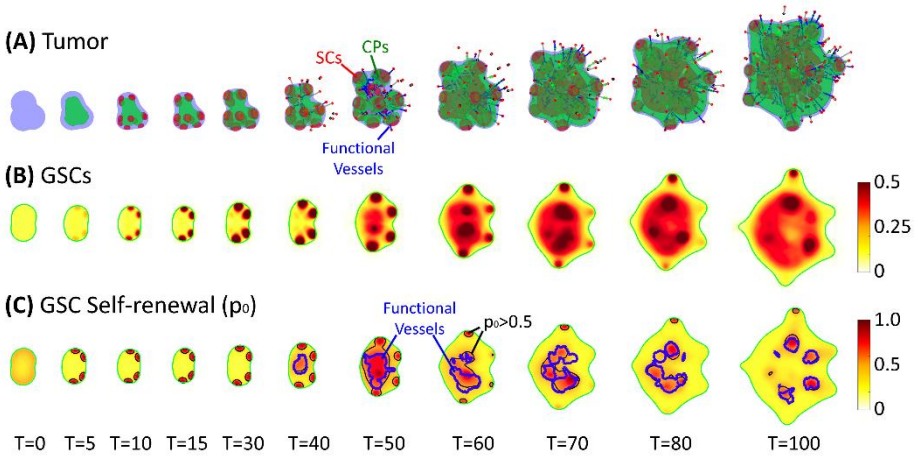


Figure 3.0-1 VEC-GSC crosstalk promotes GSC proliferation and self-renewal

Fig. 3.1. VEC-GSC crosstalk promotes GSC proliferation and self-renewal. **(A)** Time evolution of tumor ($\varphi_T = 0.5$ surface, blue), GSCs ($\varphi_{GSC} = 0.3$ surface, red), GCPs ($\varphi_{GCP} = 0.25$ surface, green) and neovasculature (red dots: sprout initiation points; grey: sprouts, blue: functional vessels). At early stages, GSC clusters form near the tumor boundary and fingers develop. Angiogenesis starts around T =39, after which a large GSC cluster forms at the center of tumor due to VEC-GSC crosstalk. **(B)** 2D slices of GSCs (at z =-1). At T=5, GSC clusters begin to emerge near tumor boundary. **(C)** 2D slices of the GSC self-renewal probability p_0 (at z=-1) shown together with the $p_0 = 0.5$ (black) and functional vessel density $\rho_{FV} = 20$ (blue) contours. In the tumor interior, the functional vessels are colocalized with GSC clusters with $p_0 > 0.5$.

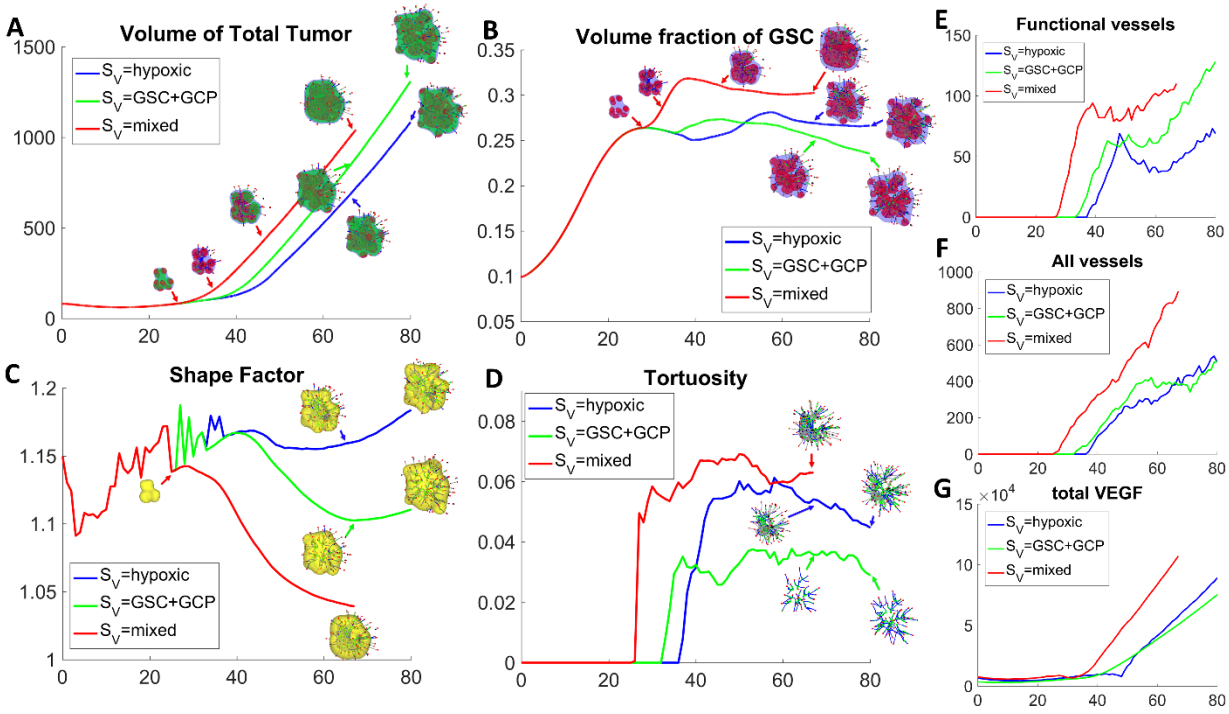


Figure 3.2 VEGF sources affect tumor and vasculature characteristics. (A) Time evolution of total tumor volumes; (**B)** GSC fractions; (**C**) shape factor; (**D**) vessel tortuosity; (**E**) numbers of functional vessels; (**F**) numbers of all vessels; and (G**)** total amount of VEGF with indicated VEGF sources. Insets in (**A-D**) show GSCs (red), GCPs (green), tumor shape (yellow) and the vessel network (red dots: sprout initiation points; grey: sprouts, blue: functional vessels) respectively. When GSC/GCPs produce twice as much VEGF as other cells (red curves), the tumor has largest amount of VEGF that yields largest tumor size, GSC fraction and most spherical tumor shape. As the source of VEGF is reduced (e.g. blue/green curves), vessels are generated later, the tumor is more invasive (larger shape factor) and vessels become less tortuous. At late stages, vessel crushing takes place in all tumors leading to non-monotone time evolution of the number of functional vessels and to saturation in vessel tortuosity.

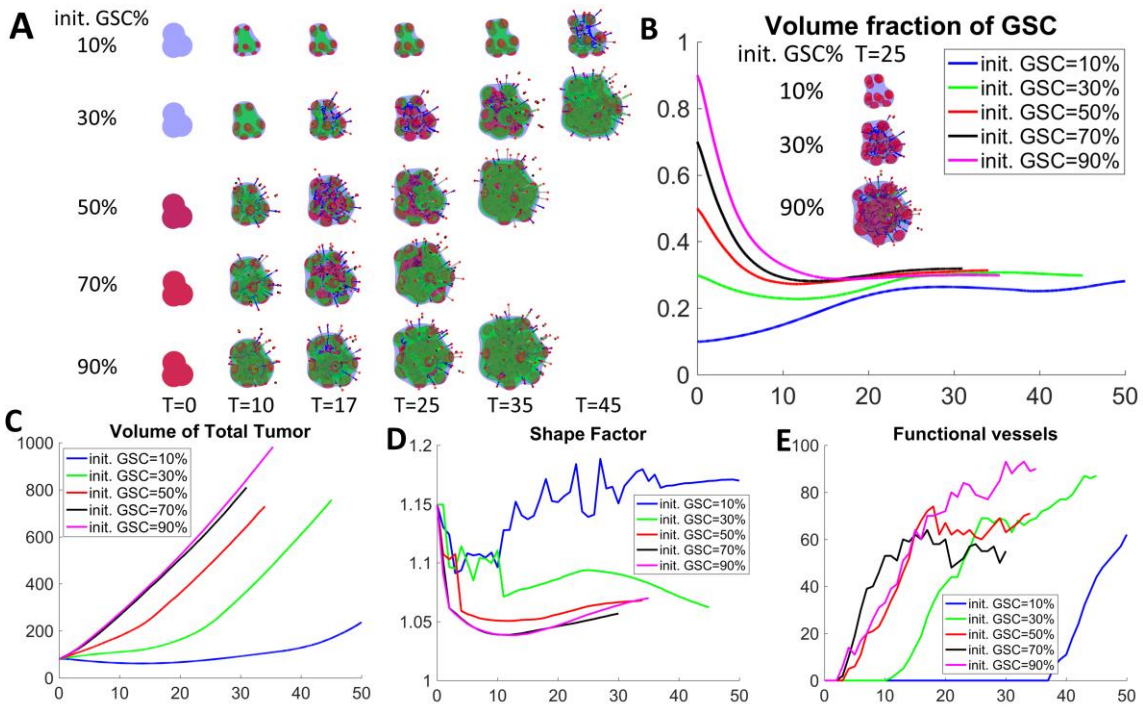


Figure 3.3. Higher initial GSC fractions increase tumor sizes and vessel numbers. **(A)** Evolution of tumors with different initial GSC fractions at indicated times. A large GSC cluster emerges earlier in tumors with higher initial GSC fraction. **(B)** As time evolves, the GSC fraction in all cases converges to approximately 30% despite different tumor sizes and initial GSC fractions. Insets show GSC distributions in tumors with 10%, 30% and 90% initial GSCs. **(C)** Higher initial GSC fractions result in larger tumor sizes. **(D)** Tumors with higher initial GSC fractions grow in more compact shapes. **(E)** The number of functional vessels. Angiogenesis begins earlier in tumors with higher initial GSC fraction. The 50%, 70% and 90% tumors generate functional vessels around the same time, and the functional vessel numbers evolve similarly, suggesting that the positive feedback from VEC-GSC crosstalk has saturated. The GSC fractions tend to converge to about 30% for all tumors, regardless of size, which reflects the fact that at the later stages of vascularization, the number of functional vessels is roughly independent of the initial GSC fraction and instead regulated by mechanical and chemical feedback signaling

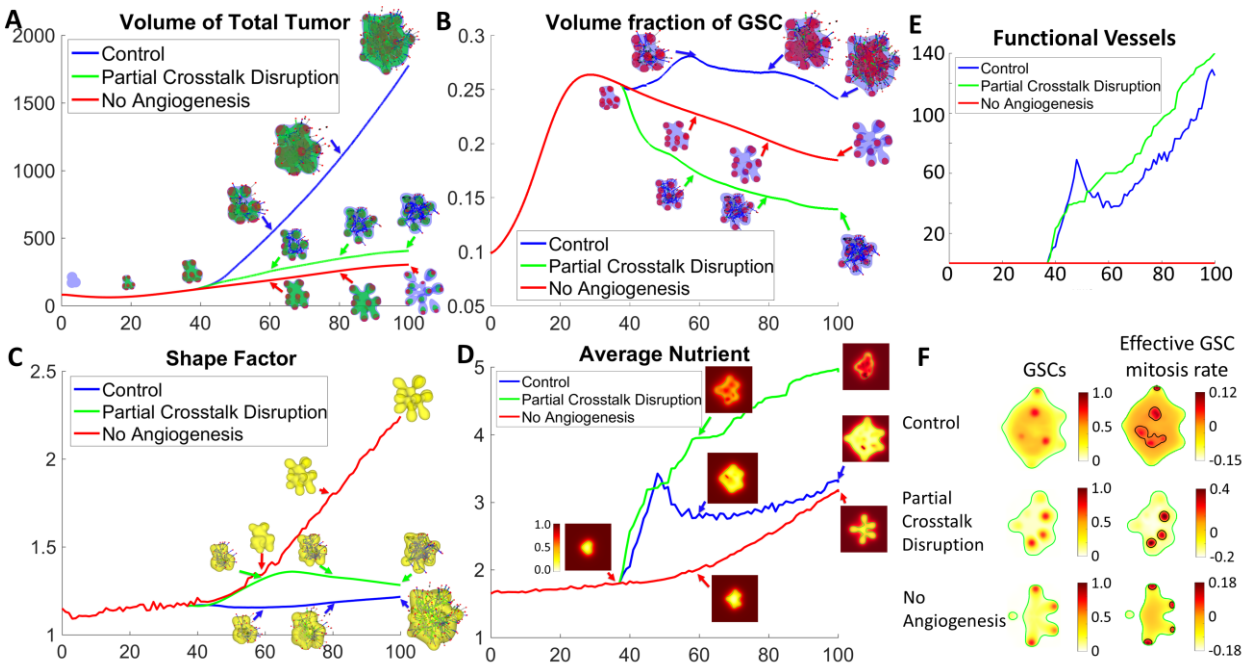


Figure 3.4 Treatment of vascularized GBM .A) Time evolution of total tumor volumes. Treatments that partially disrupt VEC-GSC crosstalk by blocking VEC secretion of the GSC promoter *F* (green) or angiogenesis (red) reduce tumor size compared to Control (blue, tumor from Fig. 1). **(B)** Blocking angiogenesis prevents the formation of a GSC cluster at the tumor center and reduces the GSC fraction. Blocking VEC-GSC crosstalk removes the positive feedback on GSC self-renewal and further reduces GSC fraction. **(C)** Blocking angiogenesis promotes finger development and significantly increases the tumor shape factor. Blocking the VEC-GSC crosstalk increases the shape factor at early times. At later times, GSC clusters are located closer to tumor center and fingers cease to grow, which reduces the shape factor. **(D)** Time evolution of average nutrient concentration in the tumor. Insets show slices of the nutrient distribution at the tumor center. **(E)** Between T=50 and T=60 in Control, pressure-induced vessel crushing reduces functional vessels, which recover after T=60. The functional vessels in tumors with VEC-GSC crosstalk blocked steadily increases. **(F)** Slices of GSC mitosis rate $\lambda_m^{SC} n(2p_0-1)$ at T=80 for the indicated tumors. Green: tumor boundary. Black: contours of $\lambda_m^{SC} n(2p_0-1)=0$. Blocking the crosstalk reduces the effective GSC mitosis at the tumor center, and GSC clusters are located off the tumor boundary due to higher nutrient levels at the center (see insets in (**D**)).

REFERENCES

124. Bonavia, R., et al., *Heterogeneity Maintenance in Glioblastoma: A Social Network.* Cancer Research, 2011. **71**(12): p. 4055-4060.
125. Tabatabai, G. and M. Weller, *Glioblastoma stem cells.* Cell and Tissue Research, 2011. **343**(3): p. 459-465.
126. Bayin, N.S., A.S. Modrek, and D.G. Placantonakis, *Glioblastoma stem cells: Molecular characteristics and therapeutic implications.* World J Stem Cells, 2014. **6**(2): p. 230-8.
127. Eyler, C.E. and J.N. Rich, *Survival of the Fittest: Cancer Stem Cells in Therapeutic Resistance and Angiogenesis.* Journal of Clinical Oncology, 2008. **26**(17): p. 2839-2845.
128. Ramírez-Castillejo C, S.-S.F., Andreu-Agulló C, Ferrón SR, Aroca-Aguilar JD, Sánchez P, Mira H, Escribano J, Fariñas I., *Pigment epithelium-derived factor is a niche signal for neural stem cell renewal.* Nat Neurosci, 2006. **9**(3): p. 331-9.
129. Calabrese, C., et al., *A perivascular niche for brain tumor stem cells.* Cancer Cell, 2007. **11**(1): p. 69-82.
130. Charles, N., et al., *Perivascular nitric oxide activates notch signaling and promotes stem-like character in PDGF-induced glioma cells.* Cell Stem Cell, 2010. **6**(2): p. 141-52.
131. Fan, X., et al., *NOTCH pathway blockade depletes CD133-positive glioblastoma cells and inhibits growth of tumor neurospheres and xenografts.* Stem Cells, 2010. **28**(1): p. 5-16.
132. Zhu, T.S., et al., *Endothelial cells create a stem cell niche in glioblastoma by providing NOTCH ligands that nurture self-renewal of cancer stem-like cells.* Cancer Res, 2011. **71**(18): p. 6061-72.
133. Merchant, A.A. and W. Matsui, *Targeting Hedgehog--a cancer stem cell pathway.* Clin Cancer Res, 2010. **16**(12): p. 3130-40.
134. Yan, G.N., et al., *Endothelial cells promote stem-like phenotype of glioma cells through activating the Hedgehog pathway.* J Pathol, 2014. **234**(1): p. 11-22.
135. Galan-Moya, E.M., et al., *Secreted factors from brain endothelial cells maintain glioblastoma stem-like cell expansion through the mTOR pathway.* EMBO Reports, 2011. **12**(5): p. 470-476.
136. Cristini, V. and J.S. Lowengrub, *Multiscale modeling of cancer: An integrated experimental and mathematical modeling approach*. 2010, Cambridge, UK: Cambridge University Press.
137. H. Rieger, T.F.a.M.W., *Physics of the tumor vasculature: Theory and experiment.* Eur. Phys. J. Plus, 2016. **131**(31).
138. Hartung, N., et al., *Mathematical modeling of tumor growth and metastatic spreading: validation in tumor-bearing mice.* Cancer Res, 2014. **74**(22): p. 6397-407.
139. Robertson-Tessi, M., et al., *Impact of metabolic heterogeneity on tumor growth, invasion, and treatment outcomes.* Cancer Res, 2015. **75**(8): p. 1567-79.
140. Gao, X., et al., *Acute and fractionated irradiation differentially modulate glioma stem cell division kinetics.* Cancer Res, 2013. **73**(5): p. 1481-90.
141. Gao, X., et al., *A proposed quantitative index for assessing the potential contribution of reprogramming to cancer stem cell kinetics.* Stem Cells Int, 2014. **2014**: p. 249309.
142. Youssefpour, H., et al., *Multispecies model of cell lineages and feedback control in solid tumors.* Journal of theoretical biology, 2012. **304**: p. 39-59.

143. Frieboes, H.B., et al., *Three-dimensional multispecies nonlinear tumor growth-II: Tumor invasion and angiogenesis.* J Theor Biol, 2010. **264**(4): p. 1254-78.
144. Wise, S.M., et al., *Three-dimensional multispecies nonlinear tumor growth--I Model and numerical method.* Journal of theoretical biology, 2008. **253**(3): p. 524-43.
145. Wise, S.M., J.S. Lowengrub, and V. Cristini, *An Adaptive Multigrid Algorithm for Simulating Solid Tumor Growth Using Mixture Models.* Math Comput Model, 2011. **53**(1-2): p. 1-20.
146. Jones, C.M., Armes, N., Smith, J.C., *Signalling by tgf-b family members: Short-range effects of xnr-2 and bmp-4 contrast with long-range effects of activin.* Curr. Biol., 1996. **6**(11): p. 1468-75.
147. Gregory, C.A., et al., *The Wnt signaling inhibitor dickkopf-1 is required for reentry into the cell cycle of human adult stem cells from bone marrow.* Journal of Biological Chemistry, 2003. **278**(30): p. 28067-28078.
148. Lee, N., et al., *A potential role for Dkk-1 in the pathogenesis of osteosarcoma predicts novel diagnostic and treatment strategies.* British Journal of Cancer, 2007. **97**(11): p. 1552-1559.
149. Klaus, A., Birchmeier., W., *Wnt signalling and its impact on development and cancer.* Nat. Rev. Cancer, 2008. **8**(5): p. 387-398.
150. Zhu M-L, H.C., Garzotto M, Qian DZ, Beer TM, Kyprianou N., *Tubulin-targeting chemotherapy impairs androgen receptor activity in prostate cancer.* Cancer research, 2010. **70**(20): p. 7992-8002.
151. Xiangxin Zhu, M.W., Fang Jin, and John Lowengrub, *Predicting Simulation Parameters of Biological Systems Using a Gaussian Process Model.* Stat Anal Data Min., 2012. **5**(6): p. 509-22.
152. Simonsen, T.G., et al., *High Interstitial Fluid Pressure Is Associated with Tumor-Line Specific Vascular Abnormalities in Human Melanoma Xenografts.* PLoS ONE, 2012. **7**(6): p. e40006.
153. Lunt, S.J., et al., *Interstitial fluid pressure in tumors: therapeutic barrier and biomarker of angiogenesis.* Future Oncology, 2008. **4**(6): p. 793-802.
154. Bao, S., et al., *Stem cell-like glioma cells promote tumor angiogenesis through vascular endothelial growth factor.* Cancer Res, 2006. **66**(16): p. 7843-8.
155. Hartnett, M.E., et al., *Neutralizing VEGF Decreases Tortuosity and Alters Endothelial Cell Division Orientation in Arterioles and Veins in a Rat Model of ROP: Relevance to Plus Disease.* Investigative ophthalmology & visual science, 2008. **49**(7): p. 3107-3114.
156. Folkins, C., et al., *Glioma tumor stem-like cells promote tumor angiogenesis and vasculogenesis via vascular endothelial growth factor and stromal-derived factor 1.* Cancer Res, 2009. **69**(18): p. 7243-51.
157. de Groot, J.F., et al., *Tumor invasion after treatment of glioblastoma with bevacizumab: radiographic and pathologic correlation in humans and mice.* Neuro-Oncology, 2010. **12**(3): p. 233-242.
158. Iwamoto, F.M., et al., *Patterns of relapse and prognosis after bevacizumab failure in recurrent glioblastoma.* Neurology, 2009. **73**(15): p. 1200-1206.
159. Cristini, V., et al., *Morphologic instability and cancer invasion.* Clin Cancer Res, 2005. **11**(19 Pt 1): p. 6772-9.

160. Sottoriva A, V.J., Borovski T, McWeeney SK, Naumov L, Medema JP, Sloot PM, Vermeulen L, *Cancer stem cell tumor model reveals invasive morphology and increased phenotypical heterogeneity.* Cancer Res., 2010. **70**(1): p. 46-56.
161. Cheng, L., et al., *Elevated Invasive Potential of Glioblastoma Stem Cells.* Biochemical and biophysical research communications, 2011. **406**(4): p. 643-648.
162. Cristini, V., J. Lowengrub, and Q. Nie, *Nonlinear simulation of tumor growth.* J Math Biol, 2003. **46**(3): p. 191-224.
163. Casanovas, O., et al., *Drug resistance by evasion of antiangiogenic targeting of VEGF signaling in late-stage pancreatic islet tumors.* Cancer Cell, 2005. **8**(4): p. 299-309.
164. Paez-Ribes, M., et al., *Antiangiogenic therapy elicits malignant progression of tumors to increased local invasion and distant metastasis.* Cancer Cell, 2009. **15**(3): p. 220-31.
165. Folkman, J., *Incipient Angiogenesis.* Journal of the National Cancer Institute, 2000. **92**(2): p. 94-95.
166. Bullitt, E., et al., *Vessel Tortuosity and Brain Tumor Malignancy: A Blinded Study.* Academic radiology, 2005. **12**(10): p. 1232-1240.
167. Saaristo, A., et al., *Adenoviral VEGF-C overexpression induces blood vessel enlargement, tortuosity, and leakiness but no sprouting angiogenesis in the skin or mucous membranes.* The FASEB Journal, 2002. **16**(9): p. 1041-1049.

Supplemental Materials

Sec. S1. Continuum tumor growth model

We follow [142, 144] and assume that the volume fractions satisfy the mass conservation equation

$$\frac{\partial \varphi_i}{\partial t} = -\nabla \cdot \mathbf{J}_i + Src_i - \nabla \cdot (\mathbf{u}\varphi_i), \qquad (1)$$

where $i = GSC, GCP, GTD, D \text{ or } T$. We introduce an adhesion energy $E = \frac{\gamma}{\varepsilon} \int f(\varphi_T) + \varepsilon^2 |\nabla \varphi_T|^2 dx$, where γ measures cell to cell adhesion, $f(\varphi_T) = \frac{1}{4}\varphi_T{}^2 (1-\varphi_T)^2$ is a double-well potential that penalizes mixing of the tumor ($\varphi_T \approx 1$) and host tissues ($\varphi_T \approx 0$). $\mathbf{J}_i$ is a flux taken to be the generalized Fick's law $\mathbf{J}_i = -M\chi\nabla\left(\frac{\delta E}{\delta \varphi_i}\right)$, where M is the cell mobility, $\frac{\delta E}{\delta \varphi_i}$ is the variational derivative of the adhesion energy, $\frac{\delta E}{\delta \varphi_i} = \frac{\gamma}{\varepsilon}\left(f'(\varphi_T) - \varepsilon^2 \nabla^2 \varphi_T\right)$.

The term $\nabla \cdot (\mathbf{u}\varphi_i)$ models passive cell movement (advection), where $\mathbf{u}$ is the mass-averaged velocity of solid components defined by Darcy's law

$$\mathbf{u} = -\left(\nabla p - \frac{\delta E}{\delta \varphi_T}\nabla \varphi_T\right) \qquad (2)$$

Where p is the solid, or mechanical, pressure. To solve for p, we assume that $Src_H = 0$, e.g. homeostasis. We sum up Eq. (1) for all cell components and define $Src_T = Src_{GSC} + Src_{GCP} + Src_{GTD} + Src_D$ as the mass exchange term for total tumor cells, then $\nabla \cdot \mathbf{u} = Src_T$. The solid pressure can then be solved by

$$-\nabla^2 p = Src_T - \nabla \cdot \left(\frac{\delta E}{\delta \varphi_T}\nabla \varphi_T\right). \qquad (3)$$

It can be shown that the adhesion energy is non-increasing in time in the absence of cell proliferation and death, given our choices of flux and velocity terms [144]. To model the advection of cell substrates with the interstitial liquid velocity, we also use Darcy's law to relate the water pressure q and the interstitial fluid velocity $\mathbf{u}_w$ by $\mathbf{u}_w = -\nabla q$. Since the sum of all the solid and liquid volume fractions is one, we obtain [144]:

$$-\nabla^2 q = -Src_T. \qquad (4)$$

Sec. S2. Pattern Formation and Feedback Regulation

We follow [142] and assume that there is a short range self-renewal promoter C_W and a long range inhibitor C_{WI}. Both C_W and C_{WI} are produced by GSCs [149] and their production rates are proportional to the nutrient level. We take a generalized Gierer-Meinhardt model

$$\begin{aligned}\frac{\partial C_W}{\partial t}+\nabla\cdot(\mathbf{u}_w C_W)&=\nabla\cdot(D_W\nabla C_W)+kF(C_W,C_{WI})\\ \frac{\partial C_{WI}}{\partial t}+\nabla\cdot(\mathbf{u}_w C_{WI})&=\nabla\cdot(D_{WI}\nabla C_{WI})+kG(C_W,C_{WI}),\end{aligned}\tag{5}$$

where $\nabla\cdot(\mathbf{u}_w C_W)$ and $\nabla\cdot(\mathbf{u}_w C_{WI})$ model advection with the interstitial water velocity, D_W and D_{WI} are the diffusivities, k is the reaction rate. We take non-linear reaction terms

$$\begin{aligned}F(C_W,C_{WI})&=p_W\frac{C_W^2}{C_{WI}}n\varphi_{GSC}-d_W C_W+u_0 n(\varphi_T-\varphi_D)\\ G(C_W,C_{WI})&=p_{WI}C_W^2 n\varphi_{GSC}-d_{WI}C_{WI},\end{aligned}\tag{6}$$

where p_W, p_{WI} are production rates, d_W and d_{WI} are natural decay rates. u_0 models a background nutrient-dependent production of C_W from all viable cells.

In addition, we assume that GTDs produce negative feedback regulators C_{T1} on GSC self-renewal and C_{T2} on GCP self-renewal. Accordingly, we take

$$\begin{aligned}0&=\nabla\cdot(D_{T1}\nabla C_{T1})-(u_{T1}^{GSC}\varphi_{GSC}+d_{T1})C_{T1}+p_{T1}\varphi_{GTD}\\ 0&=\nabla\cdot(D_{T2}\nabla C_{T2})-(u_{T2}^{GCP}\varphi_{GCP}+d_{T2})C_{T2}+p_{T2}\varphi_{GTD},\end{aligned}\tag{7}$$

where D_{T1}, d_{T1} and p_{T1} are the diffusivity, natural decay and production rates by GTDs, respectively. u_{T1}^{GSC} is the uptake rate by GSCs; parameters for C_{T2} are defined analogously.

Sec. S3. Detailed analysis of different VEGF sources

We investigate the effects of different VEGF sources in more detail than shown in Fig. 2 in the main text. Fig. S1 shows the neovascular network and tumor when the sources of VEGF are GSCs and GCPs. Fig. S2 shows the dynamics of the GCP and GTD volume fractions, and Fig. S3 shows the solid pressure in the tumors.

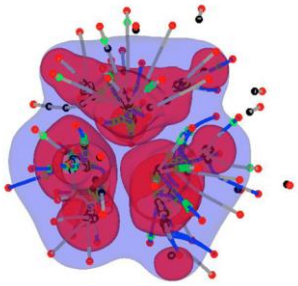


Fig. S1. Distribution of GSCs and the vessel network in the tumor with $S_V = p_V\left(f_{GSC} + f_{GCP}\right)$ in Fig. 2 (in main text) at T=63. Blue: $\varphi_T = 0.5$ surface; red: $\varphi_{GSC} = 0.3$ surface. Red dots: sprout roots; grey: sprouts, blue: functional vessels. Note that vessels are mainly located at GSC clusters, which reduces solid pressure (Fig. S3), results in less vessel crushing and decreased vessel tortuosity.

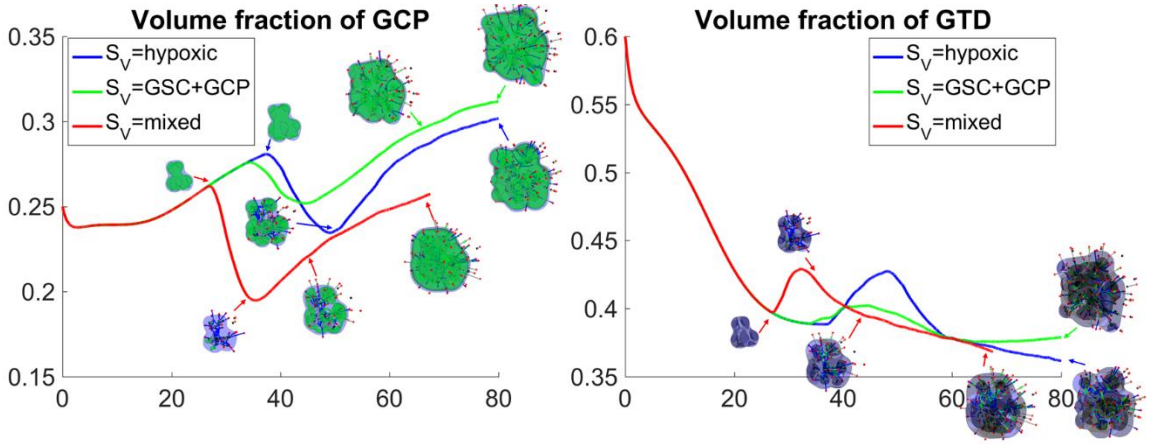


Fig. S2. Volume fractions of GCPs (left) and GTDs (right) in Fig. 2 (main text). After angiogenesis starts (T~40 for S_V=hypoxic cells (blue), T~32 for S_V=GSC+GCP (green), T~25 for S_V=mixed (red)). The GCP fractions in the tumors are seen to be non-monotone with the minimum value occurring just after angiogenesis. This is accompanied by a local maximum in the GTD fractions. This is due to increased GSC self-renewal from VEC-GSC crosstalk that decreases replenishment of GCPs following their differentiation into GTDs. However, the fractions recover at later times, as a small portion of the large GSC population differentiates into GCPs.

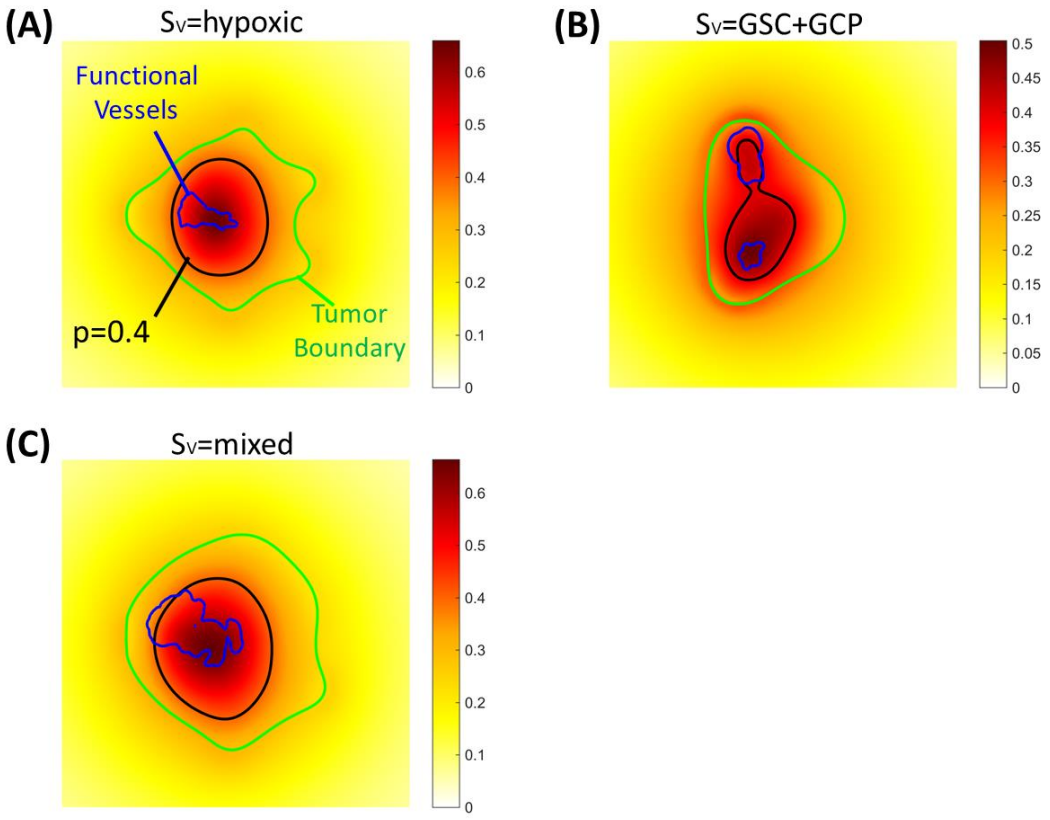


Fig. S3. 2D Slice of solid pressure in tumors in Fig. 2 (main text) at T=67, with indicated VEGF sources. Green: tumor boundary, black: p=0.4 contour (vessel crushing threshold), blue: functional vessel density $\rho_{FV}=5$ contour. **(A)** When all hypoxic cells produce VEGF, the tumor has a large GSC cluster at the center (see Figs. 1 and 2 in main text). GSC proliferation creates high pressure that shuts down functional vessels. **(B)** When only GSCs and GCPs produce VEGF, the tumor has several smaller GSC spots instead of a major cluster at the center. As a result, the solid pressure is reduced and fewer functional vessels are crushed. Since the tumor has a similar amount of VEGF compared to (**A**) (see Fig. 2G in main text, blue and green), the number of functional vessels is larger than that of (A) (Fig. 2E in main text). **(C)** When the source of VEGF is mixed (hypoxic cells and GSCs and GTDs), a large GSC cluster forms at the tumor center, which is similar to (**A**). However, the tumor has a much larger amount of VEGF and so even though there is vessel crushing, this tumor has the largest number of functional vessels.

Sec. S4. Detailed analysis of initial GSC fractions

In this section, we present details on the effects of initial GSC fractions on the tumor and vasculature to supplement Fig. 3 in the main text. Fig. S4 shows the GCP and GTD volume fractions in the tumors. Fig. S5 shows the total VEGF in the tumors. In Fig. S6, we consider the corresponding dynamics when the sources of VEGF are mixed, e.g., $S_V = H(\tilde{n}-n)(\varphi_{GSC}+\varphi_{GCP}+\varphi_{GTD})+(\varphi_{GSC}+\varphi_{GCP})$. In Fig. S7, we consider the dynamics when the vessel sprouting probabilities and pressure crushing thresholds are changed.

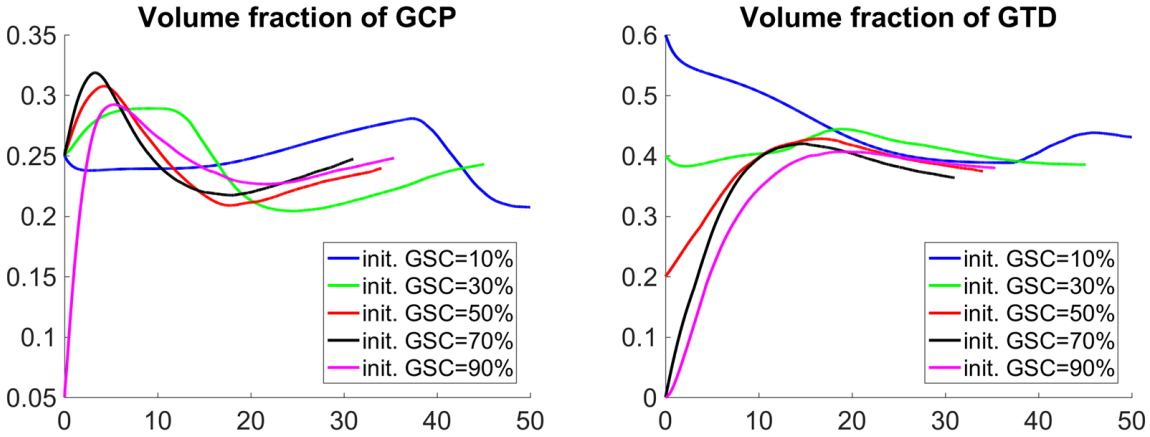


Fig. S4. Volume fractions of GCPs and GTDs from Fig. 3 (main text). After angiogenesis starts (T~40 for the tumor with 10% initial GSCs, T~10 for 30% initial GSCs, T~3 for 50%, 70% and 90%), the fractions of GCPs begin to drop, as seen in Fig. S3, before recovering at later times. After the tumor is vascularized, higher initial GSC fractions generally result in higher GCP fractions (see also Fig. 3A in the main text between T=17 and T=25). The fractions of GTDs are correspondingly non-monotone. Unlike GSCs, the fractions of GCPs and GTDs do not converge to a common value as time evolves.

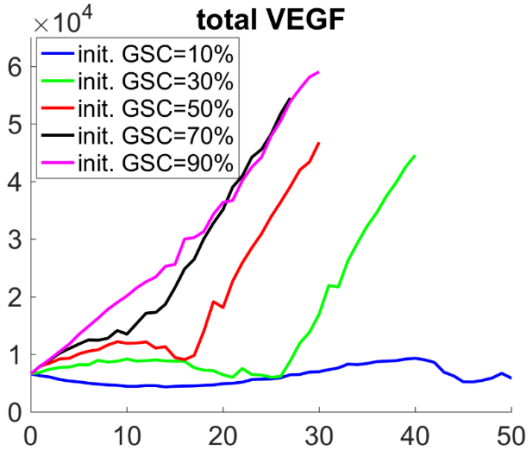


Fig. S5. Total amounts of VEGF in tumors in Fig. 3 (main text) with different initial GSC fractions. In general, larger initial GSC fractions increase VEGF production.

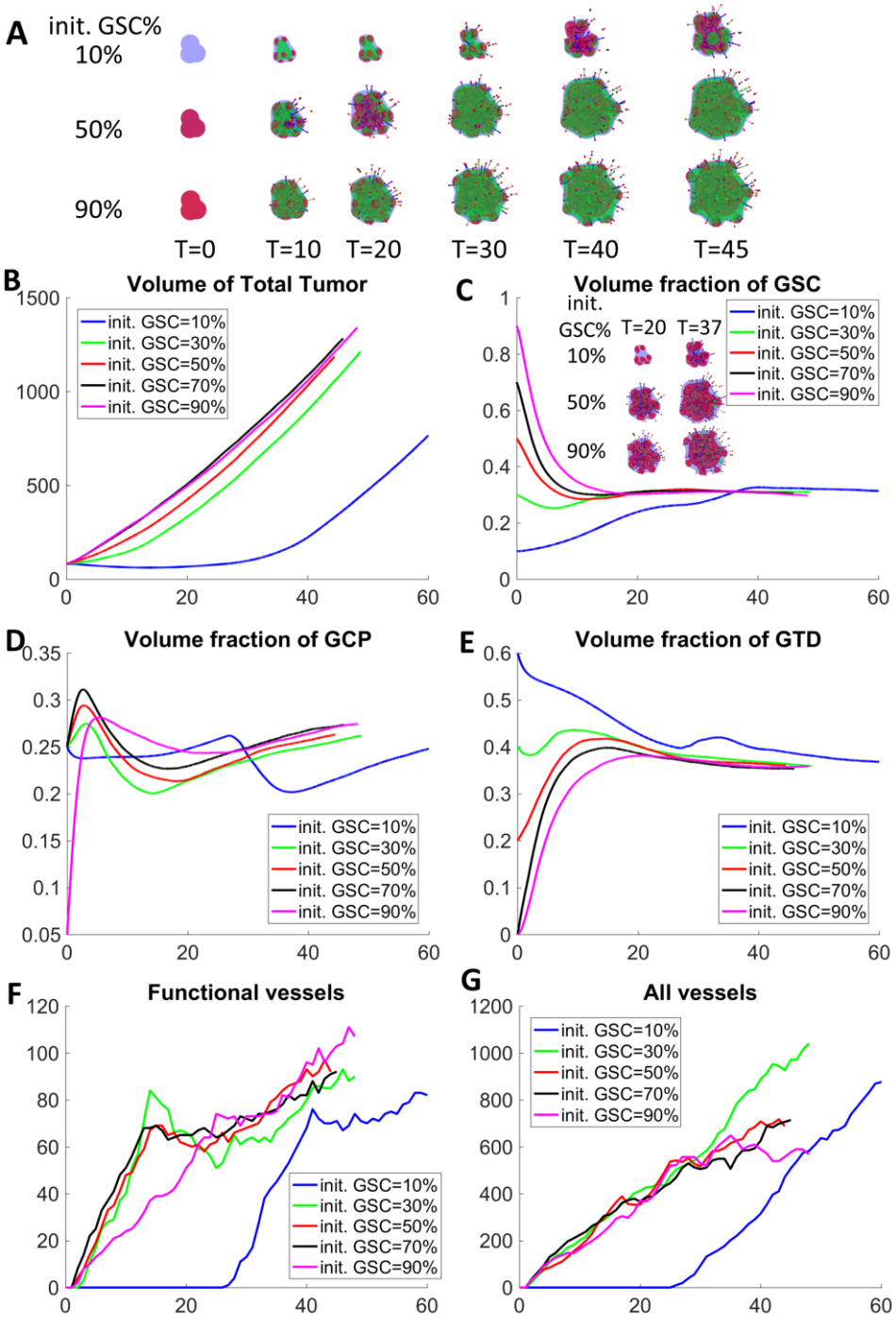


Fig. S6. The effect of initial GSC fractions in tumors with mixed VEGF production: $S_V = p_V H(\tilde{n}-n)(\varphi_{GSC}+\varphi_{GCP}+\varphi_{GTD})+p_V(\varphi_{GSC}+\varphi_{GCP})$. **(A)** Evolution of tumors with different initial GSC fractions at indicated times. **(B)** Time evolution of total volumes, **(C)** GSC fractions, **(D)** GCP fractions, **(E)** GTD fractions, **(F)** numbers of functional vessels and **(G)** numbers of all vessels. Higher initial GSC fractions result in larger tumor sizes except for the 90% case. At late times, the GSC fraction of all cases converges to approximately 30% despite differences in tumor sizes. Tumors with initial GSC fraction larger than 10% develop similar numbers of vessels, indicating that the control of initial GSC fraction over vessel numbers has saturated.

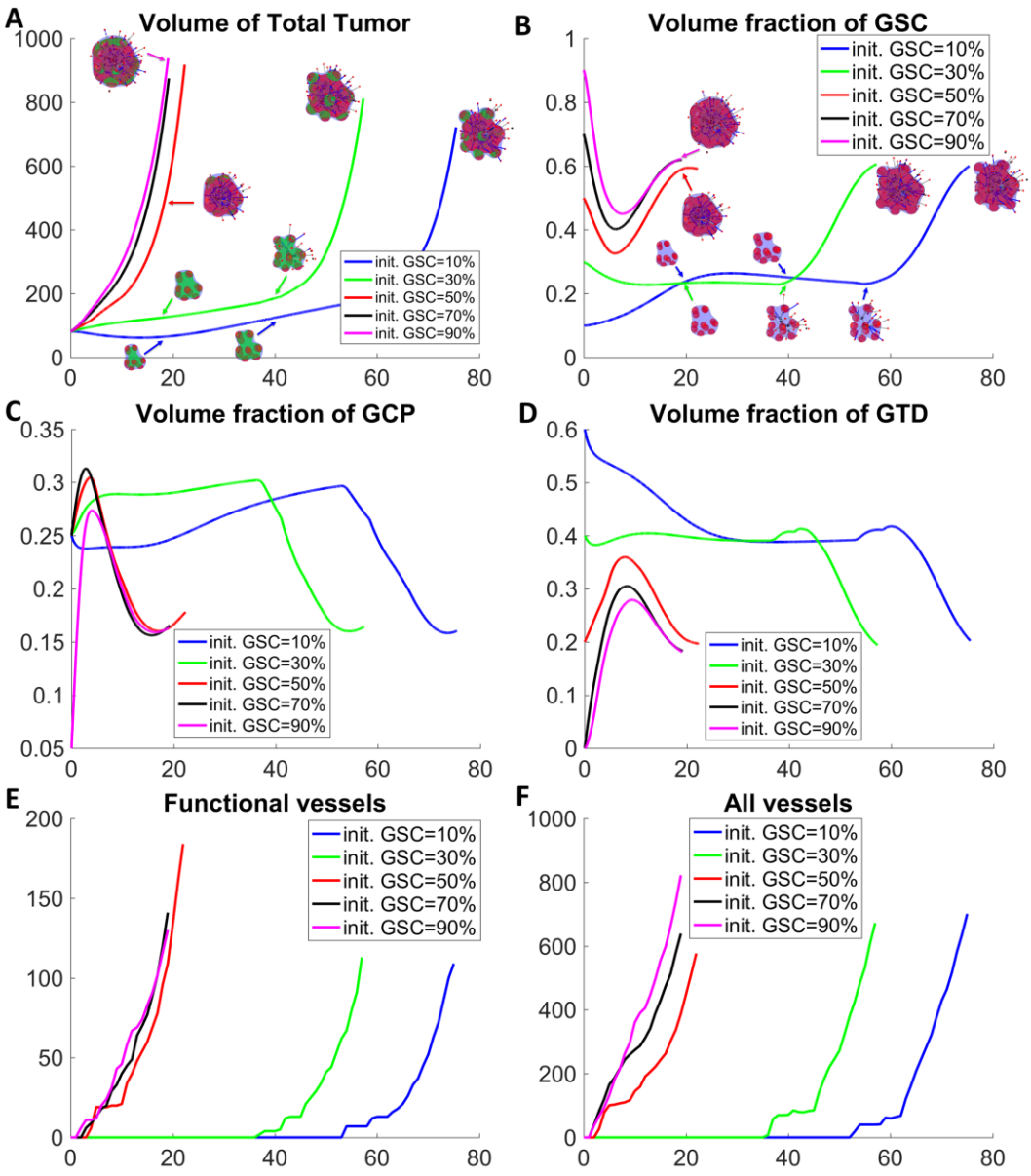


Fig. S7. Increased sensitivity of vessel sprouting distinguishes vasculature characteristics by initial GSC fractions. In Fig. **S6** and in the simulations presented in the main text, the vessel sprouting probability is $\xi = 0.05$ once $C_V > 0.01$. Here, we change the probability to $\xi = \frac{(6C_V)^8}{1+(6C_V)^8}$, and we eliminate vessel crushing (e.g., we set the pressure crushing threshold to infinity). Typical VEGF concentrations in the tumor range from $C_V = 0$ to $C_V > 0.2$. **(A-G)** Time evolution of total volumes, GSC fractions, GCP fractions, GTD fractions, numbers of functional vessels and all vessels respectively. Tumors with higher initial GSC fractions have larger numbers of vessels and functional vessels. In contrast to Fig. **S6 C**, GSC fractions begin to increase after vessel formation. This suggests that GSC fractions are affected by the vascular sensitivity to VEGF through positive feedback factors secreted by the VECs.

Sec. S5. Detailed analysis of cancer therapies

Here, we present additional details of the response of tumors to cancer therapies, from Fig. 4 in the main text. In Fig. S8, the volume fractions of GCPs and GTDs are shown and in Fig. S9, the corresponding pressure distributions are given.

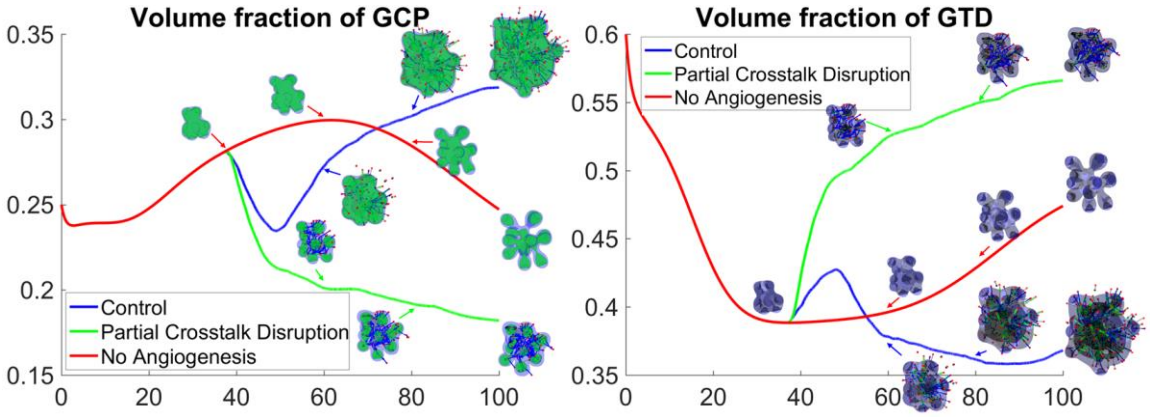


Fig. S8. Volume fractions of GCPs and GTDs from Fig. 4 in the main text. The GSC fraction is highest in Control (see Fig. 4B in the main text). Consequently, the GCP fraction is also the highest whereas the GTD fraction is reduced. When the crosstalk is partially disrupted by blocking VEC secretion of GSC promoters, the GSC cluster at tumor center is removed. The GSC fraction drops, which results in smaller GCP fractions. In addition, GCP differentiation is enhanced by nutrients released from functional vessels, which increases their proliferation and hence differentiation rates.

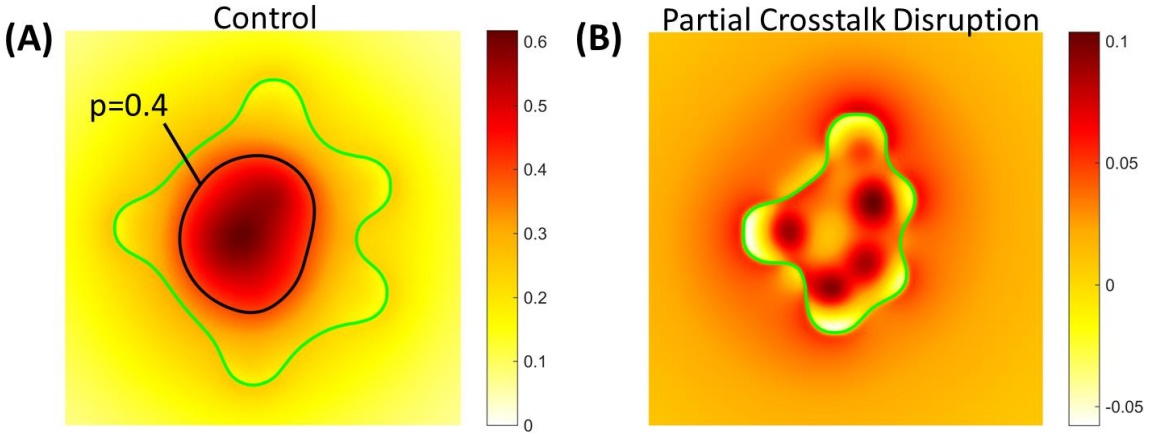


Fig. S9. 2D Slice of solid pressure at z=0 in Control **(A)** and Partial Crosstalk Disruption **(B)** in Fig. 4 (main text) at T=80. Green: tumor boundary, black: p=0.4 contour (vessel crushing threshold). In Control, vessels are shut down by excessive solid pressure. However, when crosstalk is partially disrupted by blocking VEC secretion of GSC promoters, the pressure is only generated at GSC spots and does not exceed the crushing threshold.

Sec. S6. Nondimensionalization and Model Parameters

Let L and T be the length and time scale respectively. We follow [142] and choose L to be the nutrient diffusion length $L=\sqrt{D_n/u_n^{GSC}}$. Since the nutrient concentration is measured against that in the vasculature, we nondimensionalize n as $n'=n/\bar{n}$. Denoting $\nabla'=\nabla/L$ as the dimensionless

gradient, we rewrite the equation for the dimensionless nutrient concentration n':

$$0 = \Delta' n' - \left(\varphi_{GSC} + u_n'^{GCP}\varphi_{GCP} + u_n'^{GTD}\varphi_{GTD} + d_n'\right)n' + \left(p_n'^{H}Q(\varphi_T) + p_n'^{V}\rho_{FV}\right)(1-n'),$$

where $u_n'^{GCP} = u_n^{GCP}/u_n^{GSC}$, $u_n'^{GTD} = u_n^{GTD}/u_n^{GSC}$, $d_n' = d_n/u_n^{GSC}$, $p_n'^{H} = p_n'^{H}/u_n^{GSC}$ and $p_n'^{V} = p_n'^{V}/u_n^{GSC}$.

Next, we nondimensionalize the mass conservation equations Eq. (1) in Main Text. Let $t' = t/T$ be the dimensionless time, $\mathbf{u}' = \mathbf{u}/(L/T)$, $M' = M/\overline{M}$ and $\mu' = \mu/\overline{\mu}$ be the nondimensionalized cell velocity, mobility and chemical potential respectively. We rewrite the equation for φ_T as

$$\frac{1}{T\lambda_m^{GCP}\overline{n}}\left(\frac{\partial\varphi_T}{\partial t'} + \nabla'\cdot(\mathbf{u}'\varphi_T)\right) = \frac{\overline{M}\cdot\overline{\mu}}{L^2\lambda_m^{GCP}\overline{n}}\nabla'\cdot\left(M'\varphi_T\nabla'\mu'\right) + \lambda_m'^{GSC}n'\varphi_{GSC} + n'\varphi_{GCP} - \lambda_L'\varphi_D.$$

We choose time scale $T = \left(\lambda_m^{GCP}\overline{n}\right)^{-1}$ and $\frac{\overline{M}\cdot\overline{\mu}}{L^2\lambda_m^{GCP}\overline{n}} = 1$. $\lambda_m'^{GSC} = \lambda_m^{GSC}/\lambda_m^{GCP}$, $\lambda_L' = \lambda_L/\lambda_m^{GCP}$. Analogously, the dimensionless equations for other cell species are

$$\frac{\partial\varphi_{GSC}}{\partial t'} + \nabla'\cdot(\mathbf{u}'\varphi_{GSC}) = \nabla'\cdot\left(M'\varphi_{GSC}\nabla'\mu'\right) + \lambda_m'^{GSC}n'\varphi_{GSC}(2p_0 - 1),$$

$$\frac{\partial\varphi_{GCP}}{\partial t'} + \nabla'\cdot(\mathbf{u}'\varphi_{GCP}) = \nabla'\cdot\left(M'\varphi_{GCP}\nabla'\mu'\right) + \lambda_m'^{GSC}n'\varphi_{GSC}2(1-p_0) + n'\varphi_{GCP}(2p_1 - 1),$$

$$\frac{\partial\varphi_{GTD}}{\partial t'} + \nabla'\cdot(\mathbf{u}'\varphi_{GTD}) = \nabla'\cdot\left(M'\varphi_{GTD}\nabla'\mu'\right) + n'\varphi_{GCP}\,2(1-p_0) - \lambda_a'^{GTD}\varphi_{GTD},$$

$$\frac{\partial\varphi_D}{\partial t'} + \nabla'\cdot(\mathbf{u}'\varphi_D) = \nabla'\cdot\left(M'\varphi_D\nabla'\mu'\right) + \lambda_a'^{GTD}\varphi_{GTD} - \lambda_L'\varphi_D.$$

Here $\lambda_a'^{GTD} = \lambda_a^{GTD}/\lambda_m^{GCP}$.

The dimensionless velocity $\mathbf{u}'$ satisfies $\frac{L}{T}\mathbf{u}' = -\frac{\overline{p}}{L}\nabla' p' + \frac{\overline{\mu}}{L}\frac{\lambda}{\varepsilon}\mu'\nabla'\varphi_T$, where $p' = p/\overline{p}$ is the dimensionless pressure. We choose $\overline{p} = \overline{\mu} = \frac{L^2}{T}$, then

$$\mathbf{u}' = -\nabla' p' + \frac{\lambda}{\varepsilon}\mu'\nabla'\varphi_T, \qquad \mu' = \left(\frac{df}{d\varphi}(\varphi_T) - \varepsilon^2\nabla'^2\varphi_T\right).$$

The dimensionless equation for C_V is

$$0 = \Delta' C_V - d_V' C_V + S_V',$$

where $d_V' = L^2 d_V/D_V$ and $S_V' = L^2 S_V/D_V$. Analogously, we nondimensionalize the equations for C_{T1} and C_{T2}:

$$0 = \Delta' C_{T1} - \left(u'^{GSC}_{T1}\varphi_{GSC} + d'_{T1}\right)C_{T1} + p'_{T1}\varphi_{GTD}$$
$$0 = \Delta' C_{T2} - \left(u'^{GCP}_{T2}\varphi_{GCP} + d'_{T2}\right)C_{T2} + p'_{T2}\varphi_{GTD},$$

where $u'^{GSC}_{T1} = L^2\, u^{GSC}_{T1}/D_{T1}$, $d'_{T1} = L^2\, d_{T1}/D_{T1}$ and $p'_{T1} = L^2\, p_{T1}/D_{T1}$. The parameters for C_{T2} are defined similarly.

The dimensionless equation for C_F is

$$\frac{\partial C'_F}{\partial t'} + \nabla' \cdot \left(\mathbf{u}'_w C'_F\right) = \Delta' C_F - d'_F C'_F + p'^V_F \rho_V \left(1 - C'_F\right),$$

where $C'_F = C_F/\overline{C_F}$, $\mathbf{u}'_w = \mathbf{u}_w/(L/T)$, $d'_F = \frac{L^2}{TD_F} d_F$ and $p'^V_F = \frac{L^2}{TD_F} p^V_F$. Analogously, the dimensionless equation for C_W and C_{WI} are

$$\frac{\partial C_W}{\partial t'} + \nabla' \cdot \left(\mathbf{u}'_w C_W\right) = D'_W \Delta' C_W + k' F\left(C_W, C_{WI}\right)$$
$$\frac{\partial C_{WI}}{\partial t'} + \nabla' \cdot \left(\mathbf{u}'_w C_{WI}\right) = D'_{WI} \Delta' C_{WI} + k' G\left(C_W, C_{WI}\right),$$

where $D'_W = \frac{T}{L^2} D_W$ and $D'_{WI} = \frac{T}{L^2} D_{WI}$. We take $k' = \frac{T}{L^2 p_W n} = k$ and the reaction terms

$$F\left(C_W, C_{WI}\right) = \frac{C_W^2}{C_{WI}} n' \varphi_{GSC} - d'_W C_W + u'_0 n' \left(\varphi_T - \varphi_D\right)$$
$$G\left(C_W, C_{WI}\right) = p'_{WI} C_W^2 n' \varphi_{GSC} - d'_{WI} C_{WI},$$

where $d'_W = \frac{d_W}{p_W n}$, $u'_0 = \frac{u_0}{p_W}$, $p'_{WI} = \frac{p_{WI}}{p_W}$ and $d'_{WI} = \frac{d_{WI}}{p_W n}$.

The model parameters are listed below for the simulations in Main Text. Although we present results for this basic set of parameters, the behavior we present is characteristic of that obtained by a wide range of parameter choices.

Table S1. Model Parameters

General Parameters		
Cell Mobility	$M = 100$	From [142].
Adhesion force	$\gamma = -0.1$	
Diffuse interface thickness	$\varepsilon = 0.05$	
Tumor Species		
GSC mitosis rate	$1/\tau_m^{GSC} = 0.7$	We follow [140] and assume that the GSC division rate is similar to that for dividing non-GSC cells (here, this is the GCP population). $1/\tau_m^{GCP}$, Nondimensionalization parameter. Typically on the order of 24 hours [140].
GCP mitosis rate	$1/\tau_m^{GCP} = 1.0$	
GTD death rate	$1/\tau_a^{GTD} = 0.28$	
Dead cell lysis rate	$1/\tau_L^{D} = 1.41$	

		l_a^{GTD} and l_L^D obtained by numerical experimentation. Results are qualitatively similar for a wide range of these parameter choices.
Feedback control		
Minimum GSC self-renewal probability	$p_0^{\min} = 0.2$	See [142].
Maximum GSC self-renewal probability	$p_0^{\max} = 1.0$	
Positive feedback gain on p_0 by C_W	$\chi_0^W = 1.0$	
Negative feedback gain on p_0 by C_{T1}	$\psi_0 = 0.1$	
Maximum fold change of λ_m^{GSC}	$\Delta_m^F = 1.0$	From [168], which suggested that the crosstalk increases GSC proliferation by 50% to 100%. Magnitudes of feedback gains determined by numerical experimentation. Results are qualitatively similar for a wide range of these parameter choices.
Positive feedback gain on λ_m^{GSC}	$\chi_m^F = 2.0$	
Positive feedback gain on p_0 by C_F	$\chi_0^F = 2.0$	
Minimum GCP self-renewal probability	$p_1^{\min} = 0.2$	Parameters obtained by numerical experimentation. As long as $p_1^{\max} < 0.5$, the results are qualitatively similar for a wide range of these parameter choices.
Maximum GCP self-renewal probability	$p_1^{\max} = 0.45$	
Positive feedback gain on p_1 by C_W	$\chi_1^W = 1.0$	
Negative feedback gain on p_1 by C_{T2}	$\psi_1 = 0.1$	
Nutrient		
Diffusivity	$D_n = 0.5$	From [142].
Natural decay rate	$d_n = 1.0$	
Uptake rate by GSCs, GCPs and GTDs	$u_n = 1.0$	
Production rate by microenvironment	$p_n^H = 1.0$	
Production rate by functional vessels	$p_n^V = 1.0$	From [143].
VEGF		
Diffusivity	$D_V = 1.0$	From [143].
Natural decay rate	$d_V = 2.0$	
Production rate by all hypoxic cells	$p_V = 1.0$	
Hypoxic region threshold	$\tilde{n} = 0.5$	
Pattern formation		
Diffusivity of C_W	$D_W = 1.0$	From [142].
Production rate of C_W	$p_W = 1.0$	
Natural decay rate of C_W	$d_W = 1.0$	
Leak term of C_W	$u_0 = 0.2$	
Diffusivity of C_{WI}	$D_{WI} = 1.0$	

Production rate of C_{WI}	$p_{WI} = 1.0$	
Natural decay rate of C_{WI}	$d_{WI} = 1.0$	
Reaction rate	$k = 25.0$	
Crosstalk factor C_F		
Diffusivity	$D_F = 1.0$	Parameters obtained by numerical experimentation. Results are qualitatively similar for a wide range of these parameter choices.
Natural decay rate	$d_F = 1.0$	
Production rate by vasculature	$p_F = 0.2$	
Negative feedback factors		
Diffusivity	$D_{T1} = D_{T2} = 1.0$	From [142].
Production rate by GTDs	$p_{T1} = p_{T2} = 1.0$	
Uptake rate of C_{T1} by GSCs	$u_{T1}^{GSC} = 0.1$	
Uptake rate of C_{T2} by GCPs	$u_{T2}^{GCP} = 0.1$	
Vessel network		
Vessel sprouting probability	$\xi = 0.05$	From [143].
Minimum VEGF required for sprouting	$C_V = 0.01$	
Vessel crushing threshold	$p > 0.4$	
Vessel crushing probability once $p > 0.4$	$\zeta = 0.1$	

REFERENCES

140. Gao, X., et al., *Acute and fractionated irradiation differentially modulate glioma stem cell division kinetics.* Cancer Res, 2013. **73**(5): p. 1481-90.
142. Youssefpour, H., et al., *Multispecies model of cell lineages and feedback control in solid tumors.* Journal of theoretical biology, 2012. **304**: p. 39-59.
143. Frieboes, H.B., et al., *Three-dimensional multispecies nonlinear tumor growth-II: Tumor invasion and angiogenesis.* J Theor Biol, 2010. **264**(4): p. 1254-78.
144. Wise, S.M., et al., *Three-dimensional multispecies nonlinear tumor growth--I Model and numerical method.* Journal of theoretical biology, 2008. **253**(3): p. 524-43.
149. Klaus, A., Birchmeier., W., *Wnt signalling and its impact on development and cancer.* Nat. Rev. Cancer, 2008. **8**(5): p. 387-398.
168. Borovski T, V.J., ten Cate R, Cameron K, de Vries NA, van Tellingen O, Richel DJ, van Furth WR, Medema JP, Sprick MR., *Tumor microvasculature supports proliferation and expansion of glioma-propagating cells.* Int J Cancer, 2009. **125**(5): p. 1222-30.

CHAPTER 4. 3D Mathematical modeling of vascularized glioblastoma reveals that transdifferentiated vascular or vascular-supporting cells promote resistance to combinatorial therapies

H. Yan[4], M. Romero-López[2], H.B. Frieboes [5,6,7], C.C.W. Hughes [1,2,3], J.S. Lowengrub [2,4]

[1]Department of Molecular Biology and Biochemistry, School of Biological Sciences, [2]Department of Biomedical Engineering, The Henry Samueli School of Engineering, [3]The Edwards Lifesciences Center for Advanced Cardiovascular Technology, [4]Department of Mathematics, University of California Irvine, Irvine, CA 92697, [5]Department of Biomedical Engineering, [6]James Brown Cancer Center, [7]Department of Pharmacology and Toxicology, University of Louisville.

Abstract

Glioblastoma is highly heterogeneous, vascularized and one of the deadliest brain tumors with poor prognosis. Cancer stem cells (CSCs) are found to play a crucial role in cell hierarchy and increase cancer aggressiveness. Recently, crosstalk between CSCs and capillaries has been shown to considerably enhance tumor growth, and CSCs can also transdifferentiate into vascular endothelial cells (gECs) that maintain their stemness. gECs inherit mutations present in CSCs and are resistant to traditional therapies. Therefore, cancer therapeutics for glioblastoma remains a challenge. In this paper, we model the glioblastoma growth by a three-dimensional spatiotemporal mathematical model that accounts for a branched tumor cell lineage and angiogenesis. CSC clusters form near the tumor boundary as an effect of a Turing-type pattern formation system, and develop into fingers that drive tumor invasion. gECs spontaneously form a network within the hypoxic core, consistent with experimental findings. The model is then used to investigate the effects of cancer therapies. We demonstrate that traditional anti-angiogenic therapies decelerate tumor growth, but make the tumor highly invasive. Chemotherapies help to

reduce tumor sizes, but cannot control the invasion. Anti-CSC therapies that promote differentiation or disturb the stem cell niche effectively reduce tumor invasiveness. Anti-gEC treatments block the support on CSCs by gECs and reduce tumor sizes. Our study suggests that therapies targeting the vasculature, CSCs and gECs, when combined, are highly synergistic and are capable of controlling both tumor size and shape.

Major Findings

We developed a mathematical model to investigate the growth of vascularized glioblastoma and its response to cancer therapies. We demonstrated that traditional anti-angiogenic therapy decelerates tumor growth but increase tumor invasion. Anti-CSC therapies are shown to control tumor invasion. gECs support CSC proliferation and self-renewal, and increase tumor resistance to cancer therapies. Therefore, combinatorial therapies that incorporate an anti-gEC/gPericyte component can be highly synergistic.

Quick Guide to Equations and Assumptions

We model the tumor progression following the multispecies mixture model from [142, 143]. Tumor cell species are modeled as volume fractions that satisfy mass conservation equations that account for cell motility, mitosis and apoptosis. Cell proliferation increases local solid pressure, and tumor cells move from high pressure regions to low pressure. Spatiotemporally varying signaling factors released by tumor cells, the vasculature and microenvironment regulate cell proliferation, differentiation and self-renewal. In particular, the volume fractions of total tumor cells (φ_T), gCSCs (φ_{SC}), CPs (φ_{CP}), transdifferentiated gECs (φ_{EC}) and dead cells (φ_D) satisfy mass conservation equation

$$\frac{\partial \varphi_i}{\partial t} + \nabla \cdot (\boldsymbol{u_s} \varphi_i) = \nabla \cdot (M \varphi_i \nabla \mu) + Src_i, \qquad (1)$$

where i=T, SC, CP, EC or D. $\nabla \cdot (\boldsymbol{u_s} \varphi_i)$ models passive cell movement by pressure (Darcy's law). $\nabla \cdot (M \varphi_i \nabla \mu)$ accounts for surface tension and the phase separation of the tumor ($\varphi_T = 1$) and host tissues ($\varphi_T = 0$). We refer to the Methods section for details.

Src_i models the mass exchange of φ_i. gCSCs initiate tumor progression and have a branched fate. We assume that oxygen/nutrient delivery (*n*) from microvasculature provides positive feedback to gCSC proliferation rate. When gCSCs divide, they may self-renew, differentiate to CPs responsible for tumorigenesis, or transdifferentiate to gECs/gPericytes for tumor angiogenesis. CPs may also self-renew or differentiate to TDs that are subject to apoptosis.

We assume that gCSCs produce a short-range activator C_W (e.g. Wnt [169]) that promotes their self-renewal possibility p_0, and a long-range Wnt-inhibitor C_{WI} (e.g. Dkk [147, 148]) that constitute a Turing-type pattern formation system [54]. TDs release factors C_{T1} and C_{T2} (e.g. TGF- β superfamily members [170]) that suppresses gCSC and CP self-renewal possibilities, respectively. In addition, the crosstalk between CSCs and capillaries is modeled by a combined signaling factor C_F that enhances p_0. Assuming the maximum and minimum self-renewal levels are p_0^{max} and p_0^{min}, we take

$$p_0 = p_0^{min} + \left(p_0^{max} - p_0^{min}\right) \cdot \frac{\chi_0^W C_W + \chi_0^F C_F}{1 + \chi_0^W C_W + \chi_0^F C_F} \frac{1}{1 + \psi_0 \, C_T}, \qquad (2)$$

where χ_0^W and χ_0^F are the positive feedback gains by Wnt and C_F respectively, ψ_0 is the negative gain by C_{T1}. The self-renewal possibility of CPs (p_1) is defined analogously. In addition, we assume that the CSC mitosis rate is also upregulated by C_F.

C_W, C_{WI} and C_F satisfy reaction-diffusion-advection equation that accounts for their production, natural decay and uptake by target cells:

$$\frac{\partial C_i}{\partial t} + \nabla \cdot (\boldsymbol{u_w} C_i) = D_i \Delta C_i + Src_i, \qquad (3)$$

where $\nabla \cdot (\boldsymbol{u_w} C_i)$ models the advection by water pressure, D_i is the diffusivity and Src_i is the source term. Nutrient concentration (n) and negative feedback factors C_{T1}, C_{T2} satisfy quasi-steady state equations $0 = D_i \Delta C_i + Src_i$, see the Methods section for details.

We model tumor angiogenesis following [145], which generates a vascular network independent of the computational grid (lattice-free) and stimulated by soluble angiogenic regulators (e.g. vascular endothelial growth factor, VEGF [154]). We assume that viable tumor cells in the hypoxic core (when the nutrient level is below a threshold) produce VEGF. Vessel sprout sites are selected at a constant probability once the VEGF concentration is higher than a threshold. The tip of vessels moves in circular random walk. At each time step, the tip has a fixed probability to branch into two leading endothelial cells that continue to develop into new vessels. Once a leading cell crosses the path of another vessel, the two vessels may connect and form loops, and begin to deliver cell substrates, e.g. nutrients to the tumor. The contribution from all vessel segments that supply cell substrates is integrated to obtain the effective vascular density. We refer to [145] for further details. Tumor cells increase solid pressure when they

proliferate, and vessels may crush and be removed from simulation under excessive pressure. The model is illustrated in Fig. 1A.

Introduction

Glioblastoma (grade IV glioma) is one of the most aggressive, heterogeneous, vascularized and deadly brain tumors that causes more than ten thousand deaths each year in the United States. The median patient survival for glioblastoma is approximately 15 months, according to the American Brain Tumor Association. It remains a challenge to eradicate glioblastoma due to its high heterogeneity and vascularization.

The cancer stem cell (CSC) hypothesis (i.e. a group of cells are capable of initiating a new tumor mass and differentiate into other tumor cell hierarchies) in glioblastoma has been extensively studied in [126, 134, 154, 171-176]. The glioma stem cell (gSC) hierarchy is found to play a crucial role in tumor development and therapy resistance. Tumors with higher stem cell population are more aggressive and vascularized than those with fewer or no stem cells [171]. gSCs are also able to initiate tumors when implanted in animal models [174].

It has been found in glioma that Nestin+ cells are located closer to the capillaries, and gSCs cultured with endothelial cells (ECs) maintain their proliferation and self-renewal properties [129], even when gSCs do not directly contact with ECs. This suggests an EC-gSC crosstalk in glioma. Possible mechanisms include perivascular nitric oxide [130, 177], Hedgehog pathway [134] and Interleukin-8 signaling [172]. In addition, recent studies in [174, 176, 178] have found that cells facing the lumen of some vessels in glioma were p53 and epithelial growth

factor (EGFR) positive, i.e. they carried tumor-cell mutations. When culturing gSCs in EC conditions, the cells showed EC phenotype and expressed endothelial factors. However, this was not observed on non-stem cell lines. This suggests that glioblastoma cells actively participate in the tumor niche and neovasculature formation. These transdifferentiated cells have been found in the core of the tumors and particularly close to the hypoxic regions [174]. It has been hypothesized that transdifferentiation might be related to hypoxic conditions but many questions regarding these new endothelial cells still remain.

Over the last few decades, various therapies have been studied and tested clinically. A typical initial treatment plan consists of surgical resection of the tumor, followed by chemotherapy (e.g. temozolomide) and/or radiotherapy for 6 weeks, and another chemotherapy session for six to twelve months. In addition, antiangiogenic therapy (e.g. bevacizumab or avastin) has been approved by the FDA for glioblastoma treatments, which neutralizes vascular endothelial growth factor (VEGF) secreted by glioma initiating cells to promote the formation of new tumor blood vessels that supply nutrients and oxygen. There has been observed clinically a decreased number of tumor blood vessels, but no significant improvements in patient survival rate [179]. Additionally, increased tumor invasiveness following antiangiogenic therapy has been reported in [163, 164].

Tumor recurrence is frequently observed following the initial treatment plan. This prompts the development of new, personalized and more effective therapies. For example, anti-invasive therapy targets the matrix metalloproteinases (MMPs), which are enzymes secreted by cells during metastasis and angiogenesis to degrade the ECM and basement membrane.

However, MMPs could also be anti-angiogenic as they can sequester and inactivate chemokines and growth factors that mediate metastasis and angiogenesis. In fact, blocking MMPs does not increase the patient survival rates [180].

In addition, several therapies targeting CSCs have been developed due to their importance in tumor progression. For example, differentiation therapies enhance CSC differentiation in order to reduce the tumor aggressiveness and resistance to therapies. One of the most frequently used differentiation therapy is the drug-induced differentiation by all-trans retinoic acid (ATRA, derivate of vitamin A [181]), which has been shown to successfully differentiate both nSCs and CSCs (for example, in acute promyelocytic leukemia). An alternative is bone morphogenic proteins (BMPs), a group of growth factors from the TGFb superfamily. In particular, BMP-4 enhances the differentiation for both nSCs and tumor initiating cells in glioblastoma, and BMP-4 regulates cancer initiation, proliferation and differentiation [182]. The blockage of several signaling pathways has been shown to affect gSC self-renewal, proliferation and differentiation (e.g. Notch, Wnt and Sonic Hedgehog signaling pathways [183]).

Furthermore, the amplification of different cell receptors tyrosine kinases (such as EGFR and the platelet-derived growth factor receptor (PDGFR)) is related to tumor progression. For instance, EGFR is amplified in approximately half glioblastoma tumors [184] and/or mutated (20% to 40% of the EGFR amplified tumors [185]). Same mutation has been found in the transdifferentiated ECs too [186] [187]. The presence of mutated EGFR and EGFR variant III (EGFRvIII) is correlated with bad prognosis, and its expression is associated with CD133 positive cells. Several clinical trials have been studied to inhibit EGFR (e.g. by cetuximab,

erlotinib), but none of them is shown to improve the outcome of traditional therapies due to the difficulty for the drugs to infiltrate the blood brain barrier of the brain blood vessels. Since FDA has not approved these therapies, we now develop a mathematical study to help understand these new therapies and possible combination therapy outcomes.

A number of numerical methods have been developed to model tumor growth and response to therapies [139, 142, 188-191]. For example, [139] used hybrid cellular automation to investigate the effects of metabolic heterogeneity on tumor progression, and showed that diffusible cytotoxic treatments (e.g. chemotherapy) and antiangiogenic therapy may increase metabolic aggressiveness. [140] Revealed that acute and fractionated irradiation results in enrichment in glioma stem cells, which contributes to accelerated repopulation after irradiation, [192] predicted maximal synergistic antitumor effects when macrophage-based therapy that targets hypoxia is administered with conventional chemotherapy. In [138], a data-based model was used to validate the structural link between metastatic emission and primary tumor size. Here, we extend the multi-species tumor lineage model in [142] to 3D and integrate the angiogenesis model in [143]. Tumor cells and cell substrates are treated as continuum, whereas the vasculature is treated as discrete quantities. We also incorporate the CSC-vasculature crosstalk and CSC differentiation to account for the biological mechanisms in glioblastoma.

We begin by solving a three-dimensional hybrid continuum-discrete model that accounts for multispecies tumor progression, angiogenesis, transdifferentiation and the crosstalk between CSCs and the vasculature. Next, we investigate the tumor response to various therapies targeting

the vasculature, CSCs and gECs, and compare our results to experimental and clinical findings. We then summarize our results and discuss future work.

Results

We solve our model in a three-dimensional computational domain. The tumor begins as a perturbed avascular bulk that consists of uniformly distributed 10% gCSCs, 25% CPs, 60% TDs and 5% dead cells. Three tumors are solved independently since the vessel network is stochastic. We use this configuration as our control case for the therapies.

Fig. 1C shows the evolution of tumor. At early times, gCSC clusters emerge at tumor boundary as an effect of Turing-type pattern formation. These gCSC clusters develop into fingers and stay at finger tips. Vessel sprouts (red dots) form near the tumor boundary around T=30, grow and connect with each other into functional vessels (blue lines) that supply nutrients to the tumor. Consequently, cell proliferation is enhanced and the tumor size grows rapidly (see Fig. 2B, E). At the center of tumor, vessel density and C_F are highest, and a new CSC cluster forms then grows large in size.

Transdifferentiated gECs form a network within the hypoxic core

As CSCs transdifferentiate, gECs are pushed to the tumor by the pressure generated by CSC proliferation at tips, and form a network structure (Fig. 1B). Later, the network becomes connected and gECs begin to surround the tumor surface. This CSC cluster contributes significantly to transdifferentiated gECs. As a result, most gECs are hypoxic (nutrient level less than half of the host level, see Fig. 1D), since few nutrients penetrate the tumor. We note that the

percentage of hypoxic gECs drops around T=30 as a result of nutrient supplies from functional vessels. The percentage goes back after T=40 when vessel crushing comes into effect and reduces nutrient supply inside the tumor. This spatial distribution of gECs has been observed in [174] (Fig. 1E), where implanted human glioblastoma spheres with gSCs exhibited human $CD31^+$ (endothelial) markers in mouse brain. Most $CD31^+$ cells were of human origin, while nearly all the $CD31^+$ cells in tumor capsule were murine.

Anti-angiogenic therapy slows down tumor growth but increases invasiveness

Next, we investigate the effects of therapies on the tumor in Fig. 1C. It has been established in [129] that the vasculature maintains the gCSC pool and actively contributes to tumor growth. We now target this crosstalk in a most effective scenario where the vasculature is removed completely from the tumor, and new vessels are not allowed to form with this anti-angiogenic therapy applied continuously. From T=0 to T=50, the growth is identical to the control case in Fig. 1C. After the therapy starts at T=50, the overall volume grows at a slower speed (Fig. 2B). The gCSC cluster in the center persists after the removal of vessels despite the loss of positive feedback from the vasculature. In fact, the nutrient level is reduced in the center after vessels are removed (Fig. 2E), which inhibits gCSC proliferation. As a result, the tumor still grows, and stem cell fractions are only reduced marginally. Near the tumor boundary, stem cell clusters are not affected by the removal of vessels and develop into growing fingers, considerably increasing tumor invasiveness (Fig. 2A,C). This suggests that anti-angiogenic therapies could make the tumor highly invasive, consistent with both experimental and clinical findings [163, 164]. Fig 2F shows that glioblastoma multiforme treated by VEGF inhibitors exhibits increased invasiveness.

Chemotherapy reduces tumor size but results in multifocal tumors

Traditional chemotherapy has been extensively studied in [193-195]. Here, we model chemotherapy by an agent released by the background vasculature that kills viable tumor cells proportionally to their mitosis rates, since tumor cell species may respond to chemotherapy differently. When chemotherapy is applied alone, the tumor continues to grow rapidly in size (Fig. 3A, top panel), as the vasculature continues to support CSC cluster at center and tumor cell proliferation. When chemotherapy is combined with anti-angiogenic therapy (Fig. 3A, bottom), the tumor volume is reduced, as seen in [195] where anti-angiogenic therapies combined with cytotoxic therapies effectively reduce tumor mass. However, most fingers detach from the tumor at late times and form multifocal tumors. This could indicate malignant invasion since each new tumor carries an active CSC niche.

Anti-CSC therapies control tumor invasion

We have demonstrated that chemotherapy tends to enhance tumor invasion. Since CSC clusters near tumor boundary lead finger development, we now target CSCs to control invasiveness. It has been shown that Wnt signaling pathway is vital to CSC self-renewal, and various Wnt inhibitors (WI) have been studied on their therapeutic effects [183]. Here, we inhibit Wnt signaling by making the background vasculature to release WI in full contact with the tumor. WI from the host disturbs the pattern formation system. As a result, the tumor treated with a moderate level of WI has fewer CSC niches at tumor boundary, and new CSC clusters no longer form (e.g. T=150 in Fig. 2A and Fig. 4A, top panel). CSC fractions are consequently reduced. Higher levels of WI (e.g. Fig. 4A, bottom panel) eradicate all CSC niches at tumor boundary and effectively suppress finger growth. As a result, the tumor evolves in a spherical

shape, and the shape factors are dramatically reduced. However, WI from the background vasculature cannot penetrate the tumor (Fig. 4F, top panel) and has little effect on the CSC cluster at center. In addition, transdifferentiated gECs gradually concentrate at tumor boundary and support the CSC cluster (Fig. 4F, bottom). Consequently, the tumor continues to grow in size, and the CSC fraction is even higher than the untreated tumor.

Alternatively, we target CSCs by forcing them to differentiate. Differentiation therapies have been investigated in both experiments [196, 197] and simulation works [142]. Here, we consider a most effective case that the background vasculature continuously releases CSC differentiation promoter T_1. Similar to WI treatments, a moderate level of T_1 also suppress new CSC niches from forming, and higher levels of T_1 kill all CSC clusters near the boundary (Fig. 5A). However, T_1 from the host is able to diffuse across the tumor (Fig. 5F). This forces all CSC clusters to differentiate (Fig. 5D, insets), even though CSC proliferation levels at center are reduced similarly as Fig 2. Consequently, CSC fractions are significantly reduced. In contrast to Fig. 4, the tumor shrinks since CPs cannot sustain growth (we have assumed that $p_1^{\max} = 0.45 < 0.5$), and TDs are subject to apoptosis. Shape factors are also controlled as the fingers are no longer led by CSC clusters at tips and cease to grow. This behavior has been observed in [142] where tumors treated with large amounts of differentiation promoters are less invasive. In [197], stem-like glioma cells cultured under differentiation conditions invade less aggressively. We note that under T_1 treatments, fingers degenerate into small bumps, while WI treatments eradicate all fingers.

Transdifferentiated gECs/gPericytes enhance tumor resistance to therapies by supporting gCSCs

In Figs. 2-5, transdifferentiated gECs locate near the tumor boundary and support the CSC cluster in the center of tumor. This even caused failure of WI treatments (Fig 4A, bottom panel). Now, we target transdifferentiated gECs by making the background vasculature produce a signaling factor that kills gECs. This removes transdifferentiated gECs supporting the CSC niche at center (Fig. 6A, bottom panel). Consequently, the positive feedback from gECs to CSCs is suppressed. Since anti-angiogenic therapy has already blocked the vasculature-CSC crosstalk, WI treatments are now able to target the CSC niche at center and eventually kill the tumor. This suggests that gECs enhance tumor resistance to WI treatments. To test the effect of gECs on other therapies, we now treat the tumor in Figs. 2-5 additionally by anti-gEC therapies. In all cases, the tumors grow much smaller (more than halved in size, see Fig. 6B). CSC fractions are also reduced by blocking the gEC-CSC positive feedback. Similar results have been observed experimentally. For example, [171] observed that when primary glioblastoma multiforme CSCs were cultured under endothelial conditions, a larger number of CSCs survived radiotherapy by γ-irradiation. We note that without applying anti-CSC treatments, anti-gEC treatments may increase tumor invasion by killing gECs supporting the necks between finger tips and the tumor, thus detaching the fingers (see Sec. S2 in supplemental materials).

Combinatorial therapies that incorporate anti-gEC/gPericyte components are highly synergistic

We have demonstrated that combined therapies involving anti-gEC treatments are more effective than monotherapies. Now, we combine previously studied therapies compare their effectiveness. With antiangiogenic therapy applied, chemotherapy reduces tumor growth by killing all viable tumor cells (Fig. 7A), while it has little effect on removing gECs at tumor

boundary. When chemotherapy is combined with anti-gEC therapy, transdifferentiated gECs around tumor boundary are removed, but fingers become multifocal tumors and tumor invasion is increased, as seen in Fig. 6. However, when anti-CSC treatments are applied, the fingers are either degenerated by differentiation or eradicated by Wnt-Inhibitor. Consequently, tumor invasion is effectively controlled. We suggest that a combination of anti-angiogenic, chemo-, anti-CSC and anti-gEC therapy greatly reduces both tumor growth and invasion.

Discussion

We have developed and tested a hybrid continuum-discrete multispecies model on vascular tumor invasion and tumor responses to cancer therapies. Our model accounts for feedback control on a branched cell lineage through soluble signaling factors produced by tumor cells, host tissue and the vasculature. In addition to the normal lineage progression, cancer stem cells transdifferentiate into gECs that maintain the stem cell niche together with the vasculature. Tumor cells in the hypoxic core positively feedback to the vessel network through VEGF, while tumor cell proliferation negatively regulate the vasculature through pressure. Nutrient delivery from the vasculature provides positive feedback on cancer cell proliferation.

Conventional anti-angiogenic therapy and chemotherapy both inhibit tumor growth, by either inducing hypoxia to reduce cell proliferation or killing viable tumor cells. However, these therapies applied alone or concurrently enhance tumor invasiveness. The removal of vasculature makes the tumor invade aggressively by increasing their surface area to gain access to nutrient supplies from the host. In [164], intense hypoxia was observed following antiangiogenic

treatments, suggesting the invasive phenotype as an adaptive response to hypoxia due to the lack of vessels

We have demonstrated that CSC patterning plays an important role in tumor invasion, as CSCs cluster near the tumor boundary and develop into invasive fingers [142, 198]. Consequently, anti-CSC treatments are expected to reduce tumor invasion. We investigated therapies that inhibit CSC self-renewal (e.g. by blocking Wnt signaling) and disrupt the pattern formation near the tumor boundary. Invasive fingers are subsequently eradicated and the tumor grows slower in size, as seen in [199]. In practice, inhibiting the Sonic Hedgehog pathway has been shown to significantly deplete CSCs from the tumor spheres. As a result, the growth rate of the tumor is decreased [200]. Additionally, mediation of the PDGFRα suppresses the growth of the cells in the periphery of the tumor, decreasing invasive tumor fronts or invasive fingers into the normal brain tissue, possibly by inducing CSC apoptosis [201]. Another pathway closely involved in CSC regulation is the Notch pathway, and inhibiting this pathway has been found to reduce CSC population as well as the tumor volume [131, 202].

In addition, CSCs actively contribute to glioma chemo and radiotherapy resistance. We have demonstrated that differentiation therapies exhibit anti-CSC effects by forcing CSCs to differentiate. Tumor sizes are effectively reduced by terminal cell apoptosis, and finger growth is also suppressed. This effect has been observed in [197], where stem-like glioma cells cultured on differentiation-promoting (ATRA-containing) medium invade less aggressively. Moreover, BMP-4 treatment also showed pro-differentiation effects and reduced infiltrating tumor cells into the host, which suppressed the tumorigenicity of the glioblastoma [182].

It is thought that anti-angiogenic therapies block the CSC-vasculature crosstalk, but fail to affect transdifferentiated gECs since these cells are not VEGF dependent [186]. Consequently, these gECs positively regulate CSC proliferation and self-renewal, and it is hypothesized that the presence of these cells is responsible for glioblastoma resistance to traditional cancer therapies. Here, we have demonstrated that targeting transdifferentiated gECs effectively reduce tumor size, especially when applied concurrently with anti-CSC treatments. As we mentioned above, EGFR is involved in proliferation, differentiation, tumor cell migration and angiogenesis regulation. Therefore, we hypothesize that blocking EGFR could effectively target gECs.

In practice, the first generation of EGFR inhibitors (antibodies and pharmacological drugs, such as erlotonib, cetucimab, nimotuzumab and panitumumab) did not improve clinical outcomes compared to the traditional protocols [184], mainly due to the glioma cells resistance. However, these inhibitors combined with other therapies such as chemotherapy, differentiation [203], antiangiogenic therapies [204] or signaling pathway blockage [205] significantly impair tumor aggressiveness.

Our results suggest that combined therapies targeting the vasculature, CSCs and transdifferentiation are highly synergistic. Anti-angiogenic therapy inhibits tumor cell proliferation and blocks the positive feedback from the vasculature to CSCs. Anti-CSC therapies are vital for controlling tumor invasion. Treating gECs further reduces tumor sizes by targeting CSCs indirectly. Together, these therapies are able to reduce both tumor size and invasion. The latest generation of EGFR inhibitors, such as irreversible tyrosine kinase inhibitors (e.g.

dacomitinib, clinical trial NCT01520870 [185]) effectively reduce the tumor volume by decreasing the glioma initiating cells population through enhancing their differentiation [185], and could be synergized by PI3K/mTor inhibitors. Therefore, we suggest that EGFR inhibitor matches our differentiation, anti-CSC and anti-gEC agent complemented with an antiangiogenic therapy and/or chemotherapy.

However, we predict increased tumor invasion following anti-gEC treatments. gECs are shown to support finger-tumor connections, and killing these gECs develops multifocal tumors. This agrees with experimental observations of dacomitinib, which has to be administered continuously due to the tumor recurrence whenever the treatment stops.

We note that the anti-angiogenic therapy in this paper was implemented as the most effective case, where the vasculature is completely removed and no vessels can form thereafter. However, a small amount of function vessels delivering nutrients to the tumor may help to control the invasion, risking larger tumor in size. In practice, anti-VEGF binding is a candidate of anti-angiogenic therapies [206]. Anti-CSC therapies and chemotherapies can also be administered through functional vessels rather than from the host. Investigation of these therapy strategies is left to future work.

Methods

We solve a simplified model of soft tissue mechanics for tumor cell species. In Eq. (1), M is the cell mobility, $\mu = \frac{\gamma}{\varepsilon}\left(f'(\varphi_T) - \varepsilon^2\nabla^2\varphi_T\right)$ is the chemical potential. $f(\varphi_T) = \frac{1}{4}\varphi_T^2(1-\varphi_T)^2$ is a double-well potential that delineates the phase separation of the tumor ($\varphi_T = 1$) and host tissues

($\varphi_T = 0$). γ measures the stiffness of tumor-host interface, and ε is the interface thickness. $u_s = -\nabla p$ is the solid velocity that models passive cell movement by pressure (simplified Darcy's law). p is the solid pressure generated by tumor cell proliferation ($-\nabla^2 p = Src_T$, where Src_T quantifies the mass exchange of all tumor cells). Assuming no voids, namely the total tumor, host tissue (φ_H) and water region (φ_W) satisfy $\varphi_T + \varphi_H + \varphi_W = 1$, we solve the water pressure q by $-\nabla^2 q = -Src_T$ and the fluid velocity is defined by $\boldsymbol{u}_w = -\nabla q$ [50].

The source terms Src_i in Eq. (1) account for tumor cell proliferation, self-renewal and differentiation. In particular, gCSCs proliferate at base rate λ_m^{SC}. gCSCs may self-renew with possibility p_0, differentiate to CPs, or transdifferentiate to gECs/gPericytes with branching possibility r. CPs may self-renew with possibility p_1 or differentiate to TDs. TDs undergo apoptosis at rate λ_a^{TD}, and dead cells are subject to lysis at rate λ_L^D. The mass exchange terms are

$$Src_{SC} = \lambda_m^{SC} n \varphi_{SC} \cdot (2p_0 - 1),$$

$$Src_{CP} = \lambda_m^{SC} n \varphi_{SC} \cdot 2(1 - p_0 - r) + \lambda_m^{CP} n \varphi_{CP} \cdot (2p_1 - 1), \qquad (4)$$

$$Src_{EC} = \lambda_m^{SC} n \varphi_{SC} \cdot 2r,$$

$$Src_{TD} = \lambda_m^{CP} n \varphi_{CP} \cdot (1 - 2p_1) - \lambda_a^{TD} \varphi_{TD},$$

$$Src_D = \lambda_a^{TD} \varphi_{TD} - \lambda_L^D \varphi_D.$$

We note that Eq. (1) is only solved for φ_T, φ_{SC}, φ_{CP}, φ_{EC} and φ_D. The volume fraction of TDs is calculated by $\varphi_{TD} = \varphi_T - \varphi_{SC} - \varphi_{CP} - \varphi_{EC} - \varphi_D$.

Source terms Src_i in Eq. (3) account for cell substrates production, uptake and natural decay. In particular, we assume a generalized Gierer-Meinhardt model [142] for C_W and C_{WI}:

$$Src_W = \bar{\gamma}\left(p_W \frac{c_W^2}{c_{WI}} n\varphi_{SC} - d_W C_W + u_0 n(\varphi_T - \varphi_D)\right), \quad (5)$$

$$Src_{WI} = \bar{\gamma}(p_{WI} C_W^2 n\varphi_{SC} - d_{WI} C_{WI}),$$

where p_W and d_W are the production and natural decay rate of C_W, respectively. The parameters for C_{WI} are defined analogously. We assume that $D_W << D_{WI}$. $\bar{\gamma}$ is the reaction rate, u_0 models a low-level leak of C_W from viable tumor cells. The production of C_W and C_{WI} is dependent on the nutrient level n. C_W nonlinearly upregulates C_{WI}, which in turn inhibits C_W production.

The signaling factor C_F satisfies a reaction-diffusion-advection equation that accounts for its production from the vasculature and transdifferentiated gECs:

$$\frac{\partial C_F}{\partial t} + \nabla\cdot(u_w C_F) = \nabla\cdot(D_F \nabla C_F) + \left(p_F^V \rho_V + p_F^{EC}\varphi_{EC}\right)\cdot\left(\bar{F} - F\right) - d_F C_F,$$

where D_F and d_F are the diffusivity and the natural decay rate, p_F^V and p_F^{EC} are the production rates by the vasculature and gECs respectively. ρ_V is the vessel density function, $\bar{F}$ is concentration of C_F in the vasculature.

The nutrient concentration (n) satisfies quasi steady state equation

$$0 = D_n \Delta n - (u_n^{SC}\varphi_{SC} + u_n^{CP}\varphi_{CP} + u_n^{TD}\varphi_{TD})n + p_n\ Q(\varphi_T)(\bar{n} - n),$$

where D_n is the nutrient diffusivity, u_n^{SC}, u_n^{CP} and u_n^{TD} are the uptakes rates by gCSCs, CPs and TDs respectively. $Q(\varphi_T) \approx 1 - \varphi_T$ approximates the characteristic function of host tissue, p_n is the nutrient production rate by background vasculature. $\bar{n} = 1.0$ is the nutrient concentration in

the microenvironment. C_{T1} and C_{T2} satisfy similar equations except that they are produced by TDs and uptaken by gCSCs and CPs respectively.

We solve the equations above by an adaptive nonlinear multigrid method described in [145]. We use an implicit second order Crank-Nicholson scheme for time discretization. Spatial derivatives are discretized using central difference approximations. Equations at the implicit time step are reformulated as a system of second order equations. Block structured Cartesian refinement is used to efficiently resolve the multiple spatial scales, especially in regions with large gradients (typically around tumor boundary). Tumor cell species and soluble cell substrates are solved with homogenous Neumann boundary condition. Pressure, chemical potential and nutrients satisfy homogenous Dirichlet condition.

Tumor statistics, spatial distributions of cell species and vessel networks are generated by MATLAB. The non-dimensional tumor shape factor is computed by $\sqrt[3]{36\pi}\frac{S}{V^{2/3}}$ where V is the tumor volume and S is the surface area.

Figures

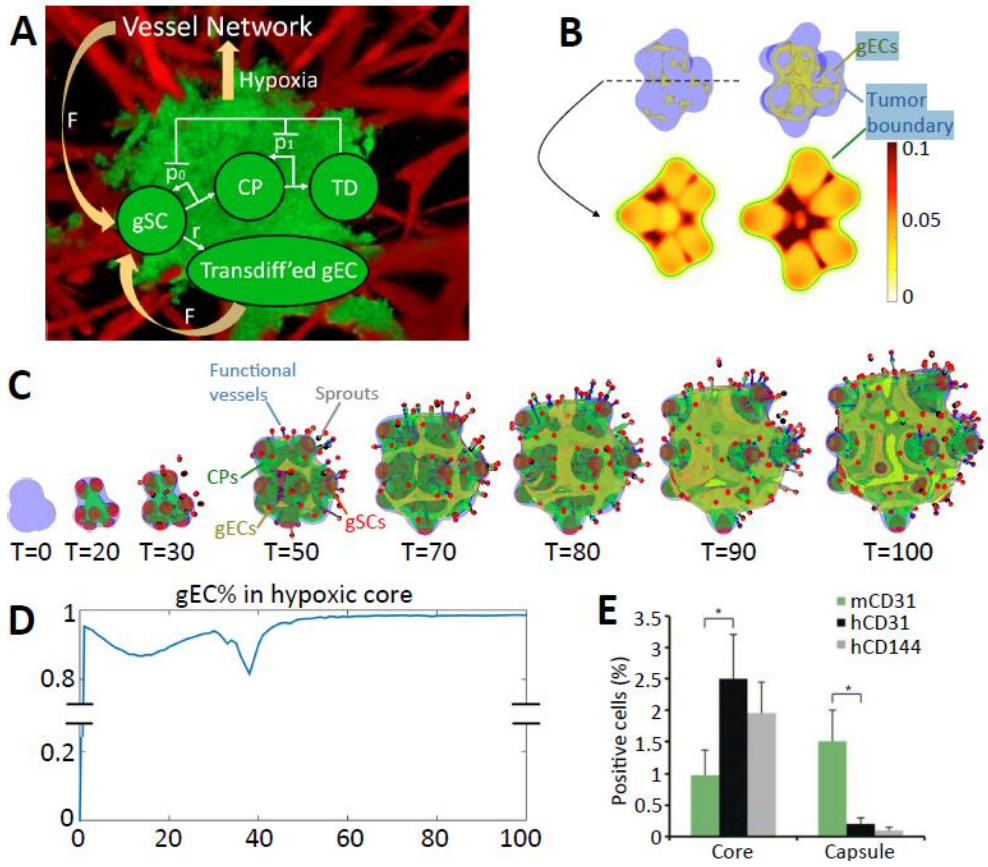


Fig. 4.1. Model schematic and spatial distribution of transdifferentiated gECs in control case. **(A)** Model schematic. Background shows the slice of a vascularized colon tumor spheroid made in 15% methylcellulose with sw620 and fibroblasts cells, and embedded in natural colon extracellular matrix together with endothelial progenitor cells (EPCs, red). Colon metastatic cell line (sw620) is transduced in green. **(B)** Transdifferentiated gECs spontaneously form a network structure. 3D isosurfaces of tumor boundary (blue) and $\varphi_{EC} = 0.1$(yellow) are shown in top panels. Bottom panels show the 2D slices of φ_{EC}. **(C)** Evolution of a vascularized tumor. The spatial distribution of tumor cells (blue: tumor boundary, red: $\varphi_{SC} = 0.3$, green: $\varphi_{CP} = 0.25$) and vasculature (red dots: sprout roots; grey: sprouts; blue: functional vessels; green dots: anastomosis points) are shown at indicated times. **(D)** Most transdifferentiated gECs locate within the hypoxic core. **(E)** FACS evaluation of murine $CD31^{+}/CD45^{-}$ (mCD31), human CD31 (hCD31) and human CD144 (hCD144) in the capsule and core of the tumor reveals that about

70% CD31$^+$ cells in the tumor core were of human origin (transdifferentiated), whereas nearly all the CD31$^+$ cells in the tumor capsule were murine [174].

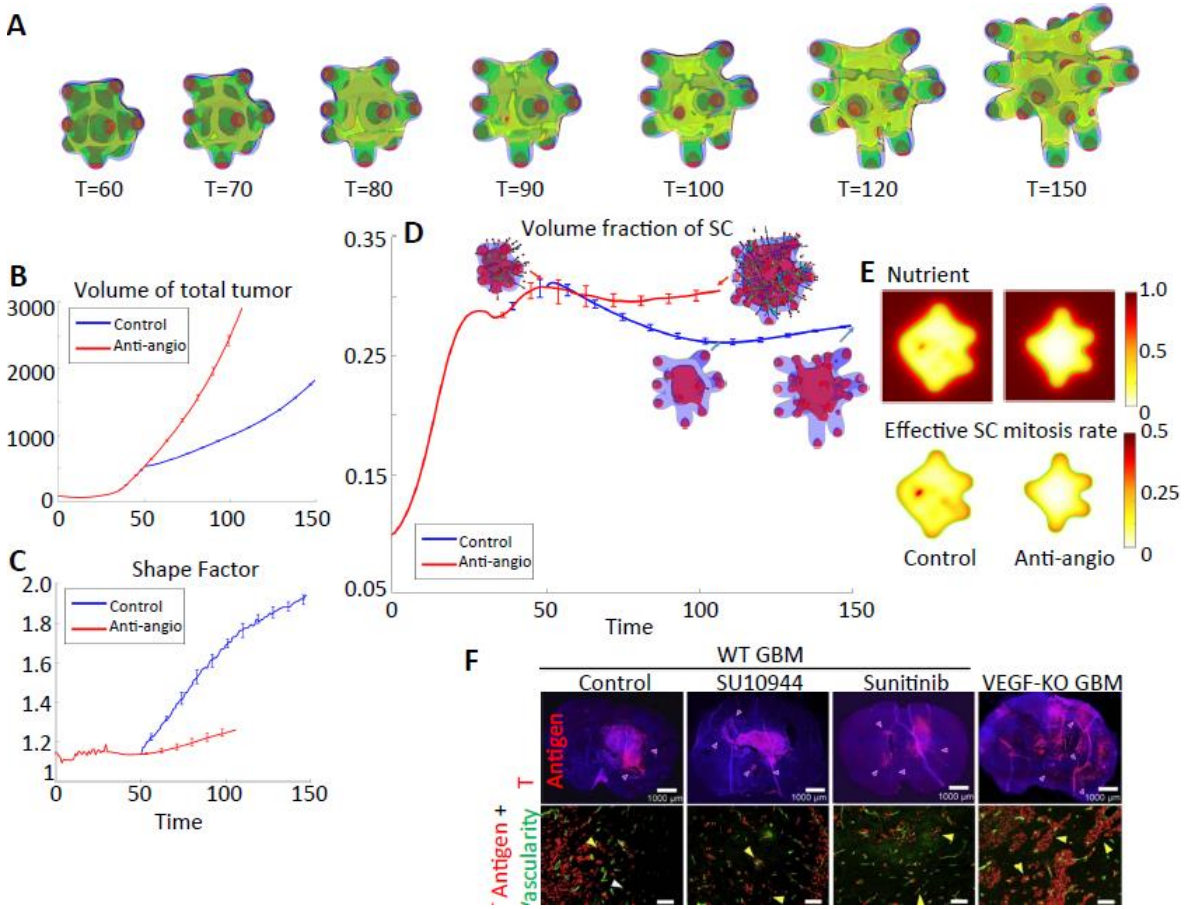


Fig. 4.2. Anti-angiogenic therapy reduces tumor size but increases invasion. **(A)** Evolution of a tumor treated with anti-angiogenic therapy. The growth is identical to Fig. 1C until T=50. At T=50, the vasculature is removed from the tumor. **(B-D)** Evolution of tumor volumes, shape factors and CSC fractions for the tumor in Fig. 1C (Control) and (A) (Anti-angio). Insets in (D) show CSC distributions (red) within the tumor (blue). **(E)** 2D slices of nutrient and effective CSC mitosis rate $n\lambda_m^{SC}$ are shown at T=70. **(F)** Top row: Glioblastoma multiforme (GBM) with fluorescent SV40 T antigen staining (red) on whole brain sections counterstained with DAPI (blue). Control wild-type (WT) GBMs appear less invasive than WT GBMs treated with SU10944 or sunitinib, or *VEGF*-KO GBMs (purple arrowheads). Bottom row: tumor cells (anti-T antigen antibody; red) and the perfused vasculature (FITC-lectin, green). WT GBM cells infiltrate as single cells into the brain parenchyma without associating with blood vessels (white arrowheads) or invade alongside blood vessels in the brain (perivascular invasion; yellow

arrowheads). GBMs treated with either SU10944 or sunitinib as well as *VEGF*-KO GBMs are more invasive and predominantly migrate along blood vessels (yellow arrowheads). [33]

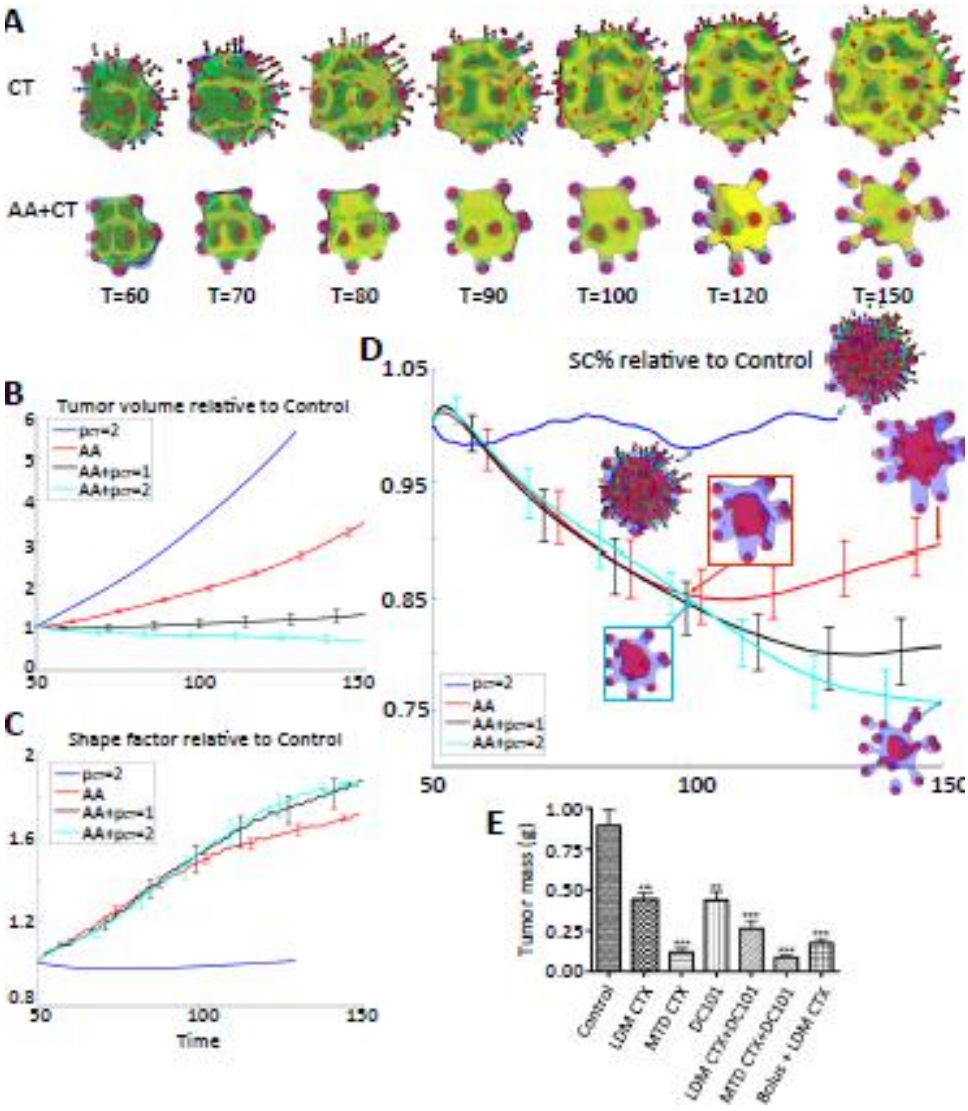


Fig. 4.3. Chemotherapy reduces tumor size but results in multifocal tumors. **(A)** Evolution of a tumor treated with anti-angiogenic and chemotherapy. The growth is identical to Fig. 1C until T=50. At T=50, the vasculature is removed from the tumor, and the background vasculature begins to release a chemotherapy agent that kills all viable tumor cells proportionally to their mitosis rates. **(B-D)** Evolution of tumor volumes, shape factors and CSC fractions are plotted relatively to Control at T=50. The tumor in (A) is shown in black. AA: anti-angiogenic therapy; p_{CT} : production rate of the chemotherapy agent. Insets in (D) show CSC distributions (red)

within the tumor (blue). **(E)** A combination of anti-angiogenic therapy (DC101) and chemotherapy (MTD, LDM) results in smaller tumor mass than monotherapies [195].

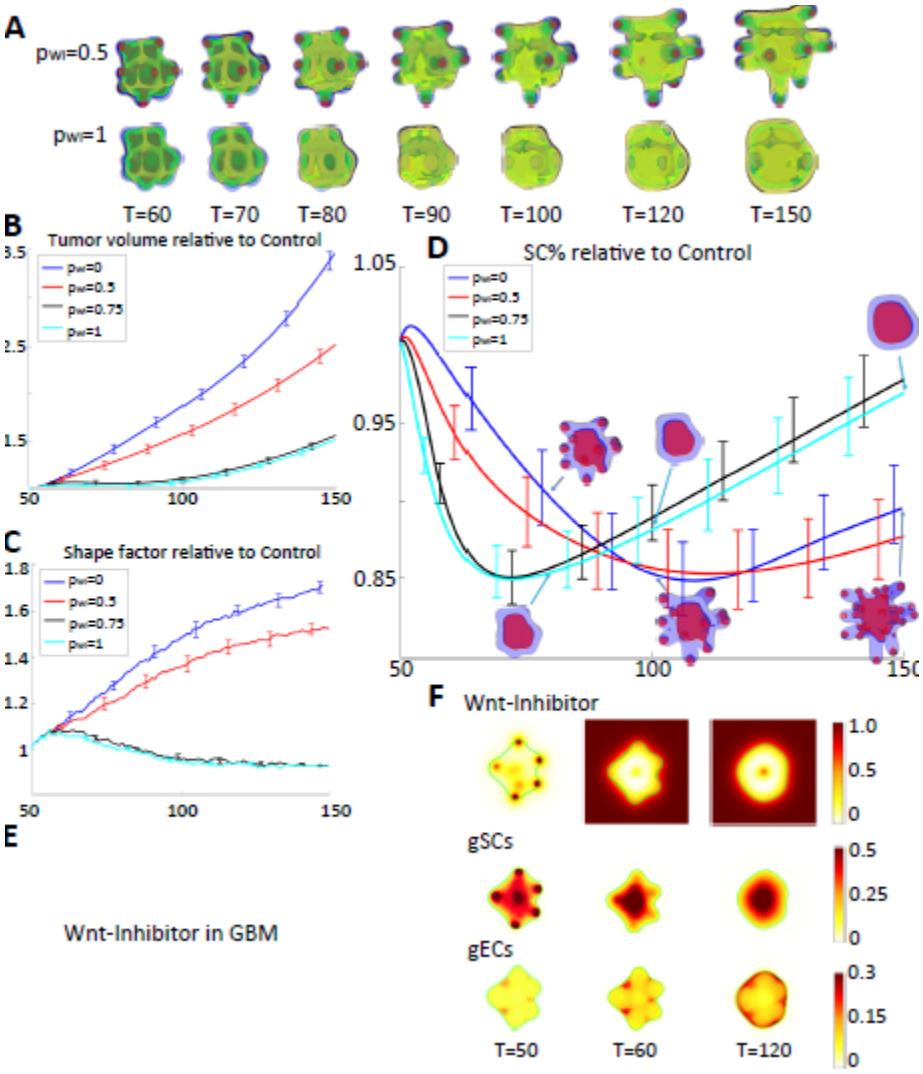


Fig. 4.4. Wnt-inhibitor therapy reduces tumor invasion but suffers from resistance induced by transdifferentiation. (A) Evolution of tumors treated with anti-angiogenic and different levels of Wnt-inhibitor (WI). The growth is identical to Fig. 1C until T=50. At T=50, the vasculature is removed from the tumor, and the background vasculature begins to release WI at indicated rates. **(B-D)** Evolution of tumor volumes, shape factors and CSC fractions are plotted relatively to Control at T=50. Insets in (D) show CSC distributions (red) within the tumor (blue). **(F)** 2D slices of WI, CSCs and gECs in the tumor with $p_{WI} = 1$ are shown at indicated times.

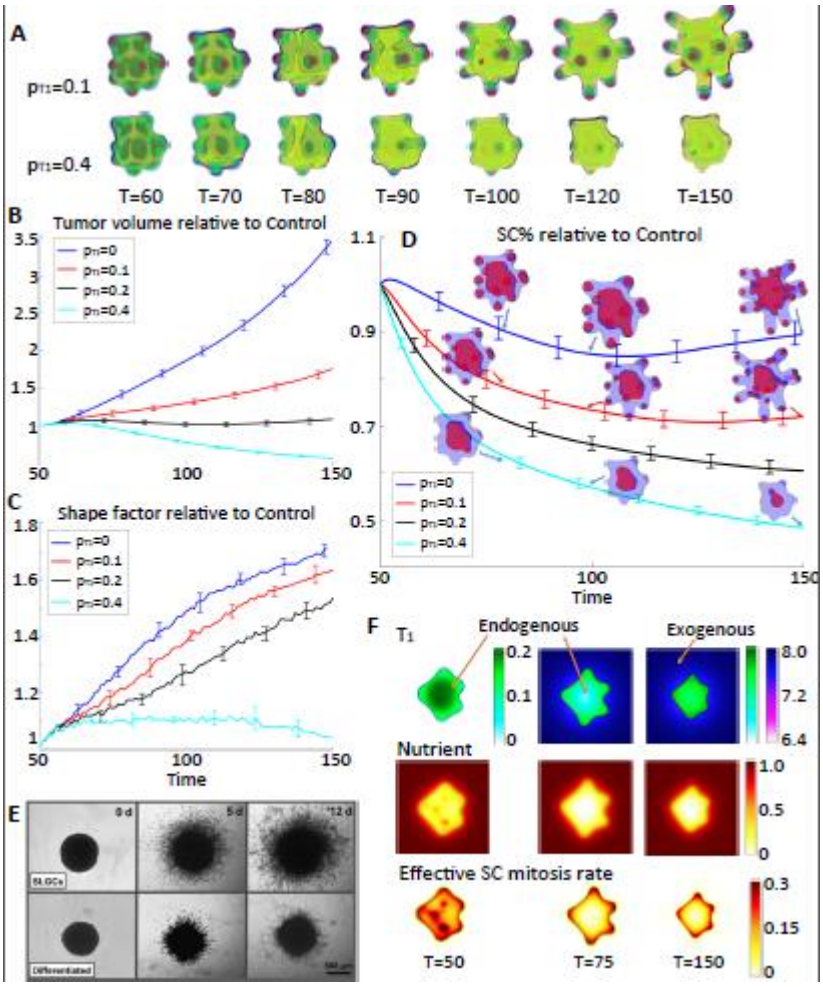


Fig. 4.5. Differentiation therapy reduces both tumor growth and invasion. (A) Evolution of tumors treated with anti-angiogenic and different levels of differentiation promotor T_1. The growth is identical to Fig. 1C until T=50. At T=50, the vasculature is removed from the tumor, and the background vasculature begins to release T_1 at indicated rates. **(B-D)** Tumor volumes, shape factors and CSC fractions are decreased as T_1 treatments become stronger. **(F)** 2D slices of T_1, nutrients and effective CSC mitosis rates in the tumor with $p_{T1} = 0.4$ are shown at indicated times. **(E)** Differentiation reduces the invasiveness of stem-like glioma cells (SLGCs) [197].

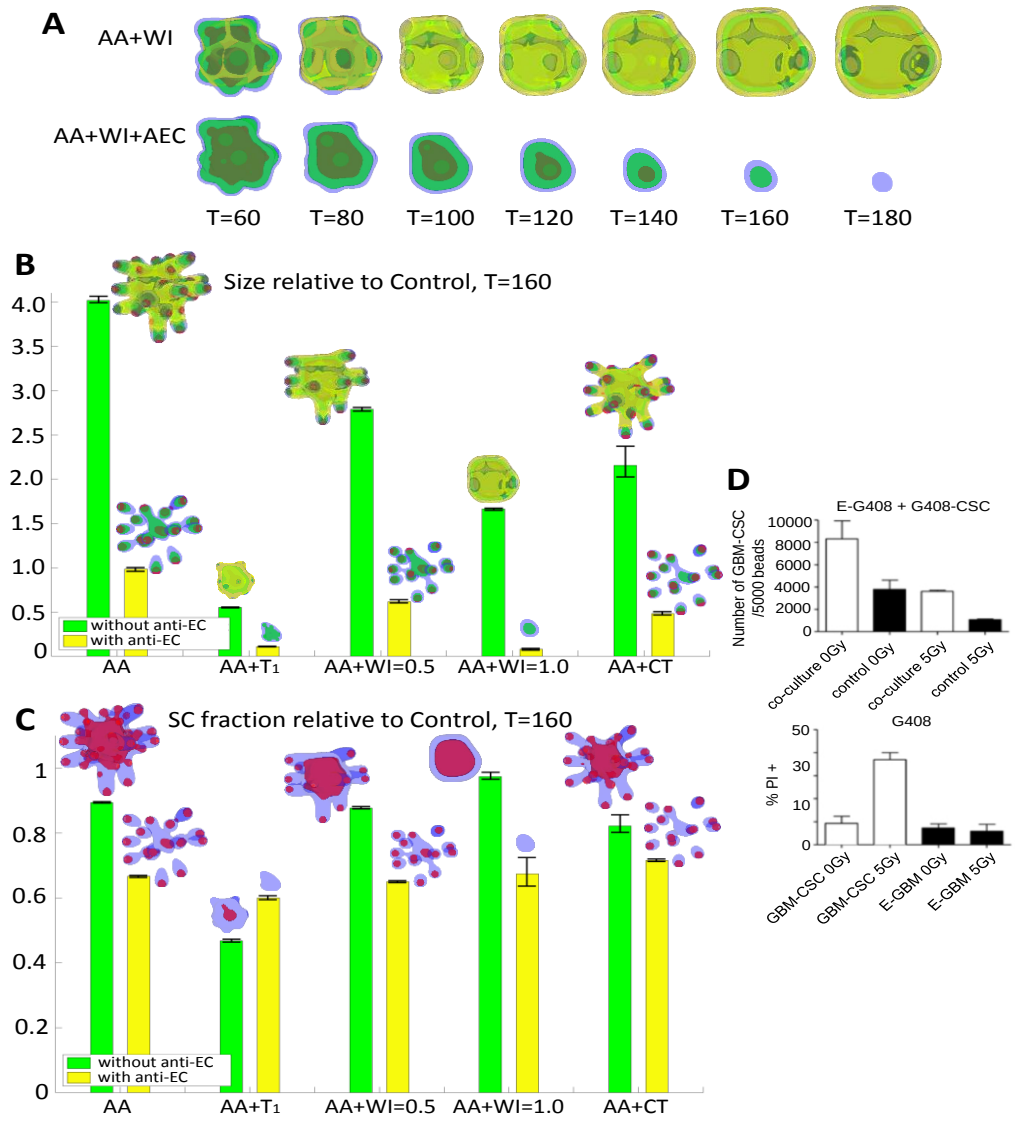


Fig. 4.6. Transdifferentiated gECs/gPericytes enhance tumor resistance to therapies by supporting gCSCs. **(A)** Top panel: evolution of a tumor treated with anti-angiogenic therapy and WI ($p_{WI} = 1$). Bottom: the tumor is treated additionally by anti-gEC treatments. **(B-C)** Tumor volumes and CSC fractions are plotted relatively to Control at T=50. The tumors treated with anti-angiogenic therapy (AA) in Fig. 2A, WI treatments with $p_{WI} = 0.5$ and $p_{WI} = 1$ in Fig. 4A, differentiation therapies with $p_{T1} = 0.4$ in Fig. 5A and chemotherapies with $p_{CT} = 0.5$ in Fig. 3A are shown in blue bars. Yellow bars show the corresponding tumor treated additionally with anti-gEC therapy from T=50. Insets above the bars show the corresponding cell distributions (blue: tumor; red: CSCs; green: CPs; yellow: gECs). **(D)** Primary glioblastoma

multiforme (GBM) cultures were either cultured in endothelial differentiation conditions (E-GBM) or maintained under CSC conditions (GBM-CSC), and subsequently exposed to γ-irradiation. Co-cultures show larger numbers of CSCs (top panel) and less cell death (bottom) [171].

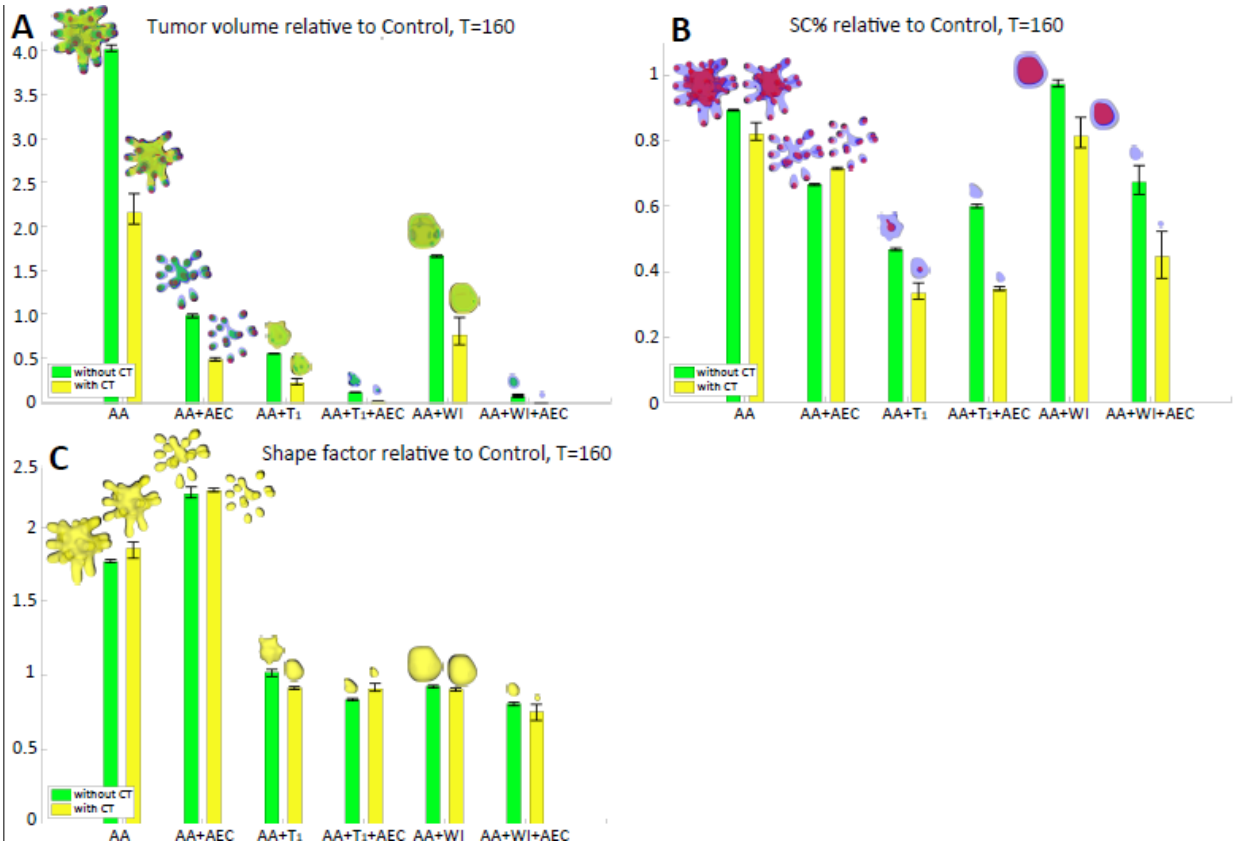


Fig. 4.7. Combined therapies effectively control both tumor growth and invasion. Tumor volumes **(A)**, CSC fractions **(B)** and shape factors **(C)** are plotted relatively to Control at T=50. The tumors treated with anti-angiogenic therapy (AA) in Fig. 2A, WI treatments with $p_{WI} = 1$ in Fig. 4A and differentiation therapies with $p_{T1} = 0.4$ in Fig. 5A with or without anti-gEC therapies are plotted in blue bars. Yellow bars show the corresponding tumor treated additionally with chemotherapy from T=50. Insets above the bars in (A-B) show the corresponding cell

distributions (blue: tumor; red: CSCs; green: CPs; yellow: gECs), and tumor morphologies in (C).

REFERENCES

126. Bayin, N.S., A.S. Modrek, and D.G. Placantonakis, *Glioblastoma stem cells: Molecular characteristics and therapeutic implications.* World J Stem Cells, 2014. **6**(2): p. 230-8.
129. Calabrese, C., et al., *A perivascular niche for brain tumor stem cells.* Cancer Cell, 2007. **11**(1): p. 69-82.
130. Charles, N., et al., *Perivascular nitric oxide activates notch signaling and promotes stem-like character in PDGF-induced glioma cells.* Cell Stem Cell, 2010. **6**(2): p. 141-52.
131. Fan, X., et al., *NOTCH pathway blockade depletes CD133-positive glioblastoma cells and inhibits growth of tumor neurospheres and xenografts.* Stem Cells, 2010. **28**(1): p. 5-16.
134. Yan, G.N., et al., *Endothelial cells promote stem-like phenotype of glioma cells through activating the Hedgehog pathway.* J Pathol, 2014. **234**(1): p. 11-22.
138. Hartung, N., et al., *Mathematical modeling of tumor growth and metastatic spreading: validation in tumor-bearing mice.* Cancer Res, 2014. **74**(22): p. 6397-407.
139. Robertson-Tessi, M., et al., *Impact of metabolic heterogeneity on tumor growth, invasion, and treatment outcomes.* Cancer Res, 2015. **75**(8): p. 1567-79.
140. Gao, X., et al., *Acute and fractionated irradiation differentially modulate glioma stem cell division kinetics.* Cancer Res, 2013. **73**(5): p. 1481-90.
142. Youssefpour, H., et al., *Multispecies model of cell lineages and feedback control in solid tumors.* Journal of theoretical biology, 2012. **304**: p. 39-59.
143. Frieboes, H.B., et al., *Three-dimensional multispecies nonlinear tumor growth-II: Tumor invasion and angiogenesis.* J Theor Biol, 2010. **264**(4): p. 1254-78.
145. Wise, S.M., J.S. Lowengrub, and V. Cristini, *An Adaptive Multigrid Algorithm for Simulating Solid Tumor Growth Using Mixture Models.* Math Comput Model, 2011. **53**(1-2): p. 1-20.
147. Gregory, C.A., et al., *The Wnt signaling inhibitor dickkopf-1 is required for reentry into the cell cycle of human adult stem cells from bone marrow.* Journal of Biological Chemistry, 2003. **278**(30): p. 28067-28078.
148. Lee, N., et al., *A potential role for Dkk-1 in the pathogenesis of osteosarcoma predicts novel diagnostic and treatment strategies.* British Journal of Cancer, 2007. **97**(11): p. 1552-1559.
154. Bao, S., et al., *Stem cell-like glioma cells promote tumor angiogenesis through vascular endothelial growth factor.* Cancer Res, 2006. **66**(16): p. 7843-8.
163. Casanovas, O., et al., *Drug resistance by evasion of antiangiogenic targeting of VEGF signaling in late-stage pancreatic islet tumors.* Cancer Cell, 2005. **8**(4): p. 299-309.
164. Paez-Ribes, M., et al., *Antiangiogenic therapy elicits malignant progression of tumors to increased local invasion and distant metastasis.* Cancer Cell, 2009. **15**(3): p. 220-31.
169. Johnston, M.D., et al., *Mathematical modeling of cell population dynamics in the colonic crypt and in colorectal cancer.* Proc Natl Acad Sci U S A, 2007. **104**(10): p. 4008-13.
170. Meulmeester, E. and P. Ten Dijke, *The dynamic roles of TGF-beta in cancer.* J Pathol, 2011. **223**(2): p. 205-18.

171. Borovski, T., et al., *Therapy-resistant tumor microvascular endothelial cells contribute to treatment failure in glioblastoma multiforme.* Oncogene, 2013. **32**(12): p. 1539-48.
172. Infanger, D.W., et al., *Glioblastoma stem cells are regulated by interleukin-8 signaling in a tumoral perivascular niche.* Cancer Res, 2013. **73**(23): p. 7079-89.
173. Mao, F., et al., *A role for LRIG1 in the regulation of malignant glioma aggressiveness.* Int J Oncol, 2013. **42**(3): p. 1081-7.
174. Ricci-Vitiani, L., et al., *Tumour vascularization via endothelial differentiation of glioblastoma stem-like cells.* Nature, 2010. **468**(7325): p. 824-8.
175. Wang, R., et al., *Glioblastoma stem-like cells give rise to tumour endothelium.* Nature, 2010. **468**(7325): p. 829-33.
176. Soda, Y., et al., *Transdifferentiation of glioblastoma cells into vascular endothelial cells.* Proc Natl Acad Sci U S A, 2011. **108**(11): p. 4274-80.
177. Eyler, C.E., et al., *Glioma stem cell proliferation and tumor growth are promoted by nitric oxide synthase-2.* Cell, 2011. **146**(1): p. 53-66.
178. Scully, S., et al., *Transdifferentiation of glioblastoma stem-like cells into mural cells drives vasculogenic mimicry in glioblastomas.* J Neurosci, 2012. **32**(37): p. 12950-60.
179. Field, K.M., et al., *Bevacizumab and glioblastoma: scientific review, newly reported updates, and ongoing controversies.* Cancer, 2015. **121**(7): p. 997-1007.
180. *<Validating matrix metalloproteinases as drug targets and anti-targets for cancer therapy.pdf>*.
181. Cruceru, M.L., et al., *Therapy targets in glioblastoma and cancer stem cells: lessons from haematopoietic neoplasms.* J Cell Mol Med, 2013. **17**(10): p. 1218-35.
182. Piccirillo, S.G., et al., *Bone morphogenetic proteins inhibit the tumorigenic potential of human brain tumour-initiating cells.* Nature, 2006. **444**(7120): p. 761-5.
183. Takebe, N., et al., *Targeting cancer stem cells by inhibiting Wnt, Notch, and Hedgehog pathways.* Nat Rev Clin Oncol, 2011. **8**(2): p. 97-106.
184. Roth, P. and M. Weller, *Challenges to targeting epidermal growth factor receptor in glioblastoma: escape mechanisms and combinatorial treatment strategies.* Neuro Oncol, 2014. **16 Suppl 8**: p. viii14-9.
185. Zahonero, C., et al., *Preclinical Test of Dacomitinib, an Irreversible EGFR Inhibitor, Confirms Its Effectiveness for Glioblastoma.* Mol Cancer Ther, 2015. **14**(7): p. 1548-58.
186. Yasushi Sodaa, T.M., b, Dinorah Friedmann-Morvinskia, Mie Sodaa, Fei Liua, Hiroyuki Michiuec, and M.Y. Sandra Pastorinod, Robert M. Hoffmane,f, Santosh Kesarid, and Inder M. Vermaa,1, *<Transdifferentiation of glioblastoma cells into vascular endothelial cells.pdf>*. PNAS, 2010. **108**(11).
187. Emlet, D.R., et al., *Targeting a glioblastoma cancer stem-cell population defined by EGF receptor variant III.* Cancer Res, 2014. **74**(4): p. 1238-49.
188. Bearer, E.L., et al., *Multiparameter computational modeling of tumor invasion.* Cancer Res, 2009. **69**(10): p. 4493-501.
189. Sanga, S., et al., *Mathematical modeling of cancer progression and response to chemotherapy.* Expert Rev Anticancer Ther, 2006. **6**(10): p. 1361-76.
190. Wise, S.M., et al., *Three-dimensional multispecies nonlinear tumor growth--I Model and numerical method.* J Theor Biol, 2008. **253**(3): p. 524-43.
191. Preziosi, L. and A.R. Tosin, *Multiphase modelling of tumour growth and extracellular matrix interaction: mathematical tools and applications.* Journal of Mathematical Biology, 2009. **58**(4-5): p. 625-656.

192. Owen, M.R., et al., *Mathematical modeling predicts synergistic antitumor effects of combining a macrophage-based, hypoxia-targeted gene therapy with chemotherapy.* Cancer Res, 2011. **71**(8): p. 2826-37.
193. Steiniger, S.C.J., et al., *Chemotherapy of glioblastoma in rats using doxorubicin-loaded nanoparticles.* International Journal of Cancer, 2004. **109**(5): p. 759-767.
194. Taal, W., J.E. Bromberg, and M.J. van den Bent, *Chemotherapy in glioma.* CNS Oncol, 2015. **4**(3): p. 179-92.
195. Folkins, C., et al., *Anticancer therapies combining antiangiogenic and tumor cell cytotoxic effects reduce the tumor stem-like cell fraction in glioma xenograft tumors.* Cancer Res, 2007. **67**(8): p. 3560-4.
196. Kolev, V.N., et al., *PI3K/mTOR dual inhibitor VS-5584 preferentially targets cancer stem cells.* Cancer Res, 2015. **75**(2): p. 446-55.
197. Campos, B., et al., *Differentiation therapy exerts antitumor effects on stem-like glioma cells.* Clin Cancer Res, 2010. **16**(10): p. 2715-28.
198. Sottoriva, A., et al., *Cancer stem cell tumor model reveals invasive morphology and increased phenotypical heterogeneity.* Cancer Res, 2010. **70**(1): p. 46-56.
199. Gurney, A., et al., *Wnt pathway inhibition via the targeting of Frizzled receptors results in decreased growth and tumorigenicity of human tumors.* Proc Natl Acad Sci U S A, 2012. **109**(29): p. 11717-22.
200. Bar, E.E., et al., *Cyclopamine-mediated hedgehog pathway inhibition depletes stem-like cancer cells in glioblastoma.* Stem Cells, 2007. **25**(10): p. 2524-33.
201. *<PDGF receptor alpha inhibition induces apoptosis in glioblastoma cancer stem cells refractory to anti-Notch and anti-EGFR treatment.pdf>*.
202. Hovinga, K.E., et al., *Inhibition of notch signaling in glioblastoma targets cancer stem cells via an endothelial cell intermediate.* Stem Cells, 2010. **28**(6): p. 1019-29.
203. Stockhausen, M.T., et al., *Differentiation of glioblastoma multiforme stem-like cells leads to downregulation of EGFR and EGFRvIII and decreased tumorigenic and stem-like cell potential.* Cancer Biol Ther, 2014. **15**(2): p. 216-24.
204. Tabernero, J., *The role of VEGF and EGFR inhibition: implications for combining anti-VEGF and anti-EGFR agents.* Mol Cancer Res, 2007. **5**(3): p. 203-20.
205. Paul, I., et al., *Current Understanding on EGFR and Wnt/beta-Catenin Signaling in Glioma and Their Possible Crosstalk.* Genes Cancer, 2013. **4**(11-12): p. 427-46.
206. Keunen, O., et al., *Anti-VEGF treatment reduces blood supply and increases tumor cell invasion in glioblastoma.* Proc Natl Acad Sci U S A, 2011. **108**(9): p. 3749-54.

CHAPTER 5. Summary and Conclusions

The goal of this work was to gain a better understanding of the tumor microenvironment. For this purpose, we used experimental and mathematical tools to study the role of the ECM in tumor progression and the importance of tumor heterogeneity in the development of vasculature and anti-cancer therapies.

The findings presented in Chapter 2 revealed that the ECM is a key element in the tumor milleu. We showed that there exist significant differences in protein composition and mechanical properties between the ECM extracted from healthy tissue and the ECM derived from tissue invaded with cancer. Being the tumor ECM a more complex environment; there are some proteins present in tECM that are not present in nECM and that are involved with defective vasculature and bad tumor prognosis [106, 107]. Moreover, these differences in the composition could be the cause of the difference in stiffness. It is already known that the modifications in the ECM due to cancer cause an increase in collagen crosslinking and with this an increase in ECM stiffness[207].

Additionally, we showed that the endothelial cells embedded in the tECM generate a pathological vasculature when compared to the vessels formed in the nECM. This effect could be, the response of the endothelial cells to growth factors present in the tECM. It is known that the proteins present in the ECM of malignant tumors can increase growth factor signaling [105]. We also uncovered the role of the ECM in tumor growth finding that tumor cells grow faster in the tECM than in nECM.

Recent studies have observed a link between ECM mechanical properties and tumor cell behavior, such as ECM stiffness and tumor migration. Moreover, there is a growing research direction leaded by Weaver and her group, in which a relationship between the ECM and metabolism is being investigated [17]. However, it is still not well understood.

Our results about tumor metabolism presented support Weaver hypothesis. These observations demonstrated that the tECM might favor a more glycolytic environment than the normal ECM. Being the ECM stiffness differences a possible reason to the changes in cell metabolism [17]. The implications of the results presented in Chapter 1 are promising: we have design a 3D scaffold that supports vasculature and can reproduce tumor growth which can be used for in vitro studies in cancer drug screening. For example, Dr. Hughes laboratory has developed a microfluidic device in which tumor and endothelial cells can be seeded and vessels can be perfused. This tumor ECM could be added to this platform to study the complete dynamics of the ECM-tumor-perfusion system.

Complementary to this work, we have presented a mathematical model for tumor angiogenesis in chapter 2. The motivation of this project was to elucidate mechanisms that can have a critical role in cancer but that are difficult to model experimentally. That is the case of the tumor heterogeneity. It is well known that CSCs are present in different tumors; however, it is not very easy to follow accurately the effects of the different tumor populations in tumor growth and angiogenesis. The findings presented in this chapter support experimental observations seen in glioblastoma. Moreover, the model predicts a saturation point of the GSCs given a certain initial population[154].

Finally, the findings presented, in chapter 3, revealed the importance of the vasculature developed by the gECs in cancer therapy [174]. These new vessels are able to exert resistance to all the therapies tested. The results of the simulations can help to elucidate a better way to treat glioblastoma. Also, we are looking forward to include in the mathematical model de effects of the ECM in the vasculature and tumor growth. And at some point, we would like to include the geometry and configuration of the microfluidic device into this model. And at some point, we could be able to input some patient data, such as tumor size after certain therapy and then explore a possible individualized treatment

REFERENCES

17. Tung, J.C., et al., *Tumor mechanics and metabolic dysfunction.* Free Radic Biol Med, 2015. **79**: p. 269-80.
105. Egeblad, M., M.G. Rasch, and V.M. Weaver, *Dynamic interplay between the collagen scaffold and tumor evolution.* Current opinion in cell biology, 2010. **22**(5): p. 697-706.
106. Van Obberghen-Schilling, E., et al., *Fibronectin and tenascin-C: accomplices in vascular morphogenesis during development and tumor growth.* Int J Dev Biol, 2011. **55**(4-5): p. 511-25.
107. Orend, G. and R. Chiquet-Ehrismann, *Tenascin-C induced signaling in cancer.* Cancer Lett, 2006. **244**(2): p. 143-63.
154. Bao, S., et al., *Stem cell-like glioma cells promote tumor angiogenesis through vascular endothelial growth factor.* Cancer Res, 2006. **66**(16): p. 7843-8.
174. Ricci-Vitiani, L., et al., *Tumour vascularization via endothelial differentiation of glioblastoma stem-like cells.* Nature, 2010. **468**(7325): p. 824-8.
207. Chen, T.T., et al., *Anchorage of VEGF to the extracellular matrix conveys differential signaling responses to endothelial cells.* The Journal of Cell Biology, 2010. **188**(4): p. 595-609.